Udvikling af materialer til brintpermeable membraner

Bentzer, Henrik Karnøe

Publication date:
2011

Document Version
Publisher's PDF, also known as Version of record

Risø DTU
National Laboratory for Sustainable Energy

Technical University of Denmark

Ph.D. Thesis

Development of materials for hydrogen permeable membranes

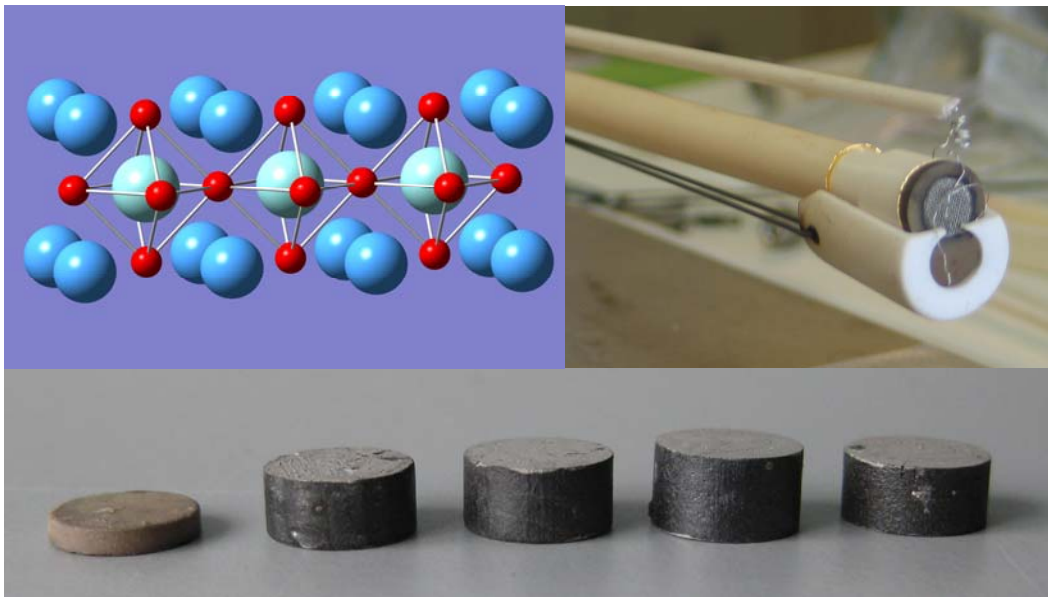

Henrik K. Bentzer

December 2010

PhD Thesis

Henrik K. Bentzer

Academic advisors:

Nikolaos Bonanos
Risø National Laboratory for Sustainable Energy, Technical University of Denmark, Roskilde, Denmark

John W. Phair
poLight AS, Horten, Norway

Submitted December 2010

Abstract

Due to global warming as well as other factors, it is necessary to find alternatives to the current consumption of fossil fuels. Oxide materials with high protonic conductivity can potentially find application within many different technological fields in a society that is based on renewable energy to a wider extent. Materials that also have electronic conductivity can find use in hydrogen permeable membranes, which is the main subject of this thesis.

The focus of the thesis is experimental aspects of development of new membrane materials. The necessary theoretical background is treated, and three primary methods of characterising potential materials are presented, paying specific attention to how they can be applied to materials with mixed protonic and electronic conductivity; conductivity measurements, concentration cell measurements and flux measurements.

Experimental results achieved with all three methods will also be presented.

DC conductivity measurements on yttrium doped strontium cerate are shown and compared to previous measurements. Impedance spectroscopy is used to characterise the conductivity as a function of temperature and partial pressures of oxygen and water vapour in calcium doped samarium titanate, lanthanum magnesium titanate and strontium cerate doped with yttrium and nickel.

Concentration cell measurements were used to estimate transport numbers for protons and oxide ions in yttrium doped strontium cerate and calcium doped samarium titanate. Furthermore, the voltage of a concentration cell with hydrogen on one side and deuterium on the other was examined as a function of temperature.

Results of flux measurements on strontium cerate doped with yttrium or yttrium and nickel are presented and compared to theoretically calculated fluxes and results of similar studies in literature.

Dansk resumé

Grundet blandt andet den globale opvarmning er det nødvendigt at finde alternativer til det nuværende forbrug af fossile brændstoffer. Oxidmaterialer med høj ledningsevne af protoner vil kunne finde andvendelse indenfor mange teknologiske områder i et samfund baseret i højere grad på bæredygtigt energi. Materialer der også er elektroniske ledere kan finde brug i brintpermeable membraner, hvilket er emnet for denne afhandling.

Afhandlingen fokuserer på eksperimentelle aspekter af udviklingen af nye membranmaterialer. Den bagvedliggende teori er gennemgået, og tre primære måder at undersøge potentielle materialer bliver præsenteret, med fokus på hvordan de specifikt kan udnyttes i forbindelse med materialer med blandet protonisk og elektronisk ledningsevne; konduktivitetsmålinger, koncentrationscellemålinger og fluxmålinger.

Experimentelle resultater opnået med de tre metoder vil også blive præsenteret.

Jævnstrøms konduktivitetsmålinger på yttriumdoteret strontium cerat præsenteres og sammenlignes med tidligere målinger. Impedans spektroskopi benyttes til at karakterisere ledningsevnen som en funktion af temperaturen og partialtrykket af oxygen og vanddamp i calciumdoteret samariumtitanat, lanthan magnesium titanat samt strontium cerat doteret med yttrium og nickel.

Koncentrationscellemålinger blev benyttet til at estimere transportnumre for protoner og oxid-ioner i yttriumdoteret strontium cerat og calciumdoteret samariumtitanat. Desuden blev spændingen over en koncentrationscelle med brint på den ene side og deuterium på den anden som en funktion af temperatur undersøgt.

Resultater af fluxmålinger på strontium cerat doteret med yttrium og med yttrium og nickel præsenteres og sammenlignes dels med teoretiskt beregnede brintfluxe, dels med lignende målinger rapporteret i litteraturen.

Index

1. Introduction

1.1. Rationale and outline

Throughout the last few decades, environmental issues have been given ever increasing attention from scientists, media, politicians and the general public
[1-2]. Which specific topics have been the most prominent in the debate has varied, but in more recent time, global warming and climate change have been the centre of attention. While the question of whether global warming is caused by mankind - or indeed taking place at all, has been a matter of contention for perhaps too long, this now appears to be the consensus, at least among scientists. Action needs to be taken to reduce greenhouse gas emissions and limit global warming as much as possible, or the consequences are potentially catastrophic.

Carbon dioxide, being a strong greenhouse gas [3], needs to be released to the atmosphere at significantly reduced levels. The most obvious solution is to reduce the use of fossil fuels, both through reducing energy consumption and by moving towards sustainable energy sources.

The environment is not the only reason to move away from fossil fuels. These fuels are not renewable, meaning that at some point, they will run out. Current predictions indicate that coal reserves are still large and will last well over 100 years and natural gas supplies approximately 60 years at the current rate of use [4-5] For oil, the case is different, and we have very likely already reached “peak oil”, the point in time when global oil production is at its highest [6], as seen in Figure 1.

New oil sources may be discovered, and new technology may make it possible to extract more oil from already known sources. Most models of future oil supply already attempt to factor this in, and even if predictions are exceeded this will only delay the inevitable. While supplies are dwindling, demand is increasing as the living standards in developing countries rise and world population grows, further stressing the need for developing alternatives to fossil fuels quickly.

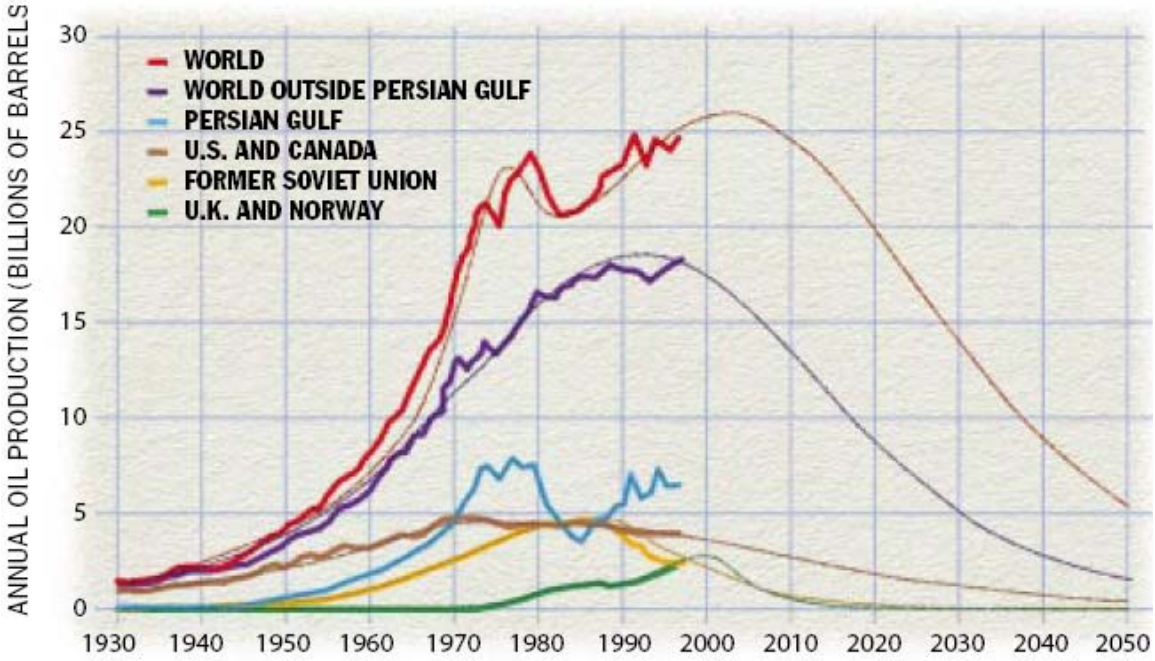

Figure 1 Prediction of world oil production [6]

Another concern is the geographical location of the remaining oil sources. A lot of is it situated in politically unstable or repressive areas of the world. Depending on repressive regimes for vital energy deliveries is obviously undesirable. Other sources are located where they are difficult or costly to utilise. The recent deep-well disaster in the Mexican gulf shows that off shore drilling is not unproblematic. Other types of sources, such as bituminous sand ("oil sand") and shale oil require large amounts of energy to extract and refine and the environmental impact of the extraction is severe compared to that of oil drilling. The Energy Return on Investment, EROI, for such sources is typically as low as 1.5-4 [7-8].

All in all, the case for moving away from fossil fuels and towards renewable alternatives is very strong. However, the alternatives are still more expensive than coal, and are not always available at the time and place where they are needed. Solar power is not available during night time and is limited in overcast weather, hydropower is only harvestable where a sufficiently energy rich body of water exists, and wind turbines will not function on calm days. Times of high output do not necessarily fit with times of high demand. Powering the transport sector poses an interesting problem of its own, since the power supply here must be transportable. Current battery technology does not provide

power densities that are practically useful for applications other than personal transport over short distances [9]. Producing renewable energy is not enough; we must also be able to store it for when it is needed and transport it to where it is required.

One solution model is the so called hydrogen society, or hydrogen economy. Excess electrical energy is converted to chemical energy in the form of hydrogen through the electrolysis of water. The hydrogen can be converted back to electrical energy through fuel cells when and wherever needed. While this idea is simple on the surface, a lot of challenges must be overcome before it is practically realisable. Every conversion step naturally incurs a loss of energy. Hydrogen is not easily storable or transportable in gas form, due to the low mass and small size of the molecules. Also, reaching energy densities that are competitive with those of liquid fuels for the transport sector requires compression or liquefaction, which again requires energy. Storage of hydrogen at several hundred bars of pressure or in a liquid state also puts some very strict demands on the storage containers. As an alternative to storing molecular hydrogen, a lot of research is directed towards finding materials which can incorporate hydrogen, such as metal hydrides. While a lot of progress has been made in the field, further work is still required to achieve the desired energy density, weight percentage of hydrogen, reversibility and kinetics of the hydrogen uptake, etc. [10]. Another approach is using the hydrogen along with for example captured CO_2 to produce hydrocarbons that are easier to store, transport and use [11].

High temperature protonic conducting oxides are potential candidates for use in a lot of the processes involved in this new energy situation, regardless of whether the preferred energy vector is hydrogen or one of the alternatives. Purely protonic conductors can be utilised in electrolysers and fuel cells. Mixed protonic-electronic conductors are candidates for hydrogen membranes. Such materials are the main focus of this work, and have numerous possible applications, both in a fully developed hydrogen economy and in the transition towards it, a subject which will be discussed in a later chapter.

The experimental work for this thesis has been carried out in full at the Fuel Cells and Solid State Chemistry Division of Risø Laboratory for Sustainable Energy, Technical University of Denmark. The division has previously been involved in international research projects in the field of high temperature protonic conductors in the time period

between 1994 and 2003. After a short break, an effort to get back in the field was made in the division by funding two Ph.D. scholarships concerning hydrogen membranes; one more theoretical in nature, utilising density functional theory to calculate atomic level behaviour of protons in oxides, and one more experimental in nature, the end result of which is the present work.

Initially, this project was envisioned to encompass characterisation of a wider range of materials as well as fabrication and testing of actual membranes of promising candidate materials.

Already in the early stages of the project, it became apparent that before attempting to undertake tests of a larger range of materials, a deeper understanding of the basics of protonics was necessary. Therefore, the focus has moved from characterising materials and optimising properties to understanding how best to perform that task. Thus, the main effort has been devoted to the defect chemistry and transport properties of proton conducting ceramics, and the impact of these on the results of commonly performed electrochemical measurements and the requirements these place upon experimental design.

This thesis will first treat the relevant background material in chapter 1, including a brief history of high-temperature protonics, a treatment of the relevant defect chemistry and theory of electrochemical transport. Applications for mixed protonic electronic conductors will be outlined, and the technical demands on applicable materials will briefly be touched upon.

After a full introduction to the topic, the experimental work will be presented and discussed, explaining the specific measurement methods and experimental set-ups used, as well as the results obtained. First, simple conductivity measurements (chapter 2) will be discussed. Results on the well known perovskite system $SrCe_{1-x}Y_xO_{3-\delta}$ (SCY) will be treated in chapter 2.1, and some preliminary results on the mixed perovskite La_2MgTiO_6 in chapter 2.2. The concentration cell electromotive force (EMF) method will then be examined, discussing the method itself, corrections for electrode polarisation resistance, findings on SCY and the pyrochlore system $Sm_{2-x}Ca_xTi_2O_7$ in chapter 2.3, and finally isotope effects in high temperature proton conductors, and their implications for the EMF method in chapter 4. The material on electrode polarisation resistance, results on SCY

and isotope effects was presented at the 14th International Conference on Solid State Proton Conductors in Kyoto, Japan, 2008 and the former two published in the special conference proceedings issue of Solid State Ionics. Conductivity and EMF measurements on $Sm_{2-x}Ca_xTi_2O_7$ were conducted in cooperation with University of Gothenburg, and published in Journal of Solid State Electrochemistry. Results on nickel-doped SCY will be presented in chapter 2.3. A method for measuring hydrogen flux will be presented in chapter 5, and results of such measurements will be shown and compared to literature data. Finally, a short summary will be given, along with suggestions for further work in chapters 7 and 8.

The two papers that have been published as a part of this work are given as appendices at the end of the thesis.

It is our hope that the material presented here can contribute to a deeper understanding of and assist in future efforts within the field of protonics and hydrogen transport membranes in particular.

1.2. Background

1.2.1. A brief history of high temperature protonics

The presence of hydrogen in oxides has been known since the 1950s, where it was noted that reduction of ZnO in hydrogen led to dissolution of protons in the oxide [12]. During the 70s, some measurements were made on hydrogen permeability of oxides, but the intended use of the materials was as tritium barriers in nuclear applications. BeO and Al_2O_3 were investigated, and the hydrogen permeation found to be smaller than in metals. It was also noted that the permeability of alumina increased when it was acceptor doped with 0.2 % MgO, thus decreasing its usefulness as a hydrogen barrier [13-14].

The first reports of high proton conductivity in oxides at high temperature came in the early 1980s by Iwahara et al., who found that indium doped strontium zirconate is a proton conductor in hydrogen containing atmospheres [15]. This material has since found technological application as a high temperature hydrogen sensor [16]. In the following years, this area was further explored. Other, similar perovskite materials were also investigated and found to show proton conductivity, with acceptor doped strontium cerate [17-19], barium cerate [20-24] and barium zirconate [25-26] being some of the most promising early candidates. Of these, solid solutions of barium cerate and zirconate still gets a lot of attention as high conductivity pure protonic conductors [27-31,70], while various strontium cerates have been investigated as mixed protonic-electronic conductors [32-41], see also chapters 5 and 6.

While new materials were being explored, the nature of the hydrogen in the oxides and the conductivity processes were also being investigated further. Using IR-spectroscopy, it was shown that the protons reside in the electron cloud of the oxygen [42-43]. This led to some speculation that they might also be transported as OH^- units in a vehicle transport mechanism [44]. Through a variety of methods, including quasielastic neutron scattering [45], analysis of the exit gas of a fuel cell [46], the sign of a concentration cell method experiment [47] and ^{18}O-tracer diffusion [48], the proton conductivity was shown to take place by the Grotthus mechanism [49]. This mechanism involves two separate steps,

rotation of the proton around an oxygen, and transfer between oxygen atoms as shown in Figure 2.

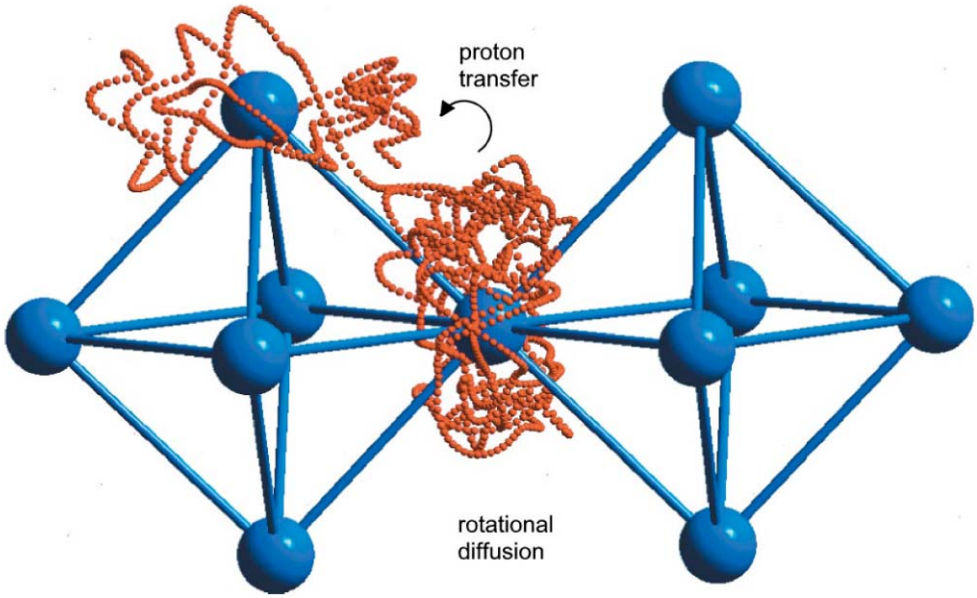

Figure 2 Proton transport in a perovskite [67]

In the mid-1990s, several mixed perovskites (see next chapter) were investigated for proton conductivity, of which off-stoichiometric $Ba_3CaNb_2O_9$ showed the highest conductivity [50-51].

Several non-perovskite mixed oxides containing tetrahedral structural units have also been found to show promising levels of proton conductivity. Acceptor doped lanthanum orthophosphate [52-54] and several other lanthanide phosphate [55-57] compounds were the first in this group to be investigated. $LaNbO_4$ was found to have higher conductivity than the phosphates [58-59], although it is limited by the low solubility limit of dopants. Recent studies have shown that compounds in the system $La_{1-x}Ba_xGaO_4$ is both an oxide ion and proton conductor, with protonic conductivity higher than that of both niobates and phosphates [60-61].

Conductivity versus inverse temperature plots of some well known proton conductors are shown in Figure 3. As can be seen in this figure, some of the very first perovskites that were shown to be proton conductors remain the ones with highest conductivity over a wide temperature range to this day.

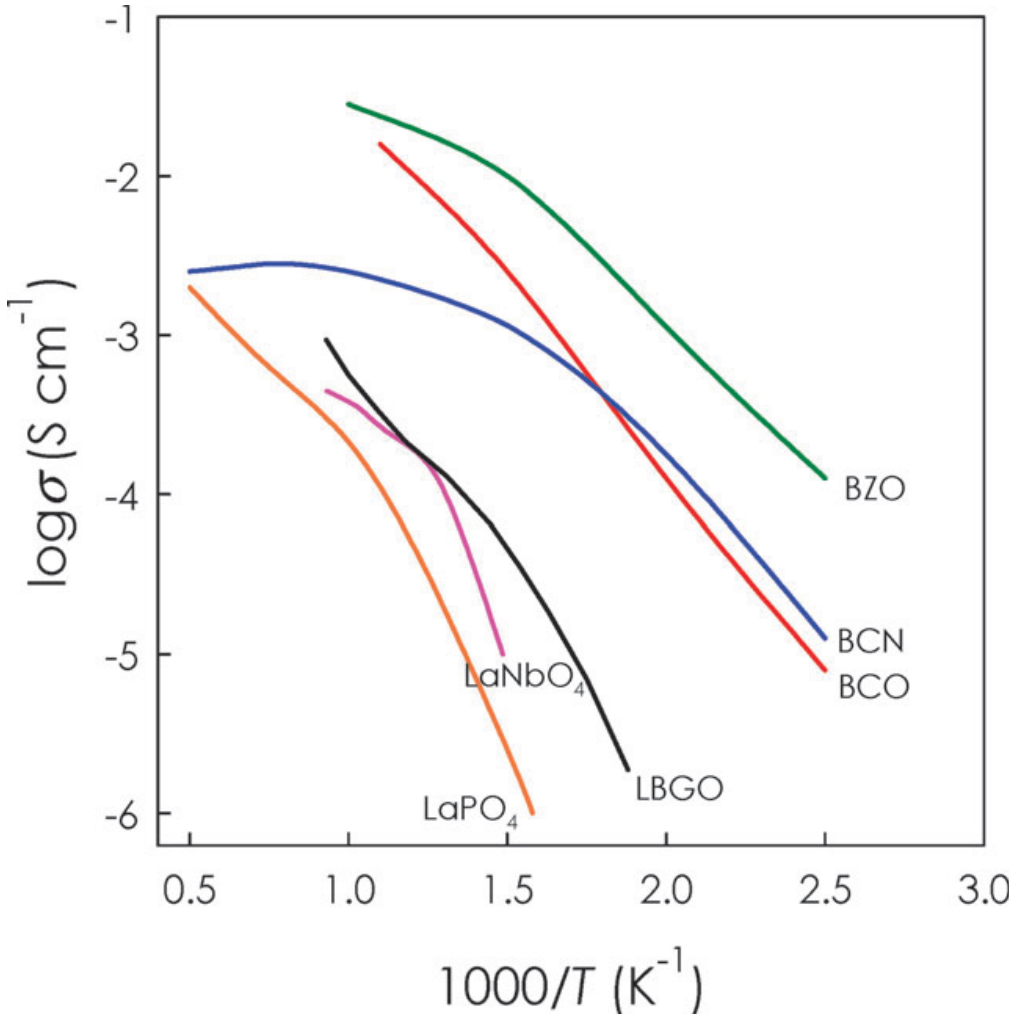

Figure 3 Conductivity versus inverse temperature of some well known proton conductors; $BaCe_{0.9}Y_{0.1}O_3$ (BCO), $BaZr_{0.8}Y_{0.2}O_3$ (BZO), $La_{0.9}Sr_{0.1}PO_4$, $Ba_3Ca_{1.18}Nb_{1.82}O_{8.73}$ (BCN), $La_{0.99}Ca_{0.01}NbO_4$ and $La_{0.8}Ba_{1.2}GaO_{3.9}$ (LBGO) [69]

Several excellent reviews on proton conducting oxides have also been written throughout the period of time where they have been studied, each treating aspects of the materials and their properties more in depth than we have done here [62-70].

1.2.2. Perovskites and related structures

As seen in the last chapter, a lot of known protonic conducting oxides have the perovskite structure. Since most of the materials explored during this work are also perovskites, the structure family will be briefly discussed here.

The general perovskite formula is ABO_3, where A is typically a large (alkali, alkaline earth or rare earth) metal ion and B is a transition metal ion. The name comes from the mineral perovskite, with the chemical formula $CaTiO_3$. The ideal perovskite structure is cubic, consisting of corner-sharing BO_6-octahedra at the corners of the cube and the A-ion at the body centre, see Figure 4.

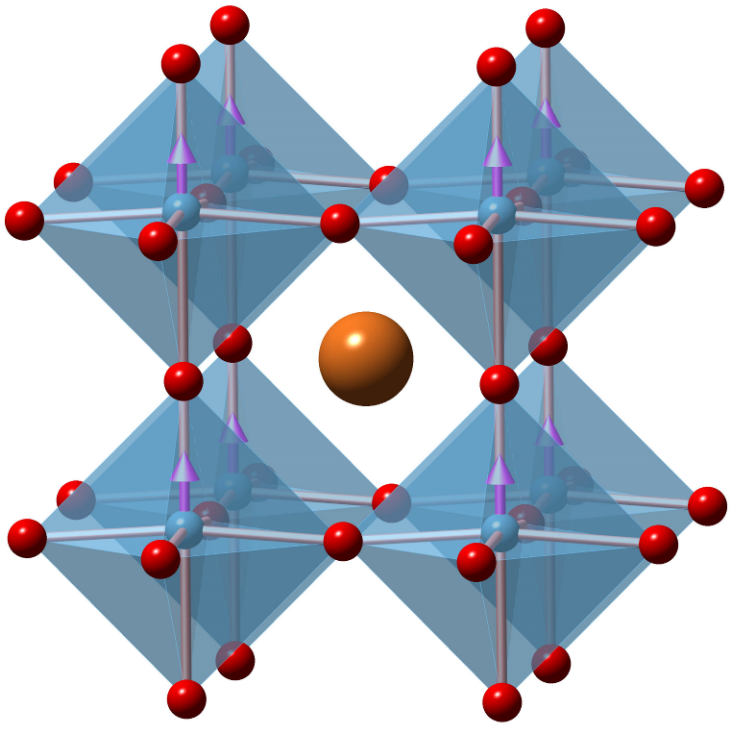

Figure 4 The perovskite structure with the larger A-site ion shown in orange, the B-site ion and its coordination octahedra in blue and oxygen in red.

The perovskite structure is very versatile, and many members of the family have found technological use within a wide variety of fields. Much of this versatility stems from the resilience of the structure to variations in both atomic composition and form. Perovskites

tolerate fairly large amounts of dopants on either A- or B-site, and the structure is frequently distorted into lower symmetry than the ideal cubic one by tilting of the BO_6-octahedra to accommodate A-site ions that do not fit in the ideal structure. For example, $BaZrO_3$ is cubic [71], $BaCeO_3$ is has a small orthorhombic distortion [72-74], and $SrCeO_3$ a stronger deviation from the cubic structure [72-74], leading to different oxygen sites. The (bulk) protonic conductivity of the acceptor doped oxides also varies in that order, with $BaZrO_3$ having the highest, and the difference in structure is probably at least part of the reason [67, 74].

In addition to regular doping, up to full range solid solutions, mixed perovskites are known with fixed stoichiometric amounts of two different A- or, more commonly, B-site ions. If there is a pronounced size or charge difference between the two species, these will usually be ordered on alternating sites, creating a so-called double perovskite. This name stems from the fact that the unit cell must be doubled to take the ordering into account. The difference in charge and size between B-site ions can lead to trapping of other defects, negatively influencing the conductivity. As mentioned in the previous chapter, the most successful double perovskite proton conductor to date is BCN18.

Apart from regular perovskites, there are a number of related structures. One interesting example is the Ruddlesden-Popper phases with general formula $A_{n+1}B_nO_{3n+1}$. The structure of these compounds is layered, comprising alternating perovskite and rock salt (AO) layers. The Ruddlesden-Popper type structure with n = 1, commonly referred to as K_2NiF_4 structure, is frequently created in small amounts in perovskites with an excess of the A-site ion. Little literature exists about proton conductivity in Ruddlesden-Popper phases. Some proton conductivity was reported in indium doped Sr_2TiO_4 and $Sr_3Ti_2O_7$, although lower than in the parent perovskite, $SrTiO_3$ [75]. Several members of this compound family have been found to have mixed oxide ionic-electronic conductivity, making them useful as oxygen membrane and SOFC electrode materials [76-78].

A second interesting perovskite related family is the $A_nB_nO_{3n-1}$ series, with perovskites as one end member at $n = \infty$ and brownmillerites, with the general formula $A_2B_2O_5$ at the other end with n = 2. The brownmillerite structure can be described as a perovskite with one sixth of the oxygen sites vacant, ordered in rows along the [101] direction in every other layer, or as a sequence of alternating BO_6 octahedra and parallel chains of BO_4

tetrahedra. At high temperature, the ordering of vacancies can be removed. This large amount of oxygen vacancies creates a situation where, at low temperature, a significant concentration of protons can be incorporated as discussed below (depending on the enthalpy of proton uptake), but their mobility is too low for the material to have a high protonic conductivity due to the ordering. As the temperature increases, the mobility, and hence the conductivity, increases as the ordering is lifted, until a temperature is reached where proton defects are unfavourable and oxide ionic conductivity takes over. Alternatively, the temperature where protons become thermodynamically disfavoured is lower than the temperature at which disorder is favoured, and the material will likely not have a range in which it is a good proton conductor.

The most thoroughly studied brownmillerite type compound that has been shown to have proton conductivity is $Ba_2In_2O_5$ [79-81], although protons are only the main carrier up to around 300 °C, where oxide ion conductivity takes over.

While not being directly related to the perovskite structure, the pyrochlore structure still shares some features of the brownmillerites, in that it is an inherently oxygen deficient structure with BO_6 octahedra as the principal building block. It is a superstructure derivate of the fluorite structure, with the general formula $A_2B_2O_7$. A- and B-site ions are ordered along the [110] direction. The oxygen vacancies of the pyrochlore structure as compared to the fluorite structure are also ordered in the ideal pyrochlore structure, but like in brownmillerites, this ordering may be lifted. Acceptor doped $La_2Zr_2O_7$ is a well known proton conductor [82-85], and recently, pyrochlore structured titanates and stannates of some lanthanides have also been shown to have protonic conductivity [86-88].

To predict which crystal structure a given material will take, numerous factors will have to be taken into account. Giaquinta and zur Loye [89] name interactions such as Coulombic, electronic and steric will all influence the structure. For the perovskite structure, however, a set of simple rules relating the ionic radii of the metal and oxide ions to the formability of the structure exist. The most well known is the tolerance factor suggested by Goldschmidt in the 1920's [90], stating that the ionic radii of the A-site, B-site and oxide ions (r_A, r_B and r_O respectively) have a tolerance factor t_G:

$$t_G = \frac{r_A + r_O}{\sqrt{2}\left(r_B + r_O\right)} \quad (1)$$

For the ideal, cubic perovskite structure, t_G is 1, but perovskites in the range t_G = 0.75-1 are known. As shown by Li et al. [91], the Goldschmidt tolerance factor is a necessary but insufficient criterion for perovskite formation. Since the BO_6-octahedron is the basic building block of the structure, it too must be stable. This gives us the octahedron factor

$$\frac{r_B}{r_O} \geq 0.425 \quad (2)$$

Both these factors are derived from structural parameters of materials at room temperature and normal pressure, and therefore also apply at those conditions.
An alternative way to state the demands on ionic radii is [92]

$$\begin{aligned} 1.00\,\text{Å} < r_A < 1.69\,\text{Å} \\ 0.57\,\text{Å} < r_B < 1.02\,\text{Å} \end{aligned} \quad (3)$$

1.2.3. General defect chemistry

All crystalline solids contain imperfections, deviations from their ideal structure, termed defects [93]. Although their concentrations are usually very small, they can have tremendous impact on the properties of the material. Indeed, since protons are not a native part of the oxides studied here, but are defects in their lattice, defect chemistry is an integral part of this work. A good understanding of the defect chemistry of the materials is necessary to understand and predict material and transport properties, and to aid in interpretation of experimental results.

Although two-dimensional defects, such as grain boundaries, play a significant role in, for example, conductivity, this chapter will be focused on zero-dimensional defects, or point defects. Such defects occupy specific sites in the crystal lattice, and include e.g. vacancies, interstitial atoms and dopants.

A full defect chemical model involves selection of the relevant defect chemical species to be treated, then setting up the same number of linearly independent equations using for example mass action laws, site balances and electroneutrality conditions. For simple systems, analytical solutions can often be found, while numerical methods are required to solve more complex systems, as described in [94-99].

As an example, let us consider a typical oxide based proton conductor, a B-site acceptor doped perovskite with divalent A-site and tetravalent B-site cations. The species that are most relevant to consider for proton conducting perovskites are usually, using Kröger-Vink notation:

$$\text{Acceptor dopant on the B-site} : M_B^{'}$$
$$\text{Oxygen vacancy} : V_O^{\bullet\bullet}$$
$$\text{Protonic defect} : OH_O^{\bullet}$$
$$\text{Electron hole} : h^{\bullet}$$
$$\text{Electron} : e^{'}$$
$$\text{Normal oxide ion} : O_O^{x}$$

Since the protons always reside in the vicinity of the oxygen in the lattice, protonic defects will be described as a hydroxide ion on the oxygen site, rather than an interstitial proton, $H_i^{\bullet}$. Whether these assigned integer charges are actually physically correct is doubtful. Recent ab initio calculations, so called Bader charge analysis, showed that the charge of "protons" in some perovskites e.g. $SrTiO_3$, $CaTiO_3$ and $SrZrO_3$ is 0.56-0.60 *e*, and that of oxide ions -1.17 *e* [100]. These values are much closer to the covalent charges seen, for example, in water, than the typical fully ionic integer values normally given. Possibilities of the presence of neutral and even negatively charged hydrogen in oxides

have also been discussed [68, 101]. For this work, however, the traditional single charge proton and double charge oxide ion will be assumed.

For a full treatment, various metal ion defects will also need to be taken into account:

Regular A-site cation : A_A^x

Regular B-site cation : B_B^x

A-site vacancy : $V_A^{''}$

B-site vacancy : $V_B^{''''}$

B-site cation on the A-site : $B_A^{\bullet\bullet}$

A-site cation on the B-site : $A_B^{''}$

B-site dopant on the A-site : $M_A^{\bullet}$

This treatment still does not take oxygen or metal interstitials into account, nor does it account for different oxygen sites in lower symmetry perovskites. Even so, we have 13 species for which to calculate concentrations, clearly a complex problem that requires numerical methods to solve completely.

In most cases, the concentration of the majority of these species will be negligible and have no influence on material properties. Their existence should be kept in mind though, since this might be the key to otherwise inexplicable results.

To ease the burden of calculation, a simplified approach can then be taken, where only the dominant defects are considered in the electroneutrality condition for a given set of conditions. The concentration of the minority defects can then be sequentially calculated from the defect equilibria, the most relevant and general for all materials investigated of which will be shown here.

Oxygen vacancies can be created through interaction with gaseous oxygen:

$$O_O^X \Leftrightarrow 1/2 O_{2(g)} + V_O^{\bullet\bullet} + 2e^{'}$$
$$K_O = p_{O_2}^{1/2} \left[V_O^{\bullet\bullet} \right] n^2 \qquad \textbf{(4)}$$

where K_O is the oxidation equilibrium constant. The internal electronic equilibrium is given by

$$nil \Leftrightarrow e' + h^{\bullet}$$
$$K_e = np \qquad \textbf{(5)}$$

with K_e being the internal electronic equilibrium constant and n and p the concentrations of electrons and electron holes. In hydrogen containing atmospheres, the material can be reduced creating protonic defects, K_{H_2} being the hydrogen reduction equilibrium constant:

$$2O_O{}^X + H_{2(g)} \Leftrightarrow 2OH_O{}^{\bullet} + 2e'$$
$$K_{H_2} = \left[OH_O{}^{\bullet}\right]^2 p_{H_2}^{-1} n^2 \qquad \textbf{(6)}$$

Protonic defects can also be introduced through interaction with water vapour (or indeed any species containing hydrogen, although water vapour is the only species apart from molecular hydrogen considered here):

$$V_O{}^{\bullet\bullet} + O_O{}^X + H_2O_{(g)} \Leftrightarrow 2OH_O{}^{\bullet}$$
$$K_{H_2O} = \left[OH_O{}^{\bullet}\right]^2 p_{H_2O}^{-1} \left[V_O{}^{\bullet\bullet}\right]^{-1} \qquad \textbf{(7)}$$

where K_{H_2O} is the equilibrium constant for uptake of water. The equation for uptake of water can also be found by subtracting the oxidation equation and adding the gaseous equilibrium equation between water, hydrogen and oxygen to the equation for reduction and proton creation with hydrogen:

$$H_2O_{(g)} \Leftrightarrow ½O_{2(g)} + H_{2(g)}$$
$$K_g = p_{O_2}^{½} p_{H_2} p_{H_2O}^{-1} \quad \textbf{(8)}$$

where K_g is the gas phase equilibrium constant for dissociation of water.

The fact that entropy, enthalpy and Gibb's free energy are all state function allows us to make some general statements on the two proton creation reactions. They both involve a gas phase species being incorporated into a crystal lattice, which means the entropy term will be dominated by this phase change. The same number of gaseous molecules is involved in both reactions, and the entropy change should therefore be roughly equal. Accordingly, the difference in Gibb's free energy change for the two reactions should be determined principally by the reaction enthalpies. The enthalpy change for water dissociation (since that is the direction in which the gas equilibrium equation is written) is 241.82 kJ/mol. If the enthalpy of reduction for the oxide is greater, protonation via water vapour will be favourable compared to protonation via hydrogen. This is the case for most oxides, and this explains why the reaction with water is the one most often given in literature even though both equations are equally correct.

Going back now to the defect chemistry, and still using a II-IV perovskite with a trivalent B-site dopant, the "full" electroneutrality equation (taking only the most relevant species into account) is:

$$\left[M_B^{'}\right] + n = 2\left[V_O^{\bullet\bullet}\right] + p + \left[OH_O^{\bullet}\right] \quad \textbf{(9)}$$

If the doping level is significant, the concentration of oxygen vacancies will be dominated by the concentration of the dopant rather than by the intrinsic reduction. Under dry conditions, where protonic defects will be negligible, a simplified electroneutrality condition can be written as

$$\left[M_B^{'}\right] = 2\left[V_O^{\bullet\bullet}\right] \quad \textbf{(10)}$$

Since the concentration of the dopant is assumed to be fixed from the synthesis of the material, the concentration of oxygen vacancies does not change either. The concentrations of electrons and holes can be calculated from the oxidation and internal electronic equilibrium constants:

$$K_O = p_{O_2}^{½}[V_O^{\bullet\bullet}]n^2$$
$$\Updownarrow$$
$$n \propto p_{O_2}^{-1/4}$$
$$\Updownarrow$$
$$p \propto p_{O_2}^{1/4} \qquad \textbf{(11)}$$

If the material is sufficiently reduced, especially if the concentration of the dopant is not very high, a situation may arise where electrons take over as the species charge compensating oxygen vacancies. The simplified charge neutrality condition is then

$$n = 2\left[V_O^{\bullet\bullet}\right] \qquad \textbf{(12)}$$

This leads to p_{O_2} dependencies as follows, again from the oxidation and internal electronic equilibrium constants:

$$K_O = p_{O_2}^{½}[V_O^{\bullet\bullet}]n^2 = \frac{1}{2}p_{O_2}^{½}n^3$$

$$\Updownarrow$$

$$n \propto p_{O_2}^{-1/6}$$

$$[V_O^{\bullet\bullet}] \propto p_{O_2}^{-1/6} \qquad \textbf{(13)}$$

$$\Updownarrow$$

$$p \propto p_{O_2}^{1/6}$$

These dependencies are visualised in a Brouwer diagram in Figure 5.

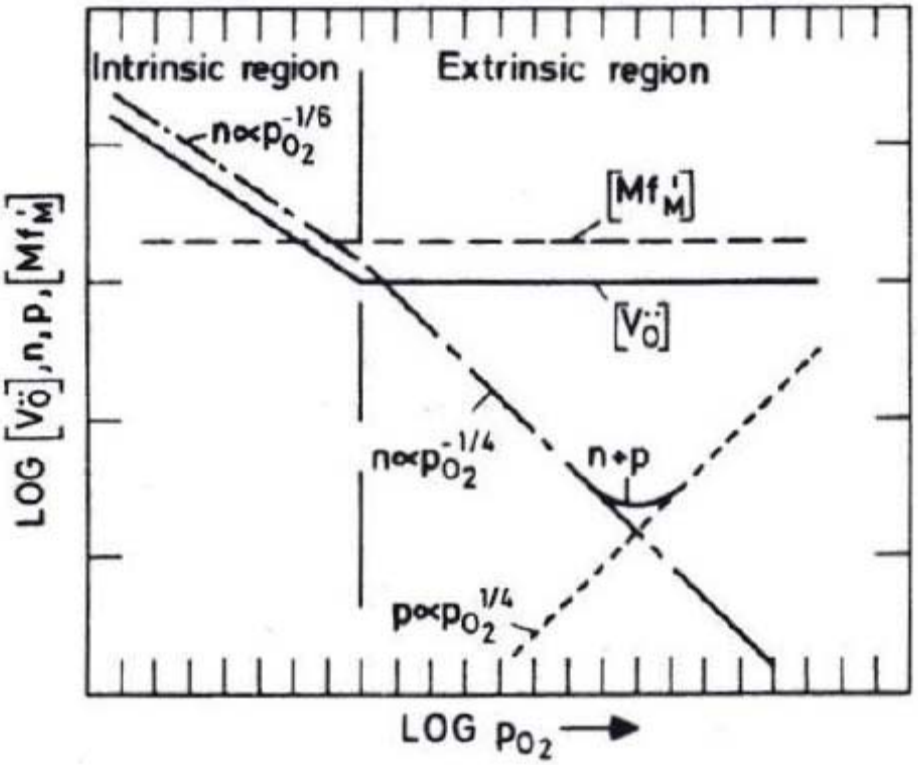

Figure 5 Brouwer diagram for an acceptor doped oxide, showing the concentrations of defects as a function of oxygen partial pressure [93]

Similarly at high $p_{O_2,}$ electron holes may be the species compensating the dopant.

$$\left[M_B^{'}\right] = p \tag{14}$$

In this case, the concentration of electron holes, and therefore electrons is fixed, which means the concentration of vacancies decreases as $p_{O_2}^{-½}$.

As described above, introduction of water vapour leads to creation of protonic defects. Assuming again that oxygen vacancies charge compensates the dopant, the concentration of protonic defects is related to the water vapour partial pressure as follows:

$$K_{H_2O} = \left[OH_O^{\bullet}\right]^2 p_{H_2O}^{-1} \left[V_O^{\bullet\bullet}\right]^{-1}$$
$$\Updownarrow$$
$$\left[OH_O^{\bullet}\right] \propto p_{H_2O}^{½} \tag{15}$$

Since no reduction or oxidation takes place, the concentration of electronic defects remains constant. As the concentration of protonic defects increases, they will eventually surpass oxygen vacancies as the species charge compensating the dopant, saturating the material with protons.

$$\left[M_B^{'}\right] = \left[OH_O^{\bullet}\right] \tag{16}$$

This leads to the following p_{H_2O} dependencies for the other species:

$$[V_O^{\bullet\bullet}] \propto p_{H_2O}^{-1}$$
$$n \propto p_{H_2O}^{½}$$
$$p \propto p_{H_2O}^{-½} \tag{17}$$

Note that while there are still no redox processes occurring, the concentration of electronic defects now change as a function of water vapour partial pressure, via the oxygen vacancies.

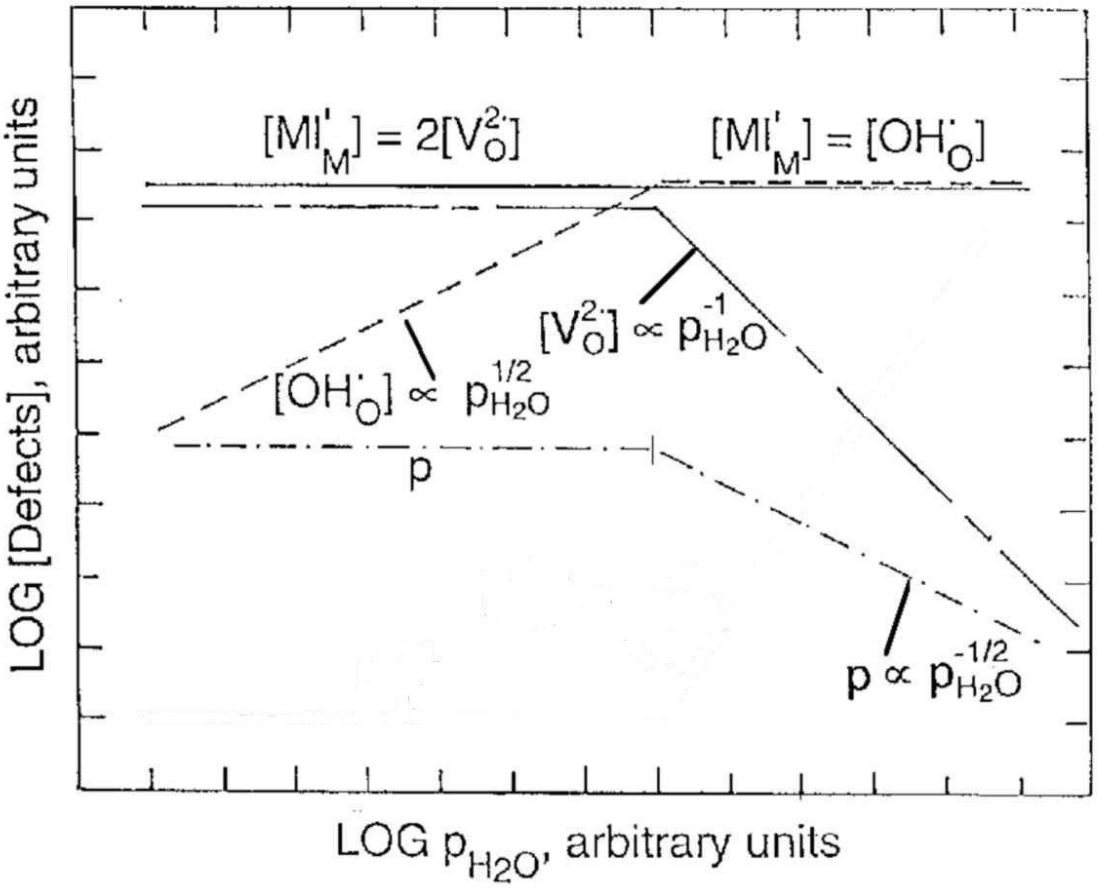

Figure 6 Brouwer diagram for an acceptor doped oxide, showing the concentration of defects as a function of water vapour partial pressure, adapted from [93]

Naturally, in between partial pressure ranges where one of these simplified electroneutrality conditions is a good approximation, there will be transition ranges, where the partial pressure dependencies of the defect species are not as simple as described above.

The above simple defect chemical model covers the most important species and reactions in high temperature proton conducting oxides, and will be assumed to apply to all the systems discussed in this work. Deviations from this model and necessary additions will be addressed as individual materials are discussed.

1.2.4. Conductivity, transport numbers, flux

The conductivity, σ_i, of a species i with charge z_i is directly proportional to its concentration, c_i, and mobility, u_i:

$$\sigma_i = z_i e c_i u_i \quad \textbf{(18)}$$

This allows us to correlate a conductivity measurement series to the defect chemistry of a material. The p_{O_2} dependency of the conductivity will not give us the concentrations and mobilities of the conducting species, but it will show which of the simplified electroneutrality conditions, if any, applies to the material under the given conditions. If, at a given temperature, the conductivity of an acceptor doped oxide shows no dependency on p_{O2}, it is likely to be dominated by ionic defects (protons or oxygen vacancies) compensating the dopant, and the conductivity measured will, therefore, be predominantly ionic. Measurements of conductivity versus water vapour partial pressure can determine whether oxide ionic or protonic conductivity is predominant. If the conductivity is proportional to $p_{O_2}^{1/4}$, ionic defects and dopants still dominate the concentrations, but the total conductivity is dominated by electron holes due to their higher mobility.

Measurements of conductivity versus temperature allows for calculation of the activation energy, E_a, for conductivity of a species as long as its concentration can be assumed to be constant.

The total conductivity of the material will be equal to the sum of the individual contributions:

$$\sigma_{tot} = \sum_i \sigma_i \quad \textbf{(19)}$$

The relative contribution that each individual conducting species, I, gives to the total conductivity is known as the transport or transference number, t_i, of that species.

$$t_i = \frac{\sigma_i}{\sigma_{tot}} = \frac{\sigma_i}{\sum_i \sigma_i} \quad \textbf{(20)}$$

The flux, j_i, of a charged species, i, in an electrochemical potential will, in one dimension, be given by

$$j_i = \frac{\sigma_i}{\left(z_i F\right)^2}\left[\frac{d\mu_i}{dx} + z_i F \frac{d\varphi}{dx}\right] \quad \textbf{(21)}$$

where μ_i is the chemical potential of i and φ is the electric potential. This gives rise to a partial current density, i_i

$$i_i = z_i F j_i = \frac{\sigma_i}{z_i F}\left[\frac{d\mu_i}{dx} + z_i F \frac{d\varphi}{dx}\right] \quad \textbf{(22)}$$

Since charge neutrality is required, this current must be counterbalanced, for example through an external circuit as will be the case in for example fuel cells. If no external circuit is present, the sum of all current densities must be zero. This allows us to relate the electrical potential gradient to the chemical potential gradient of all charge carriers using the transport number as defined above:

$$\frac{d\varphi}{dx} = -\sum_k \frac{t_k}{z_k F}\frac{d\mu_k}{dx} \quad \textbf{(23)}$$

The chemical potential of a charged species is not well-defined, and instead, the chemical potential of the corresponding neutral species must be used, assuming equilibrium between it and the charges species and electrons, yielding:

$$\frac{d\varphi}{dx} = -\sum_n \frac{t_n}{z_n F}\frac{d\mu_n}{dx} + \frac{1}{F}\frac{d\mu_{e^-}}{dx} \qquad \textbf{(24)}$$

where subscript *n* now denotes the neutral species.

The flux density of a single charges species accompanied by other charged species can be calculated as

$$j_i = \frac{-\sigma_i}{\left(z_i F\right)^2}\left[\frac{d\mu_i}{dx} - z_i \sum_k \frac{t_k}{z_k}\frac{d\mu_k}{dx}\right] \qquad \textbf{(25)}$$

Integrating over a sample thickness of L and performing again the substitution of neutral species for the charged ones in the chemical potentials, we obtain

$$j_i = \frac{-1}{\left(z_i F\right)^2 L}\int_I^{II} \sigma_i \left[d\mu_{n=i} - z_i \sum_n \frac{t_n}{z_n} d\mu_n\right] \qquad \textbf{(26)}$$

This is the most general form of the flux equation. We will now look at three specific cases that could be relevant in a material with the defect chemistry described in the previous chapter; one with electronic and oxide ionic conductivity, giving an oxygen transport membrane, one with protonic and electronic conductivity, which leads to hydrogen permeability, and finally a material with mixed protonic and oxide ionic conductivity showing permeability to water. The three materials are shown schematically in Figure 7. Here, the electronic conductivity is shown as electron holes, but for the sake of these equations, it doesn't matter whether it is actually holes or electrons running in the opposite direction. The sign of the charge will simply cancel out with the sign of the direction of the current. For material design, it naturally makes a huge difference, since the p_{O_2} dependencies of the two conductivities are inversely proportional.

The flux of oxide ions (which will of course be twice the oxygen flux) in the first material can be calculated as

$$j_{O^{2-}} = \frac{RT}{8F^2L}\int_I^{II} \sigma_{O^{2-}} t_{e^-} d\ln p_{O_2} \qquad \textbf{(27)}$$

For the hydrogen transport membrane, the flux of protons can be found using the following equation:

$$j_{H^+} = \frac{RT}{2F^2L}\int_I^{II} \sigma_{H^+} t_{e^-} d\ln p_{H_2} \qquad \textbf{(28)}$$

and for the water transport membrane

$$j_{H^+} = \frac{RT}{2F^2L}\int_I^{II} \sigma_{H^+} t_{O^{2-}} d\ln p_{H_2O} \qquad \textbf{(29)}$$

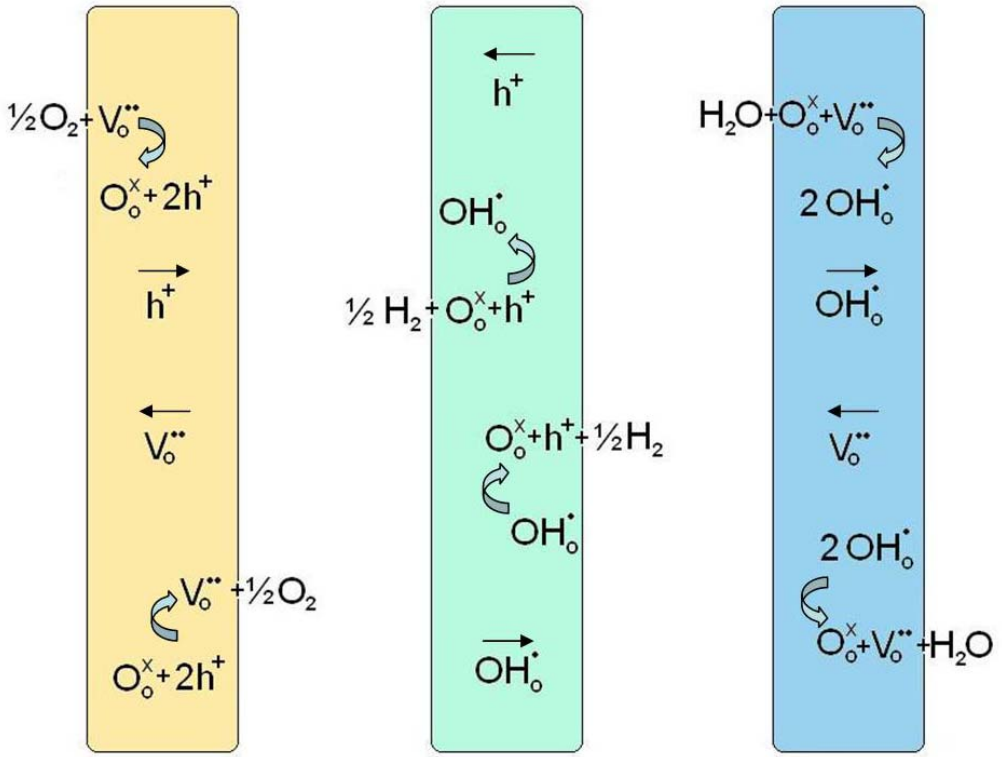

Figure 7 Three possible membrane materials, from left to right showing oxygen transport, hydrogen transport and water transport.

Common to all three equations is that they can easily be rewritten for the other species involved, and that the term to be integrated consists of a product of a conductivity and a transport number. This term, the ambipolar conductivity, can be rewritten (using the hydrogen membrane as an example):

$$\sigma_{H^+} t_{e^-} = \sigma_{tot} t_{H^+} t_{e^-} = \sigma_{e^-} t_{H^+} = \frac{\sigma_{H^+} \sigma_{e^-}}{\sigma_{tot}} \quad \textbf{(30)}$$

or, if protons and electrons are the only conducting species the more common form

$$\sigma_{ambipolar} = \frac{\sigma_{H^+} \sigma_{e^-}}{\sigma_{H^+} + \sigma_{e^-}} \quad \textbf{(31)}$$

Given that the flux depends on the ambipolar conductivity, it is clear that it is governed principally by the smaller of the two conductivities.

Norby and Haugsrud also give equations for proton flux in a material where oxide ion conductivity is present along with protonic and electronic conductivity [102] as well as solutions to the integral for given cases of dominating defects [102-103] which will not be repeated here.

1.2.5. Applications

Potential applications for high temperature proton conducting oxides are numerous [63]. Pure protonic conductors have found use in hydrogen sensors [104], and are investigated for use as electrolyte in fuel cells [69-70, 105-108] and electrolysis [17, 109].

As shown above, materials with mixed protonic electronic conductivity, specifically high ambipolar conductivity, will be able to transport hydrogen in a chemical gradient. This is interesting for several technological applications. The most obvious might be purification of hydrogen from e.g. syngas or coal gasification [110-111] or to concentrate hydrogen waste streams in e.g. refinery, hydrocarbon or metallurgy plants [112]. The large difference in conductivity between hydrogen isotopes, which will be discussed further below, means that hydrogen membranes can be used to separate hydrogen, deuterium and tritium, which has been discussed theoretically for oxide based membranes [63], and proven conceptually for metal based membranes [113-115]

Hydrogen membranes can conceivably also be used for non-galvanic steam dissociation.

Several literature studies also demonstrate use of ceramic hydrogen membranes for hydrogenation and dehydrogenation reactions [116], such as electrochemical coupling of methane to form ethane and ethylene [117-118] and reduction of NO_x [119-120]. Such applications introduce new challenges more related to catalysis, such as selectivity and resistance to surface poisoning.

Since the materials treated here only have an appreciable hydrogen flux at elevated temperatures, they can ideally be integrated in systems where other high temperature processes, preferably processes creating excess heat, already take place.

1.2.6. Materials for membranes

We have seen above that high ambipolar conductivity is desirable in materials for hydrogen membranes. We will now take a brief look at what other properties are necessary for making the materials technologically relevant, as well as what other technologies can be used for hydrogen separation.

The US Department of Energy has set a number of targets for hydrogen separation membranes to be reached by 2015, listed in Table 1.

Table 1 US DOE Targets for hydrogen separation membranes [121, 122], adapted from [123]

Characteristic	Units	2006 status	2015 target
Flux rate	$m^3/h/m^2$	61	91.5
Cost	$\$/m^2$	860	<1080
Durability	Years	0.9	>5
Operating temp.	°C	300-400	250-500
Parasitic power	kWh/1000 m^3	-	<100
ΔP oper. capability	Mpa	6.89	2.76-6.89
Hydrogen recovery	% of total gas	-	90
Hydrogen purity	% of total (dry) gas	99.99	99.99

As can be seen in this table, a lot of the targets have already been reached for some technologies. The areas that need the greatest improvement are the flux rate and the durability, and those will likely also be the largest obstacles for dense ceramic membranes. The flux rate is directly proportional to the ambipolar conductivity, which means materials with higher protonic conductivity are needed, and they must also exhibit electronic conductivity under the conditions of the given application. The targets of cost should be reachable for ceramic oxide membranes; oxides are generally low cost, although this is not the case some rare earth and transition metals that could be interesting, especially as dopants. In practice, the active membrane should also be a thin (to increase flux) dense layer on a porous substrate of an inexpensive oxide or metal.

Regarding durability, a lot of factors play in. For oxide based materials, reactivity with substrate materials, causing insulating phases must be avoided. For alkali/alkaline earth containing materials (e.g. strontium and barium) materials, reactivity with CO_2 and other components potentially present in the feed stream is also a problem [124-127]. Since the materials under consideration here are all mixed oxides, and will be operating in a gradient of p_{O_2} another problem for the long term stability could be cation migration. Finally, depending on the intended application, tolerance to thermal cycling and changes in p_{O_2} will also be required. In conclusion, it is clear that when ceramics that show

sufficient flux rates as produced have been found, it is likely that some effort will need to go into demonstrating and improving their long term durability.

The optimal operating temperature for perovskites and related systems is, in many cases, higher than those specified by the DOE in Table 1. This is not necessarily a disadvantage, since the higher operation temperature could be beneficial or even required for some applications, such as coal gasification and natural gas reforming, where Pd membranes may not be used. The purity of the hydrogen should, theoretically, be 100% as long as fully dense membranes can be produced, which gives it an advantage over some other technologies.

Of competing membrane technologies, the most prevalent are dense metallic membranes and nano- or microporous membranes [128]. In the former, the transport of hydrogen takes place by a process not entirely different from that found in oxide-based membranes, in that hydrogen atoms are dissociated and transported as ions and electrons (although the conduction mechanism is different) [129-130]. This leads to a flux proportional to the square root of the pressure difference, similar to what is found in oxide based membranes when protons are a minority defect. Traditionally, the metal used for hydrogen separation has been palladium and alloys thereof [131], which are very expensive. It combines a high permeability with sufficient resistance towards hydrogen embrittlement, the latter of which negatively affects the durability of the membrane [132-133]. Recently, progress has been made using alloys including metals that show a higher permeability to hydrogen but also a lower resistance to embrittlement than palladium, such as niobium and vanadium, potentially giving a significant price-decrease in metallic membranes [123].

In contrast to the two membrane types treated so far, microporous membranes function through size exclusion. Hydrogen molecules have a diameter of 2.83 Å. Membranes can be made either from materials that naturally have pores of the right size order, such as zeolites [134], or by careful control of the microstructure of e.g. using carbon [135], silica [136] or other materials. The materials used are cheap, and since the flux is of molecular hydrogen, the flux is directly proportional to the pressure difference. The disadvantage of microporous membranes is the fact that the pore size can not be controlled completely, and defects in the structure leads to lowered selectivity towards hydrogen.

2. Conductivity measurements

As shown above, conductivity measurements can give a wealth of data about a material. By performing measurements at a range of different temperatures and gas environments, much can be learned about the conducting species and the defect chemistry.

Conductivity measurements are performed by applying a current or potential to a sample and measuring the other, allowing for calculation of the resistance. From the dimensions of the sample the conductivity can be calculated.

Principally we can differentiate between two types of conductivity measurements, as determined by the type of signal applied; DC and AC measurements. Typical setups for the two types of conductivity measurements are shown in Figure 8. DC measurements are typically performed as a 4-terminal measurement on e.g. bars of the material to be investigated. Current is applied through electrodes at the end of the sample, and the voltage drop over two points in between are measured. These points should be placed far enough from the current electrodes that the current density at a cross section through the sample at the voltage probes is uniform, that is, fringing effects are avoided.

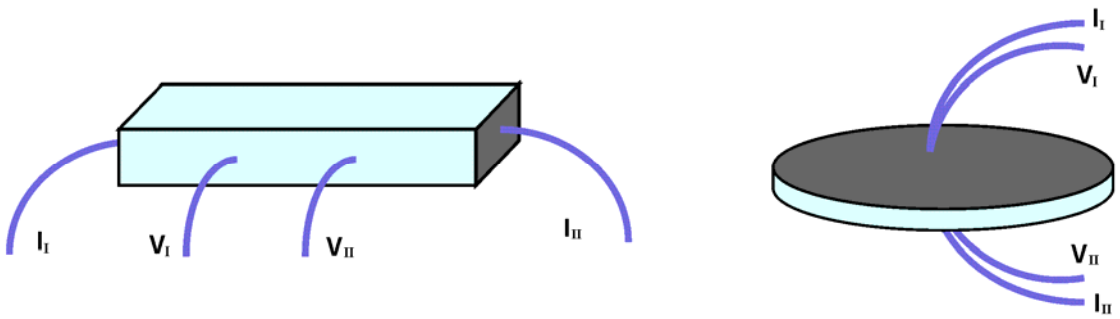

Figure 8 Diagrams of a DC (left) and AC (right) conductivity setup, showing the current and voltage leads. Dark grey areas represent electrodes.

The advantage of DC conductivity measurements is that it is a fast and straightforward method. However, it gives only a single, total conductivity for the sample. Contributions from electrode reactions and resistivity can not be discerned from the response from the sample itself. Nor can the effect of grain boundary resistance for the sample be found.

For these reasons, AC conductivity measurements are often preferred. As the name implies, an alternating, typically sinusoidal, signal is applied, and the complex impedance is measured. All processes giving a response have a characteristic frequency. This means that a conductivity measurement can be made where for example electrode reactions are not included, but only the resistance of the actual sample by using a high enough frequency. Alternatively, and perhaps more commonly, measurements can be performed over a frequency range, giving so called impedance spectroscopy. This is a very powerful technique, with which bulk and grain boundary can be separated, and electrode reactions studied in depth. A comprehensive treatment of the theory and applications of impedance spectroscopy is far beyond the scope of this work, but we will touch upon some of the points relevant to the experiments conducted. A fuller treatment is given in for example [137-138]. It has been well established that the frequency dependent response of an electrochemical system is identical to a hypothetical model circuit consisting of simple elements with well known electrical properties. While it is more precise to use the full Nernst-Planck-Possion equations to calculate the impedance, using an equivalent circuit to describe the processes giving the impedance allows for a much simpler and faster analysis of data, often without major loss of precision.

It should be noted that there is an infinite number of equivalent circuits that will give the same impedance at all frequencies, and that the more circuit elements are used in a model, the better a fit of measurement data can be achieved using the model. It is, however, important to retain some connection between the model and the actual physical processes taking place. A good approach is to use the smallest amount of circuit elements that give a reasonable fit.

One type of equivalent circuits that has been found to model conductivity measurements in solid samples well is the so called Voigt model, consisting of a number of subcircuits connected in series, each subcircuit consisting of a resistor and a capacitor in parallel. Since a typical polycrystalline solid sample is not uniform and has a finite volume, they are typically not perfectly described by point elements. Some frequency dispersion is expected. Therefore, the constant phase elements, denoted Q, are usually used instead of capacitors in the equivalent circuits. The impedance of a constant phase element is given by

$$Z = \frac{1}{Y^0 \left(j\varpi \right)^n}$$

For n = 1 this is the same as a capacitor. An equivalent circuit that describe mixed ionic electronic conductors specifically to great detail has been developed [139-140]. This model has been shown to match the exact impedance calculated using the Nernst-Planck-Poisson equations well over a large set of material parameters [139], and potentially allows for calculation of chemical diffusion coefficients, charge carrier concentrations and mobilities directly from impedance spectra [140]. Unfortunately, none of the data sets recorded in this work were suitable for fitting with this equivalent circuit model, and more traditional models were used.

Once a suitable equivalent circuit has been found, the data can be fitted using a complex non-linear least square (CNLS) fitting routine. Often, finding a suitable equivalent circuit and fitting the data is an iterative process, as the values found in one fit may reveal that the chosen circuit is not optimal. In this work, the program ZSimpWin 3.21 by Elchemia [141] was used to fit all impedance spectroscopy data.

From the Y_0, n and resistance value, the so called pseudocapacitance, or quasi equivalent capacitance (QEC) of a (RQ) subcircuit can be calculated using the formula

$$C = \frac{\left(RY_0 \right)^{1/n}}{R} \qquad \textbf{(32)}$$

This is useful for aiding in attributing the arcs to the correct processes. Typically, grain boundary conductivity has a QEC in the range of 10^{-9} F cm^{-2}, while values for bulk conductivity are usually around 10^{-11} F cm^{-2}.

A given measurement cell will always have some inductance due to leads. This influences results, especially at high frequency and on samples with low resistance. However, if the inductance due to leads is known, it is simple to correct for. For a given measurement at frequency *f*, the imaginary part of the impedance, $Z_{i,corr,}$ corrected for inductance, L_s, is

$$Z_{i,corr} = Z_{i,meas} - 2\pi f L_s \quad \textbf{(33)}$$

where $Z_{i,meas}$ is the imaginary part of the measured impedance. All impedance measurements in this work has been made using measurement cells where the inductance was known, and this correction has been routinely performed before analysis of the data.

The possibility to separate grain boundary and bulk conductivity in impedance spectra can be used for estimating the specific grain boundary conductivity, σ_{gb}^{sp} [142-144]. This quantity can be calculated from the non-specific grain boundary conductivity (that is, grain boundary conductivity normalised to the geometry of the entire sample), $\sigma_{gb,}$ the size of the grains, d_g, and the thickness of the grain boundaries, δ_{gb}.

$$\sigma_{gb}^{sp} = \sigma_{gb} \frac{\delta_{gb}}{d_g} \quad \textbf{(34)}$$

The grain size can be estimated from electron microscopy, or, for materials with nano-sized grains, X-ray diffraction [145]. The thickness of the grain boundaries can be estimated from the (quasi equivalent) grain boundary capacitance:

$$C_{gb} = \varepsilon_0 \varepsilon_{gb} \frac{d_g}{\delta_{gb}} \quad \textbf{(35)}$$

where ε_0 and ε_{gb} are the permittivity of free space and of the grain boundary respectively. In order to perform the calculations, a value must be assumed for the relative permittivity of the grain boundaries. As a starting point, the value for bulk can be assumed.

In this work, this method was utilised in the conductivity measurements on calcium doped samarium titanate, showing that the conductivity in the grain boundaries was around two orders of magnitude lower than the total conductivity.

Ideally, electrodes are made to cover the entire surface of a pellet, thus avoiding fringing effects. However, this is not always possible due to for example geometric restrictions of the experimental setup. To enable corrections for the error made by using electrodes that do not properly distribute the current over the entire surface of the pellet, a finite element model was set up using Comsol Multiphysics. The model consists of a cylindrical pellet

with height h, diameter d_0 and equipped with concentric, circular electrodes with diameter d_1. The pellet was divided in a mesh of approximately 5000 elements. The voltage at the two electrodes was set to 0 and 1 V respectively, and the total current density found by integrating over one electrode surface, allowing for a resistance to be calculated in the same way it would be done in a real measurement. The calculated resistance could then be compared to the "correct" assigned resistance, giving a correction factor. This calculation was carried out for a number of h/d_0 and d_1/d_0 ratios, finding both the error made by assuming linear current through the entire pellet and through the cylinder defined by the electrodes. Figure 9 shows the ratio between modelled and true conductivities for the former case for varying pellet heights and electrode diameters for a pellet with a diameter of 1 cm.

These corrections were applied to the conductivity measurements on calcium doped $Sm_2Ti_2O_7$. For the impedance measurements made in connection with concentration cell measurements, the required data was ratios between electrode and sample resistances, not total conductivities, and therefore these corrections were not applied despite the non-complete electrode coverage.

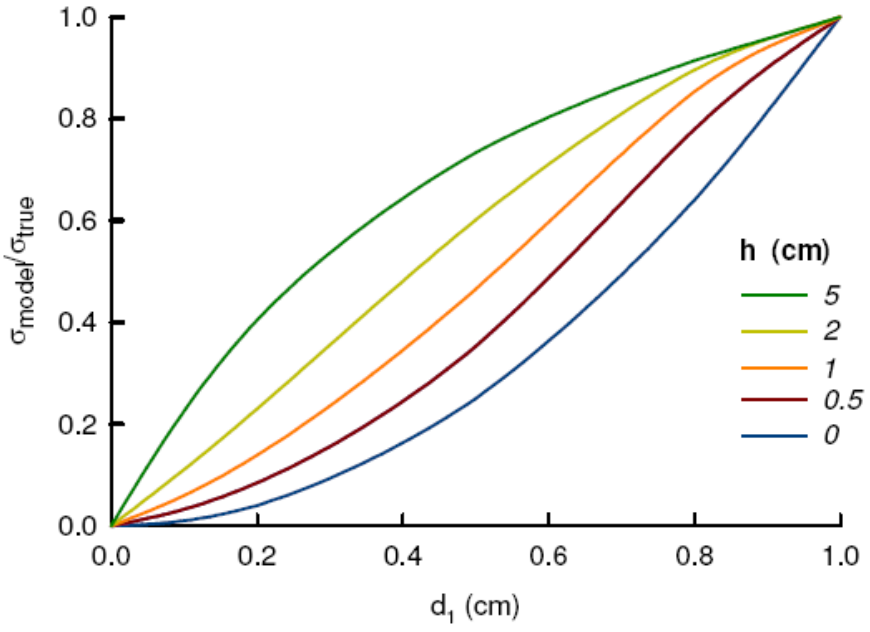

Figure 9 Correction factors for non-complete electrode coverage for a pellet with d_0 = 1 cm

Another factor that affects the conductivity measured is the porosity of the sample. The denser the sample, the higher the conductivity it will have. If the porosity can be assumed to be spherical and well dispersed in the sample, a value that depends only on the material, can be found by using the relation [146]

$$\frac{\sigma_\rho}{\sigma_1} = \rho_r^{\frac{3}{2}} \qquad \textbf{(36)}$$

where σ_ρ is the conductivity at a given relative density, ρ_r, and σ_1 is the conductivity for a fully dense sample ($\rho_r = 1$).

2.1. Yttrium doped strontium cerate (SCY)

Acceptor doped strontium cerate is, as seen above, a well known proton conductor. The structural and electrical properties of yttrium doped strontium cerate (SCY) have previously been investigated in the division [18, 72]. The material is an orthorhombic perovskite (space group *Pnma*) [72], and was shown to be primarily a protonic conductor in the temperature range 600 – 800 °C. At high and low p_{O_2}, p- and n-type electronic conductivity is seen, making it potentially interesting for hydrogen membrane applications. As a material with well known properties, $SrCe_{0.95}Y_{0.05}O_{3-\delta}$ was chosen as a starting point for experiments in this work. The powder for sample preparation was synthesised using a solid state technique as described elsewhere [19]. Since the powder had been stored for a significant period of time, it was dried overnight at 800 °C to remove any water. The powder was examined using x-ray diffraction, and no secondary phases were found. For preparation of samples, the powder was milled in ethanol using zirconia balls for 8-12 hours. The suspension was then sieved through a mesh 40 nylon cloth and dried. The fine fraction was used for sample preparation while the coarse fraction was used as sacrificial powder for sintering. After drying, the powder was ground

and pressed uniaxially using stainless steel dies at approximately 60 MPa. Stearic acid in ethanol was used as a lubricant. If necessary to make the pellets, approximately 0.5 ml pr. 10 gram of powder of a 2 % (w/w) aqueous polyvinyl alcohol solution was added as a binder. After uniaxial pressing, the pellets were transferred to latex containers, which were evacuated for isostatic pressing at 325 MPa.

Pellets were sintered in air in alumina crucibles resting on a layer of the coarser SCY powder to prevent reaction with the crucible. The sintering temperature, 1450 °C, was held for 12 hours, with heating and cooling rates of 100 °C/h.

The total and open porosity of the samples was estimated by carefully measuring and weighing the samples to find the total porosity, then submerging it in water and weighing it again to find what percentage of the porosity is open. In general, densities were found to be at least 92 % of theoretical with no measurable open porosity. The highest density (95 % of theoretical) pellet was used for concentration cell and flux measurements (see below). A second pellet was cut into a bar for DC conductivity measurements, using the left over pieces for scanning electron microscopy (SEM) investigations. SEM supported the assumption that the sample had no open porosity, indicated that the sample was more porous towards the surface than in the centre, and showed no indications of secondary phases in backscatter mode.

Conductivity measurements were performed as outlined above. Since the material had been investigated previously, a complete study over a large range of temperatures and oxygen and water partial pressures was not attempted. Rather, the intention was to verify previous results with new samples. A set of conductivity versus p_{O_2} measurements was made at 600 °C using mixtures of air and nitrogen at high p_{O_2} and mixtures of nitrogen and dilute (6 % in nitrogen) for low p_{O_2}. For all measurements, the gases were moisturised by bubbling the gas through a water bottle refrigerated at 12 °C, giving a water content of approximately 1 %.

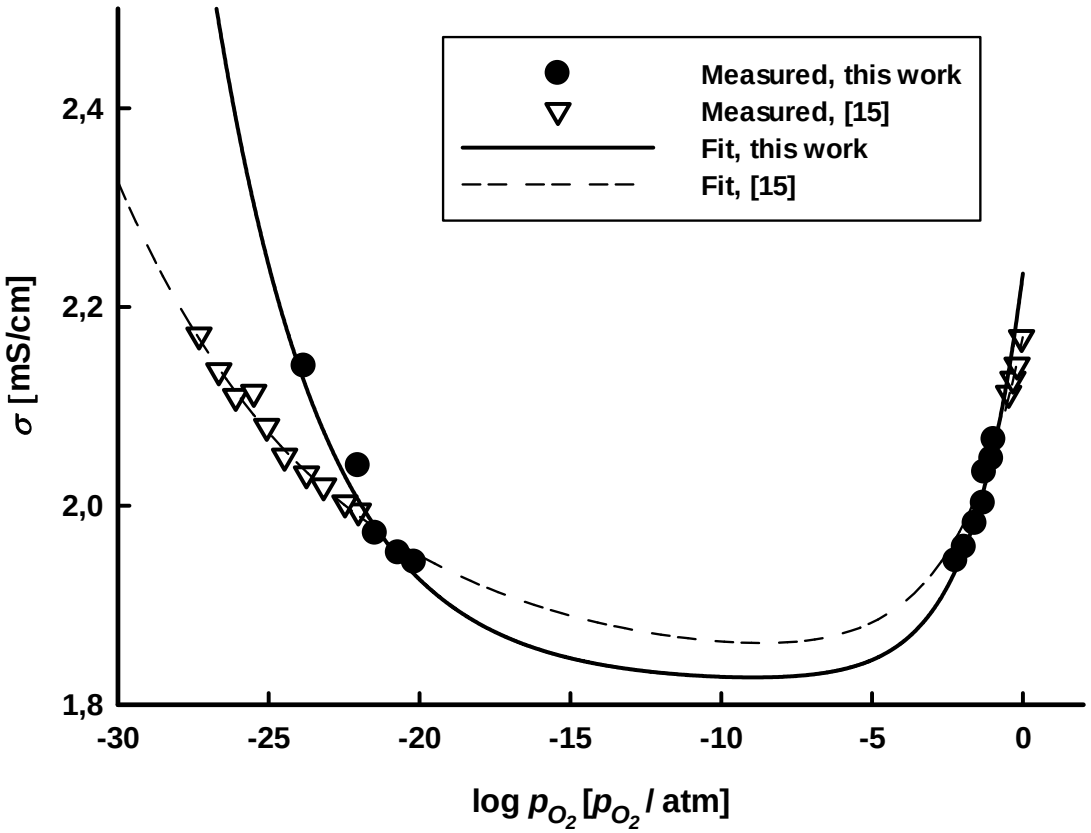

Figure 10 Measurements of conductivity vs. p_{O_2} in 1% H_2O at 600 °C. Curves are fitted to the equation $\sigma_{tot} = \sigma_{ion} + \sigma_p^0 p_{O2}^p + \sigma_n^0 p_{O2}^n$

The data collected in this work was corrected for sample porosity as described in chapter 2. This was not the case for the data from [19], but those measurements were made on a very dense sample, meaning the influence of porosity should be small.

The conductivity is increasing with increasing p_{O_2} at high oxygen partial pressures, and the opposite is observed at low p_{O_2}. The data was fitted to the equation

$$\sigma_{tot} = \sigma_{ion} + \sigma_p^0 p_{O_2}^p + \sigma_n^0 p_{O_2}^n \quad (37)$$

Here, σ_{tot} is the total conductivity, σ_{ion} the ionic conductivity, σ_p^0 and σ_n^0 p- and n-type electronic conductivity at p_{O_2} = 1 atm respectively, while p and n are the exponents

giving the p_{O_2}-dependency of the p- and n-type conductivity. Due to the high doping level, dopants and either oxygen vacancies or protons (in this case protons) are expected to dominate the defect concentrations, and *p* and *n* are therefore expected to be equal to ¼ and -¼ respectively. In earlier work [19], the conductivity was fitted with the exponents fixed to these values. This approach was also used here. Finally, the early data [19] was fitted again allowing *p* and *n* to vary. The results of these fits are summarised in Table 2.

Table 2 Fitted parameters for the conductivity of $SrCe_{0.95}Y_{0.05}O_{3-\delta}$ at 600 °C in 1 % H_2O, conductivities in S/cm.

Parameter	σ_{ion}	σ_p^0	σ_n^0	p	n
This work	1.83×10^{-3}	4.13×10^{-4}	4.22×10^{-7}	0.25	0.12
This work, *n* and *p* fixed	1.9×10^{-3}	2.23×10^{-4}	2.7×10^{-10}	¼	-¼
From [19]	1.8×10^{-3}	3.33×10^{-4}	6.7×10^{-6}	0.19	0.062
From [19] , *n* and *p* fixed (from [19])	1.7×10^{-3}	2.1×10^{-4}	5.3×10^{-11}	¼	-¼

Naturally, the values of all parameters in the fit are interdependent; a small value for *n* will give a high σ_n^0. The four different fits show good agreement on the values of the ionic conductivity and σ_p^0. The new fit to the data [19] gives a slightly lower value for *p*, but it seems reasonable to assume that the increase in conductivity at high p_{O_2} is due to p-type conductivity. There is, however, significant disagreement on especially the p_{O_2}-dependency of n-type conductivity. Looking at Figure 10 it is unsurprising; it is clear that the new measurements show higher conductivity at low p_{O_2}, and that the lower the p_{O_2}, the larger the discrepancy. As seen in the chapter 2, the slope is expected to take one of two values:

a) -¼, in the case of protons and dopants dominating the charge neutrality but electrons being more mobile and therefore dominating the conductivity, as seen in equation (11).

b) -1/6, which is close to what was found fitting to the data in this work, if electrons take over as the species charge compensating the majority ionic defect, given by equation (13).

With a dopant concentration of 5%, (b) would imply a very high electron concentration, and a level of reduction that seems unlikely for this material at 600 °C. These deviations from the expected behaviour were also noted previously [19].

One possible explanation is that the measurements were not performed at equilibrium. Significant (up to 60 hours) equilibration time was allowed for in these measurements. A weak trend of decreasing resistance was seen over time. After the measurement series was concluded, the measurement was left running for over 600 hours at the most reducing conditions. Again, an increase of the conductivity was seen. If the conductivity value reached at the end of this time period is used for a fit, the value of n is found to be -0.35. This is an indication that the true value of n is indeed -0.25, and that the smaller values found here are due to the reduction process being very slow and insufficient equilibration time being given.

2.2. Lanthanum magnesium titanate

An effort was made to find new potential proton conducting materials, preferably less susceptible to reaction with CO_2 than the alkaline earth based perovskites and having significant electronic conductivity to allow for hydrogen permeability. It was decided to explore the area of mixed perovskites further, with the intention of using off-stoichiometry with a surplus of the lower valent B-site ion as the method for achieving acceptor doping. To avoid alkaline earth metals while still retaining a large and relatively electronegative ion, lanthanum was chosen for the A-site. For the B-site range of possible I-V (roman numbers indicating the two ions valence) and II-IV pairs for perovskites with the general formula $La_2B'B''O_6$, II-V pairs giving the formula $La_3B'_2B''O_9$, I-IV pairs giving $La_2B'_2B''O_6$ materials and even II-VI pairs for $La_4B'_3B''O_{12}$ compounds were investigated. Shannon radii [147] were used to determine whether a perovskite could be

formed according to the rules outlined in chapter 1.2.2. The average Pauling electronegativity [148] was sought minimised to increase proton uptake. Furthermore, the aim was to include at least one element known to exhibit a number of different oxidation states to increase the likelihood of the final compound having electronic conductivity.

The most interesting composition found in this survey was $La_2Mg_{1+x}Ti_{1-x}O_{6-\delta}$ (LMT). Since the original survey was made, the composition has been mentioned in one US patent application as being a proton conductor [149], though the application gives no data on conductivity or similar. It has also been the focus of a master thesis [150], where the main rationale for investigating it was the similarity to known proton conductor $LaScO_3$ [151-153], and the great reduction in material cost if magnesium and titanium could be substituted for scandium while retaining the proton conductivity. In other fields, LMT has attracted attention primarily for its dielectric properties, which gives the material useful properties for microwave resonators and filters [154-159]. The structure has been studied in depth in relation to those studies. An early investigation indicated a cubic perovskite structure [154]. More recent studies using more refined methods indicated lower symmetry structures; Rieteld refinement of XRD data indicated orthorhombic *Pbnm* symmetry [155], later high-resolution neutron powder diffraction revealed the room temperature structure to be even lower symmetry monoclinic $P2_1/n$, and that the material undergoes a transition to rhombohedral *R3* at 1036 °C [159]. This study also showed significant Mg/Ti-ordering.

In this work, powders and solid samples were prepared using the same solid state method described in chapter 2.1 from La_2O_3, MgO and TiO_2, all >99.9% pure from Sigma Aldrich. Four compositions were made; $La_2Mg_{1+x}Ti_{1-x}O_6$ with x = 0, 0.05, 0.10 and 0.15. XRD indicated that phase pure powders were achieved after two calcinations at 1350 °C for 12 hours of the first two compositions, while phase purity was not achieved for the two compositions with greater off-stoichiometry, even after several more calcination steps at temperatures up to 1450 °C, indication that the tolerance level for off-stoichiometry for the system is somewhere in the range $0.05 < x < 0.10$.

Samples were sintered in both air and in moist (appr. 3 % water vapour) 9 % hydrogen in nitrogen. In both cases, small amounts of secondary phases were found when sintering at 1450 °C, and the concentration of these phases, which could not immediately be

identified using XRD, increased as the sintering temperature was increased to 1500 °C. This finding agrees poorly with the sintering temperatures of up to 1600 °C used in the cited literature, and the reason for it is not currently known. Decreasing the sintering temperature to 1430 °C yielded phase pure samples from the phase pure powders.

Four sintered samples are shown in Figure 11. A marked colour difference is found between pellets sintered in hydrogen and those sintered in air, which is an indication that the material has been reduced at high temperature and that this reduced state is frozen in at room temperature.

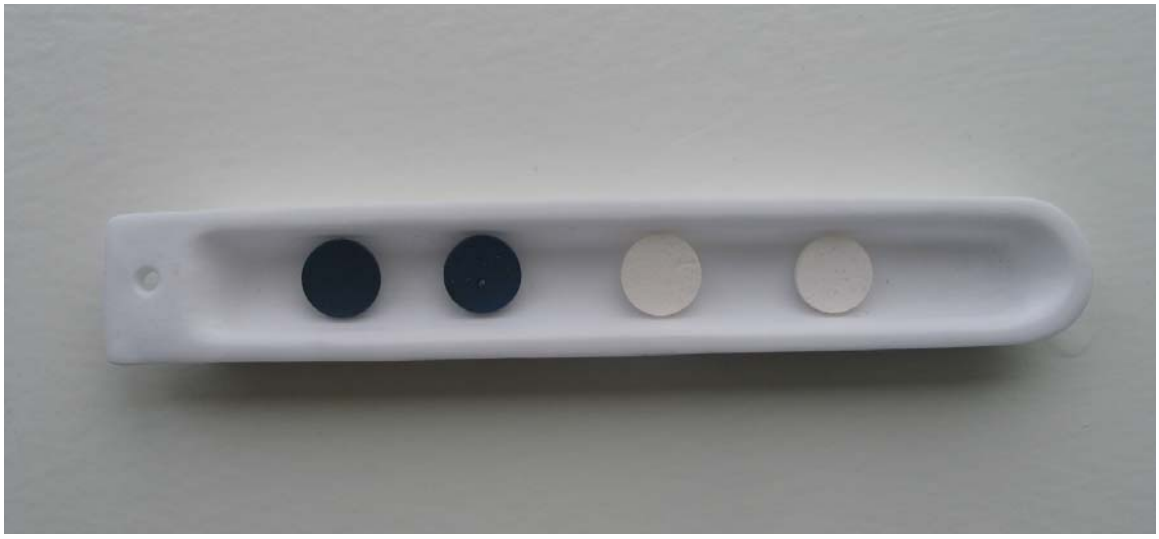

Figure 11 LMT pellets sintered in dilute hydrogen (left) and in air (right)

In this work, only some preliminary conductivity measurements were made, to verify that the samples sintered in hydrogen were in a reduced state and electronically conducting. Measurements were only conducted on the phase pure compositions La_2MgTiO_6 and $La_2Mg_{1.05}Ti_{0.95}O_{6-\delta}$. Samples were painted with a Pt-paste and baked at 1000 °C for 4 hours, again keeping the reduced samples in dilute moist hydrogen and the others in air. Measurements were performed in synthetic air and dilute (6 %) hydrogen using both dry and wet gases at 600 and 800 °C. For the regular samples, the measurements in synthetic air were conducted first, while the measurements in hydrogen were done first for reduced samples. Measurements were made in the frequency range 0.096 – 96000 Hz. Due to the large difference in conductivity, different applied voltage signals had to be used; 0.1 V

was sufficient to achieve good spectra for the reduced samples while 3 V had to be used for the oxidized ones. Upon introducing the non-reduced samples to reducing gas, clear induction loops were seen in the impedance spectra, indicating chemical reaction. A steady conductivity value was only reached after several days of equilibration.

The impedance spectra were all corrected for cell inductance. The data from reduced pellets consisted of two arcs. The quasi equivalent capacitance of the high frequency arc was in the 10^{-9} F cm^{-2} range, indicating that it was due to grain boundary resistance. Therefore, the data was fitted using a R(RQ)(RQ) model, which gave good fits for all measurements. The grain boundary arc could not be properly resolved in the fitting procedure for spectra obtained on oxidised samples. The data was therefore fitted using one (RQ) subcircuit to describe the overall conductivity and one (RQ) (at 800 °C) or Q (at 600 °C) to describe electrode processes. This gave somewhat lower quality fits and likely underestimated total sample resistance slightly.

The conductivity values obtained are summarized in Table 3, below.

Table 3 Conductivity values for LMT in S/cm. Reduced samples were used for measurements in dilute hydrogen,

		600 °C		800 °C	
		Dry	Wet	Dry	Wet
La_2MgTiO_6	Synth. air	6.8×10^{-9}	1.7×10^{-8}	3.6×10^{-7}	4.4×10^{-7}
	6 % Hydrogen	0.029	0.035	0.197	0.196
$La_2Mg_{1.05}Ti_{0.95}O_6$	Synth. air	8.7×10^{-9}	2.3×10^{-8}	4.0×10^{-7}	4.1×10^{-7}
	6 % Hydrogen	0.187	0.145	-	0.196

The most striking feature in these data is the very large difference in conductivity between reduced and regular samples; between 5 and 7 orders of magnitude. The conductivity is higher in wet atmosphere for the non-reduced samples, and this effect is more pronounced at the lower temperature.

A small p_{O_2} range sweep was performed at 800 °C on the off-stoichiometric reduced sample to confirm the nature of the conductivity, as shown in Figure 12.

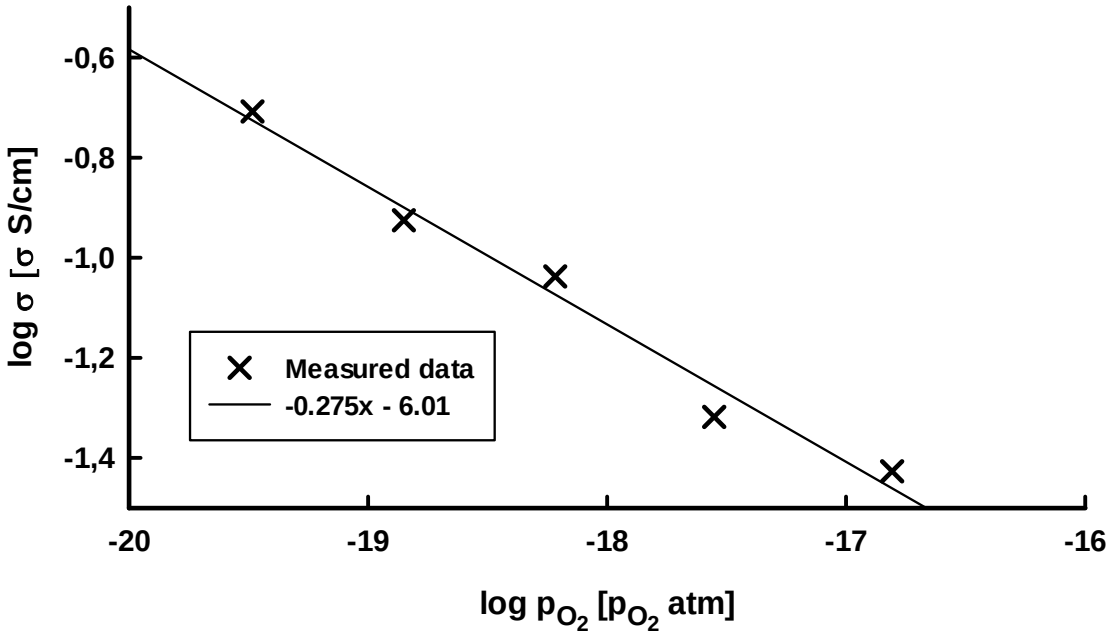

Figure 12 Conductivity data for $La_2Mg_{1.05}Ti_{0.95}O_{3-\delta}$ in moist dilute hydrogen at 800 °C

Since the slope of the fit is close to -¼, it seems safe to assume that the conductivity is primarily electronic, with the defect chemistry dominated by oxygen vacancies and "dopants" (Mg on Ti-sites).

Three out of four samples were cracked after measurements in the opposite atmosphere from which they were sintered. This could indicate that the reduction is accompanied by chemical expansion. This should be examined further.

Conductivity measurements on slightly less off-stoichiometric LMT have been performed previously [150], see Figure 13. These measurements generally showed much higher conductivity values in air, but lower in reducing atmospheres. It also indicated protonic conductivity in reducing atmospheres up to approximately 600 °C.

Some conductivity on a compound labelled $MgLa_2TiO_6$, but with the X-ray data being presented matching that of LMT, has been given in a study of phase equilibria in the MgO-La_2O_3-TiO_2 system [160]. The data, presumably recorded in air, although it is not directly specified, is in the same low range as for the non-reduced samples in this work.

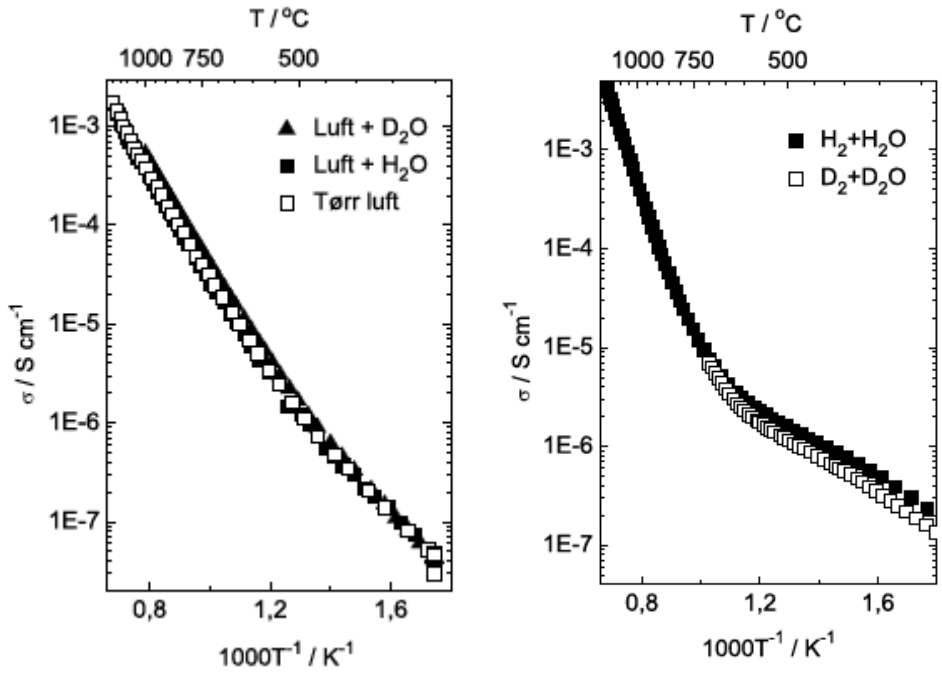

Figure 13 Conductivity of $La_2Mg_{1.04}Ti_{0.96}O_6$ as a function of inverse temperature in dry and wet (H_2O and D_2O) air, left and wet hydrogen and deuterium, right. Data is from two different measurement series. [150]

Much further work is still required on this compound, including a fuller study on the conductivity, especially of reduced samples. Thermogravimetric analysis is currently being conducted to both determine to which extent the material is reduced and whether it takes up water to a significant degree when reduced. If this is the case, hydrogen flux measurements should also be performed on dense samples. The available data on LMT is inconclusive, and somewhat self-contradicting. It does, however, appear that the material can exhibit moderate levels of proton conductivity and can also be reduced to give electronic conductivity, making it an interesting candidate for further studies for hydrogen membranes.

2.3. Nickel in SCY

Small amounts of transition metals are frequently added to doped $BaZrO_3$ to enhance the sinterability [161-163]. In a recent study, the same approach was used introducing transition metals in $BaCeO_3$ [164-165]. Studies of nickel-$SrCeO_3$ cermets for hydrogen permeable membrane applications have also been made [166-167]

In this work, the effect of attempting to use Ni as a dopant in $SrCe_{0.85}Y_{0.15}O_{3-\delta}$ on the conductivity of the material has been studied, with hopes of finding increased electronic conductivity while maintaining the protonic conductivity. VI coordinated Ni has an ionic radius of only 0.69 Å in the divalent and 0.60 Å in the trivalent state [147]. As such, it is too small to fulfil the Goldschmidt tolerance factor in equation (1) in a perovskite structure with strontium on the A-site. Thus, it was uncertain whether it would be possible to include significant amounts of Ni in the perovskite structure itself, even as a minor dopant.

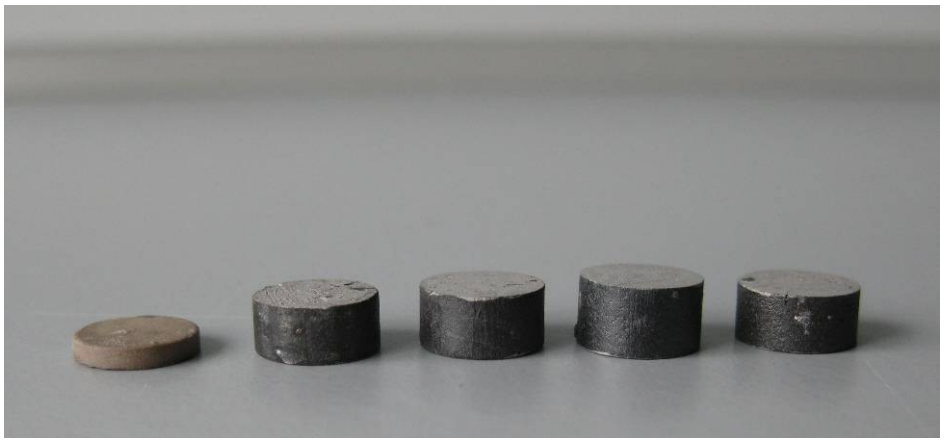

Figure 14 NiSCY pellets, with 0, 0.5, 1, 2 and 4 % Ni

Five compositions with general formula $SrCe_{0.85-x}Y_{0.15}Ni_xO_{3-\delta}$ were synthesised, with x = 0, 0.005, 0.01, 0.02 and 0.04. The powders were made using the same solid state synthesis method described in the previous chapter, with $SrCO_3$, CeO_2, Y_2O_3 and NiO as starting materials, all at least 99 % pure. The powders were ground and calcined at 1250 °C for 12 hours twice. After this, two batches of pellets were made; a set of smaller

pellets with a green diameter of 10 mm for AC conductivity measurements, and a set of larger pellets with green diameter of 18 mm for flux measurements. For the second batch, the composition without nickel was omitted.

Both sets of pellets were pressed as described in the previous chapter and sintered at 1450 °C for 12 hours in air, although in separate furnaces. AC conductivity samples equipped with Pt-paste electrodes are shown in Figure 14.

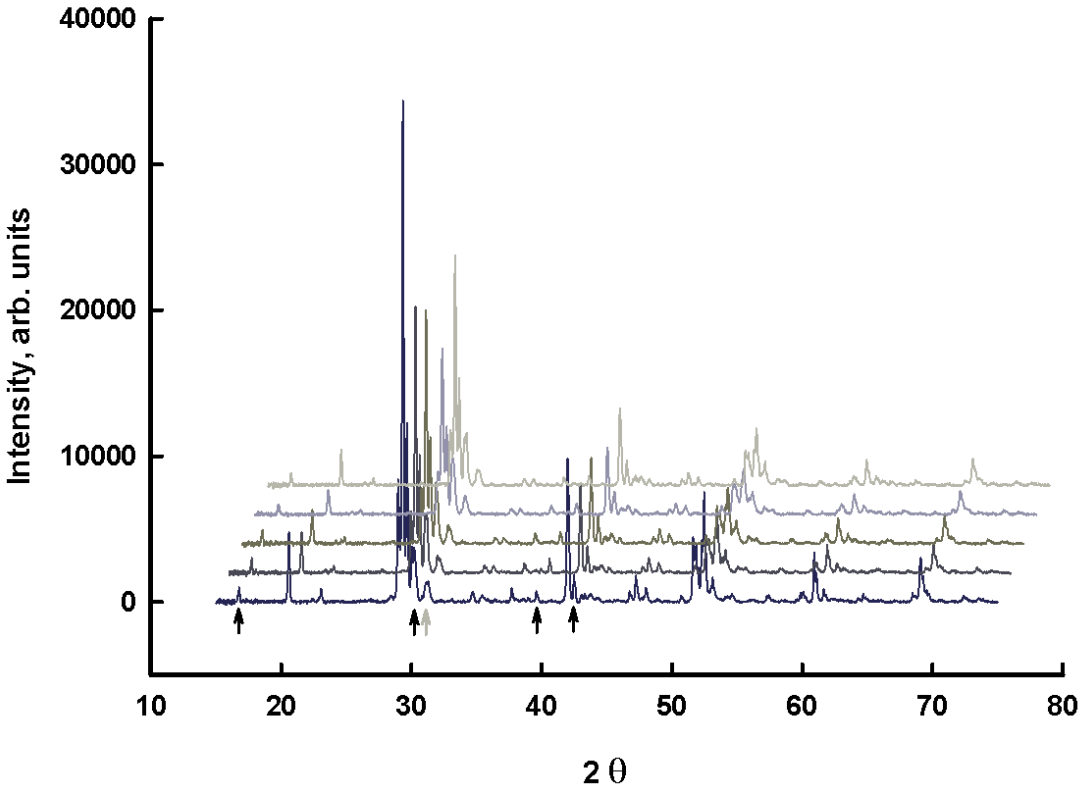

Figure 15 X-ray diffractograms of NiSCY AC conductivity pellets, with increasing Ni content from bottom to top. Diffractograms shifted in intensity and 2θ for clarity. Black arrows indicate main Sr_2CeO_4 peaks, light grey arrow indicates unknown impurity peak.

X-ray diffractograms of the smaller pellets are shown in Figure 15, while diffractograms of the larger pellets are shown in Figure 16 and Figure 17. Despite using powders from the same batch and formally identical sintering conditions, it appears that there is a significant difference in the phase composition of the two sets of samples. The smaller samples consisted of mainly perovskite phase, with a small amount of a K_2NiF_4 type phase with composition Sr_2CeO_4. As mentioned in chapter 1.2.2, this type of impurity is

often formed in A-site superstoichiometric perovskites, and could be an indication that the nickel did not enter the structure in any appreciable amount, although the amount of Sr_2CeO_4 appeared constant with nickel content. Another possibility is that the 15 % yttrium was not completely dissolved in the structure, and that the nickel was present in grain boundaries in amounts too small to be visible in XRD. In contrast to the uniform smaller pellets, the larger pellets intended for flux measurements had a grainy crystalline appearance, indicating that a secondary phase was present in significant amounts on the surface. This was confirmed by XRD, shown in Figure 16 of pellets as sintered and Figure 17 after grinding away the surface layer. As seen in Figure 16, the surface layer contained mainly the perovskite phase, but the diffractograms also revealed a secondary phase having two strong reflections at $2\theta = 32$ and 33.5°, increasing greatly in intensity with increasing nickel content. This secondary phase was identified as a member of the oxygen deficient K_2NiF_4 type structure $Ln_{2-x}Sr_xNiO_{4-\delta}$, with Ln being either Ce or Y, with the specific formulae $Y_{0.33}Sr_{1.67}NiO_{3.67}$ (or $YSr_5Ni_3O_{11}$) and $Ce_{0.25}Sr_{1.75}NiO_{3.75}$ (or $CeSr_7Ni_4O_{15}$) respectively, the structures of which are well described in literature [168-170].

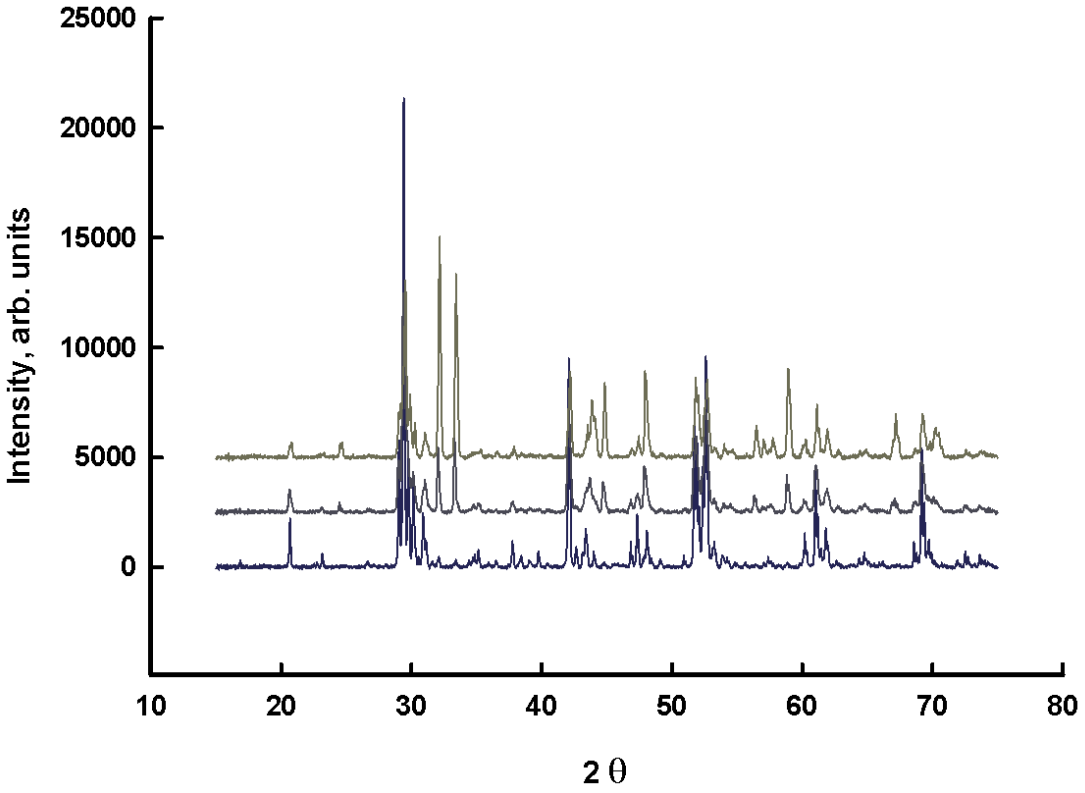

Figure 16 X-ray diffractograms of NiSCY flux pellets with 1, 2 and 4 % nickel, increasing nickel content from bottom to top, before grinding. Diffractograms shifted vertically for clarity.

With the resolution of the diffractograms, it was not possible to determine which of the two phases was present, or indeed, if it was a mixture of the two. Samples were investigated with SEM. Backscatter mode revealed two distinct compositions as shown in Figure 18. EDX (energy dispersive X-ray spectroscopy) revealed the darker areas to be Y-rich, substantiating the idea that the secondary phase is $Y_{0.33}Sr_{1.67}NiO_{3.67}$.

The samples where the surface had been ground off contained significantly smaller amounts of this phase, but still enough to be detectable with XRD.

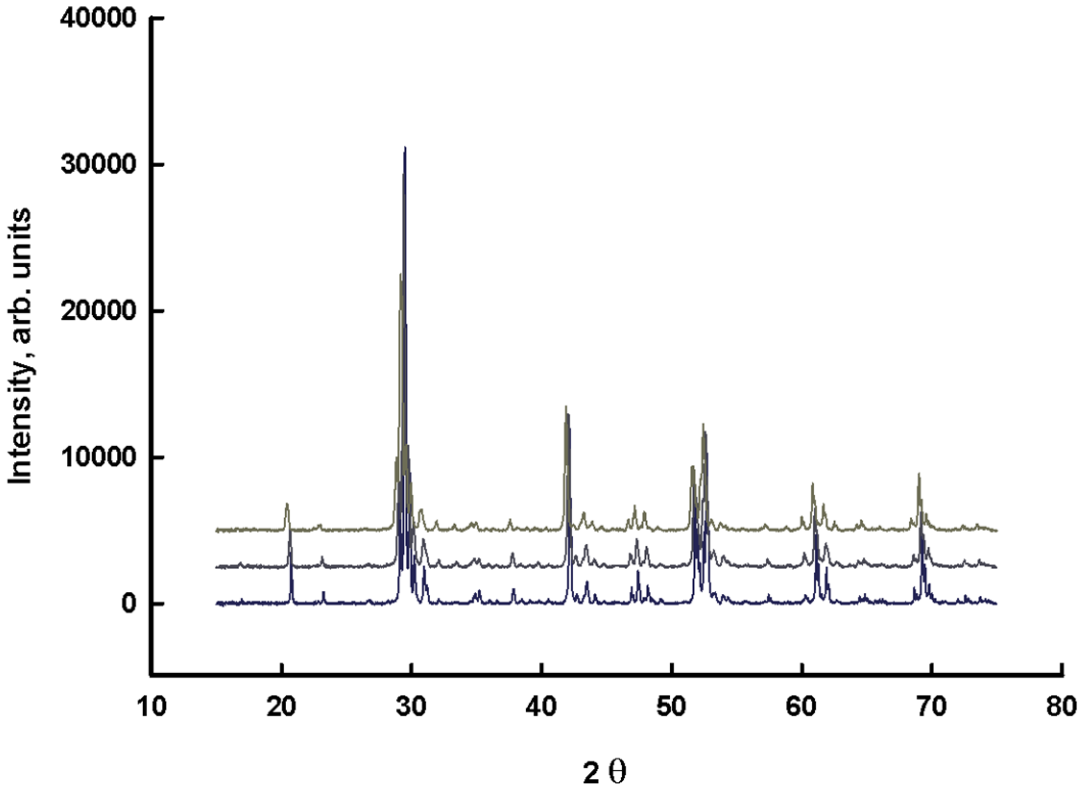

Figure 17 X-ray diffractograms of NiSCY flux pellets with 1, 2 and 4 % nickel, increasing nickel content from bottom to top, after grinding. Diffractograms shifted vertically for clarity.

The high temperature conductivity behaviour of these specific K_2NiF_4 type materials is not well known. At lower temperatures, the Y-containing compound is reported to be semiconducting, while the Ce-containing compound is a metallic conductor [169]. In general, $Ln_{2-x}Sr_xNiO_{4-\delta}$ type materials with $x \geq 1$ have been reported to behave as metallic conductors [171].

It should be noted that, if the phase has significant electronic conductivity, its presence in the samples is not detrimental to their usefulness as hydrogen membrane materials, but could positively contribute to the flux. It is, however, likely that such a two-phase system could have stability problems in large p_{O_2}-gradients.

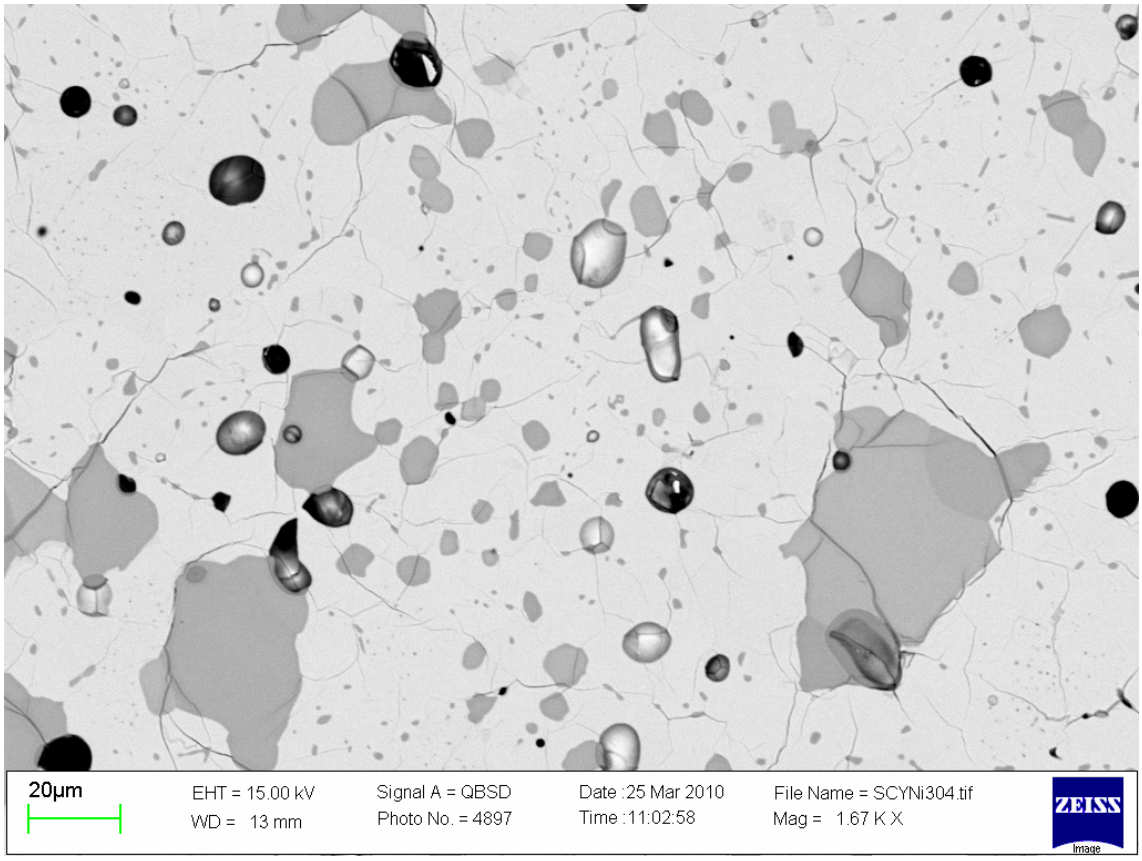

Figure 18 Backscatter mode SEM image of 1 % Ni doped NiSCY sample. Darker areas are Y-rich as indicated by EDX.

A series of AC measurements were made on the nickel doped SCY samples. Measurements of conductivity as a function of p_{O_2} were performed using wet and dry mixtures of dilute hydrogen or oxygen with nitrogen at 600 °C. The results of measurements on samples with 0.5 and 4 % nickel, representative for the entire measurement series, are shown in Figure 19. Conductivity as a function of temperature was measured in wet and dry synthetic air on samples with 1, 2 and 4 % Ni. The results of these measurements are shown in Figure 20. After the measurements were concluded it was found that a small portion of the platinum paste electrode had delaminated from the sample with 2 % nickel, which explains the lower conductivities found in this sample.

Conductivity vs. p_{O_2} data was fitted to equation (37) using three different strategies; fixing both n and p to ±0.25, allowing both to take on any value, and restricting them so that $p = -n$. As seen in Figure 19, conductivity was nearly constant with p_{O_2} in oxidising

wet conditions. Therefore, fits where both parameters were allowed to take any value did not give results that physically made sense, and those where p was restricted to $-n$ did not converge in all cases. For the fits that did converge, the value for p was between 0.13 and 0.51, indicating that $p = -n = 0.25$ was likely a correct model to use. The results of fits to $\sigma_{tot} = \sigma_{ion} + \sigma_p{}^0 p_{O_2}{}^{0.25} + \sigma_n{}^0 p_{O_2}{}^{-0.25}$ are summarised in Table 4 along with the parameters for $SrCe_{0.95}Y_{0.05}O_{3-\delta}$ for comparison.

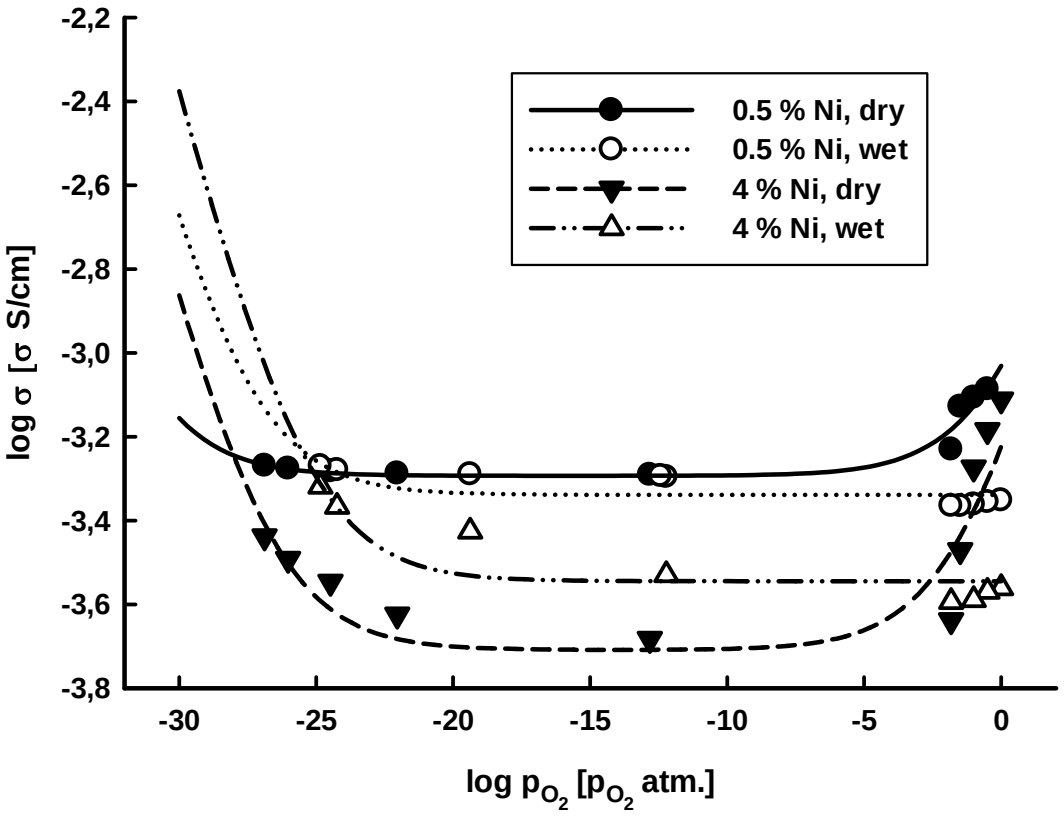

Figure 19 Conductivity vs. oxygen partial pressure for NiSCY samples with 0.5 and 4 % nickel and fits to $\sigma_{tot} = \sigma_{ion} + \sigma_p{}^0 p_{O_2}{}^{0.25} + \sigma_n{}^0 p_{O_2}{}^{-0.25}$ Data for samples with 1 and 2 % Ni omitted for clarity.

Table 4 Conductivity parameters in S/cm for nickel doped SCY at 600 °C. Wet measurements used 1 % water vapour.

	σ_{ion}	σ_p^0	σ_n^0
0.5 % Ni, dry	5.09×10^{-4}	4.22×10^{-4}	6.02×10^{-12}
0.5 % Ni, wet	4.58×10^{-4}	6.90×10^{-13}	5.29×10^{-11}
1 % Ni, dry	2.97×10^{-4}	2.53×10^{-4}	5.57×10^{-11}
1 % Ni, wet	3.39×10^{-4}	2.42×10^{-13}	1.67×10^{-10}
2 % Ni, dry	1.68×10^{-4}	1.43×10^{-4}	3.63×10^{-11}
2 % Ni, wet	1.57×10^{-4}	2.56×10^{-13}	1.34×10^{-10}
4 % Ni, dry	1.95×10^{-4}	4.00×10^{-4}	3.72×10^{-11}
4 % Ni, wet	2.85×10^{-4}	4.99×10^{-13}	1.24×10^{-10}
$SrCe_{0.95}Y_{0.95}O_{3-\delta}$	1.9×10^{-3}	2.23×10^{-4}	2.7×10^{-10}

From this data, it appears that introducing nickel in SCY negatively affects the ionic conductivity, although most of the protonic conductivity is retained as indicated by the higher ionic conductivity in wet atmospheres. An increase in the p-type electronic conductivity can also be seen in dry conditions, but it is suppressed in wet conditions.

This same trend is observed at high temperature in the conductivity versus inverse temperature plots. At lower temperatures, the conductivity is higher in wet atmospheres than in dry, and there appears to be a tendency for the temperature at which p-type conductivity becomes dominant to increase with temperature.

The activation energy for the total conductivity is approximately 0.61 eV for all measurements, which is in good accordance with values reported in literature on similar materials.

Results of flux measurements are given in chapter 5.

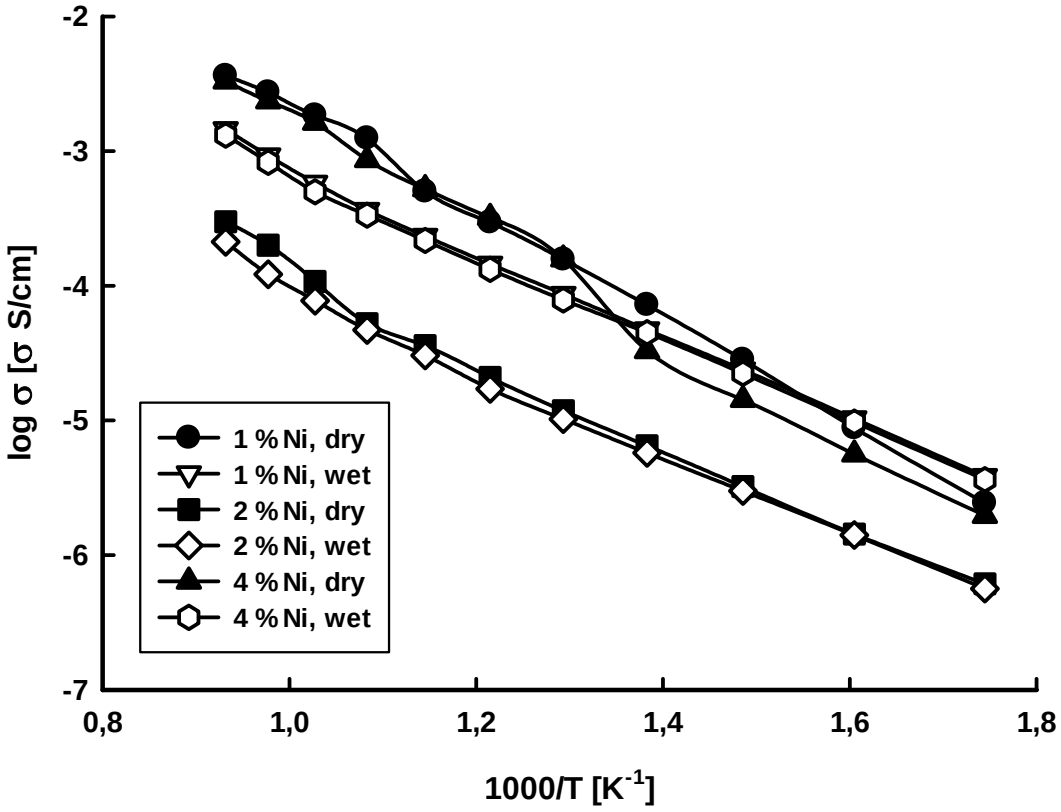

Figure 20 Arrhenius type plots for NiSCY samples in wet (1 % water vapour) and dry synthetic air.

3. The Concentration Cell Method

The concentration cell or electromotive force (EMF) method is useful for finding the transport number of different charge carriers in mixed conductors, and is therefore an interesting technique for characterisation of potential membrane materials. In this work, it has been applied to two different systems; SCY and $Sm_{1.92}Ca_{0.08}Ti_2O_7$. The former was an attempt to explore the method and evaluate the setup, as well as investigate methods for correcting for electrode polarisation resistances. The latter was investigated in collaboration with University of Gothenburg, as a part of a larger study on proton conductivity in pyrochlores. The material is published in paper I and II (appended at the end of this thesis) respectively, and methods and results are discussed in depth there. Therefore, only a summary is given here, along with some general remarks.

Let us begin with the case where only electronic conductivity and that of a single ionic species is relevant in the material investigated. In this case, the voltage measured over a sample equipped with reversible electrodes and subjected to a gradient in chemical potential will be

$$E_{EMF} = -\frac{RT}{nF} t_i \ln \frac{p_2}{p_1} \qquad \textbf{(38)}$$

as long as small enough gradients are used that an average transport number can be assumed.

The theoretical voltage calculated using the Nernst equation is

$$E_{Nernst} = -\frac{RT}{nF} \ln \frac{p_2}{p_1} \qquad \textbf{(39)}$$

Thus, the average transport number can be calculated as

$$t_i = \frac{E_{EMF}}{E_{Nernst}} \quad \textbf{(40)}$$

If the electrodes are not fully reversible, this causes an underestimation of the transport number. Corrections for electrode polarisation resistance, R_η, in measurements on mixed oxide ionic-electronic conductors are well described in literature [172-175]. Two methods of correction are used; one based entirely on impedance spectroscopy [173], hereafter called the impedance analysis method, and one based on a high frequency AC conductivity measurement coupled with a measurement of the voltage as a function of the resistance of a variable resistor connected in parallel to the sample [172], hereafter called the active load method.

The impedance analysis method depends on finding two resistances, R_S, that is only due to the sample itself and R_T, which is the total resistance including electrodes. These are usually found as high and low frequency real axis intercepts in a Nyquist plot respectively. The corrected calculation of the average transport number can be calculated as

$$t_i = 1 - \frac{R_S}{R_T}\left(1 - \frac{E_{measured}}{E_{Nernst}}\right) \quad \textbf{(41)}$$

If the electrode polarisation resistance is negligible, R_S will be equal to R_T, and the equation simplifies to the previous equation.

For the active load measurement, a variable resistor with resistance R_b of roughly the same magnitude as the sample resistance is introduced in parallel to the sample, as shown in Figure 21. This effectively increases the electronic conductivity of the sample by $1/R_b$, which gives the following relation between measured and theoretical voltages:

$$\frac{E_{Nernst}}{E_{measured}} - 1 = (R_i + R_\eta)\left(\frac{1}{R_e} + \frac{1}{R_b}\right) \quad \textbf{(42)}$$

Varying R_b and measuring the change in $E_{measured}$ and plotting $E_{Nernst}/E_{measured}$ -1 as a function of $1/R_b$ yields a straight line with slope (R_i + R_η) intersecting the x-axis at $-1/R_e$. A high frequency conductivity measurement of the sample then allows for calculation of transport numbers taking R_η into account.

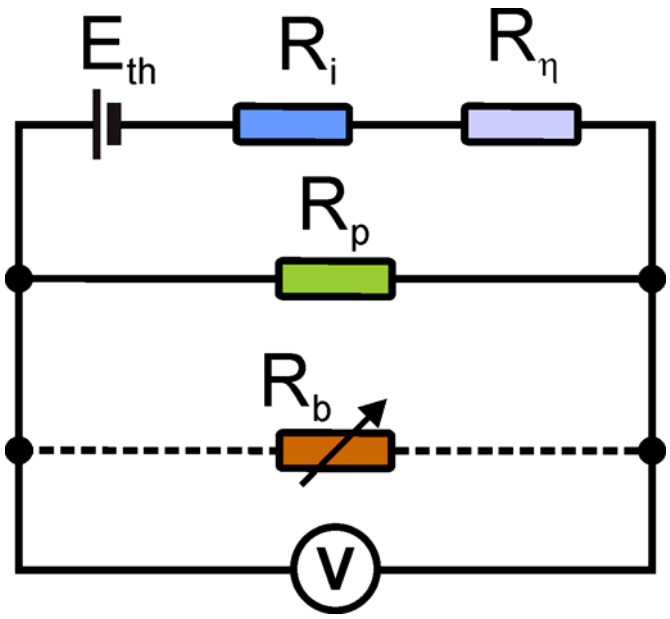

Figure 21: Equivalent circuit for an EMF measurement using the active load method for correcting for electrode polarisation resistance. R_p in this figure corresponds to R_e in equation (42).

Both of these methods were first developed for oxide ion conductors, but work equally well for proton conductors as long as the oxide ion conductivity remains negligible. The active load method requires only a single type of measurement, one that can potentially also give other information about the material. The measurement can also be performed with no applied gradient in chemical potential. At low temperatures and low concentrations of the electroactive species, finding R_T will potentially require very low frequency measurements, making the method fairly time consuming.

In contrast, the active load method works equally well at low temperatures as long as a resistor with suitably high resistance can be employed. This method also allows for precise determination of very small electronic transport numbers, as detailed in the original paper by Gorelov [172].

The measurements on calcium dope samarium titanate were performed at fairly low temperatures (300 – 500 °C), since previous studies had indicated that this was the temperature range where the material is a protonic conductor [86]. At these temperatures, electrode polarisation resistance was expected to be severe, especially in dry and oxidising conditions [176]. Therefore, the active load correction method was preferred. The results of the measurements are summarised in Table 5.

Table 5 Results of EMF measurements on $Sm_{1.92}Ca_{0.08}Ti_2O_{7-\delta}$

			300 °C	400 °C	500 °C
t_O	High p_{O_2}	Uncorrected	-	0	0.073
		Corrected	-	0	0.986
	Low p_{O_2}	Uncorrected	-	-	0.75
		Corrected	-	-	0.991
t_H	High p_{O_2}	Uncorrected	0.08	0.026	0
		Corrected	1.06	0.947	0
	Low p_{O_2}	Uncorrected	0.42	0.34	0
		Corrected	0.876	0.924	0

Essentially, the material appears to be a pure proton conductor at 300 and 400 °C, and a pure oxide ionic conductor at 500 °C, which is in good agreement with the conclusions from both previous and present conductivity measurements. It is also clear that, as expected, the difference between uncorrected and corrected transport numbers is much larger in dry and oxidising atmospheres.

We now turn our attention to the more complicated case of EMF measurements on materials with more than one ionic charge carrier, the most obvious case for oxide based proton conductors being mixed protonic and oxide ionic conductivity. In this work, it is exemplified by SCY at high temperatures.

A commonly made assumption for such systems is that the voltages created by gradients in the individual species are additive, allowing for the total voltage to be calculated as [177-178]:

$$E_{th} = \frac{RT}{4F}\left(t_O\right)\ln\frac{p_{O_2}^2}{p_{O_2}^1} - \frac{RT}{2F}\left(t_H\right)\ln\frac{p_{H_2}^2}{p_{H_2}^1} \quad \textbf{(43)}$$

or, using the equilibrium between hydrogen, oxygen and water vapour

$$E_{th} = \frac{RT}{4F}\left(t_O + t_H\right)\ln\frac{p_{O_2}^2}{p_{O_2}^1} - \frac{RT}{2F}\left(t_H\right)\ln\frac{p_{H_2O}^2}{p_{H_2O}^1} \quad \textbf{(44)}$$

or, equivalently

$$E_{th} = \frac{RT}{2F}\left(t_O\right)\ln\frac{p_{H_2O}^2}{p_{H_2O}^1} - \frac{RT}{2F}\left(t_O + t_H\right)\ln\frac{p_{H_2}^2}{p_{H_2}^1} \quad \textbf{(45)}$$

This approach was also used in paper I, but it has recently been shown to build on some simplifications that can not generally be assumed to hold [179]. The full integral that leads to the simplified equation (38) is

$$E = -\frac{1}{F}\int_1^2 \sum_{k=1}\frac{t_k}{z_k} d\mu_{k*} \quad \textbf{(46)}$$

where μ_{k*} is the chemical potential of the neutral species related to conducting species *k*. For a material with both proton and oxide ion conductivity, this gives the integral

$$E = -\frac{1}{F}\int_1^2 \left(\frac{t_H}{2} d\mu_{H_2} - \frac{t_O}{4} d\mu_{O_2}\right) \quad \textbf{(47)}$$

Since the two thermodynamic variables μ_{H_2} and μ_{O_2} are independent, the integral may depend on the integration path. As stated in [179], this is the case only if

$$\left(\frac{\partial t_H}{\partial \mu_{O_2}}\right)_{\mu_{H_2}} = -\frac{1}{2}\left(\frac{\partial t_O}{\partial \mu_{H_2}}\right)_{\mu_{O_2}} \quad \textbf{(48)}$$

which is not generally the case. This means that the potential is time dependent, which can be managed in experimental design simply by allowing enough time for steady state to be reached. However, it also means that the potential is not uniquely defined by the chemical potential of hydrogen and oxygen at the electrodes.

The method of determining the transport number of one species by applying only a chemical potential gradient of one component while keeping the other one fixed is still theoretically valid. This was the approach taken in Paper I on SCY, using the gas phase equilibrium between hydrogen, oxygen and water vapour. However, if both oxide ionic and protonic conductivity is significant, water vapour may be transported electrochemically through the sample. This leads to a situation where the chemical potential of the relevant species may not be the same at the electrode surface as they are in the gas bulk, making it difficult to control the gradients as intended.

As noted in Paper I, neither of the methods for correcting EMF measurements for the electrode polarisation resistance can easily be applied to systems with two or more ionic charge carriers.

In general, the EMF method, while excellent for systems with only one significant ionic charge carrier, does not seem ideal for determination of transport numbers in materials where both proton and oxide ion conductivity is significant. This is exemplified by the results in Paper I, where EMF measurements for the major carrier, protons, agreed reasonably with expected results and literature values, while those for the minor carrier, oxide ions, were hard to analyse in a way that resulted in meaningful transport numbers.

For obtaining transport numbers in temperature and p_{O_2} ranges where both carriers are expected to have significant conductivity, it is instead recommended to rely on models of defect chemistry and transport based on conductivity and conductivity relaxation measurements. Decoupled transport of protons and oxide-ions upon water uptake has been shown in Fe-doped $SrTiO_3$ [180], allowing for calculation of separate diffusion coefficients. The usefulness of conductivity relaxation techniques for this purpose has

also recently been demonstrated on a few systems [181-182], but the method has not yet found widespread use.

4. Isotope effects in proton conducting ceramics

One property specific to hydrogen is the large relative difference of the mass of its three isotopes, which also leads to significant differences in some material parameters when heavier isotopes are substituted for hydrogen or protons. For the sake of brevity, only deuterium and hydrogen will be treated here, but the theory is equally valid for tritium. The most commonly seen application of this phenomenon to characterisation of proton conductors is comparison of conductivity in hydrogen and deuterium containing atmospheres. If the conductivity of a material is lower when subjected to D_2 and/or D_2O than when subjected to the same concentrations of H_2 and/or H_2O, it is a clear indication that the material is a proton conductor. This effect is what is often referred to in proton conductor literature simply as the isotope effect, and the expected ratio between conductivity in hydrogen containing atmospheres, σ_H, and conductivity in deuterium containing atmosphere, σ_D, is sometimes given as $\sqrt{2}$ for a pure proton conductor, which is rather an oversimplification.

Upon investigating the phenomenon in more depth, it is found that there are two different isotope effects affecting the conductivity; one related to the mobility of the isotope, one related to the its concentration, called the thermodynamic isotope effect. Both stem from the difference in vibration frequency of an O-H and an O-D bond. In a classical approach, a bond between two atoms A and B, with mass m_A and m_B respectively, can be treated as a harmonic oscillator, and the frequency of vibration will be inversely proportional to the square root of the reduced mass, m^*, of the two atoms, defined as

$$m^* = \frac{m_A m_B}{m_A + m_B} \tag{49}$$

Since the mass of hydrogen is much smaller than that of oxygen, it dominates the reduced mass for the O-H bond, analogous to how the lower of the electronic and ionic conductivities dominates the ambipolar conductivity. Therefore, the difference in reduced mass between an O-H and an O-D bond is, to a good approximation, equal to the

difference in mass between a proton and a deuteron, a factor of 2, and the vibration frequency of the O-H bond will be a factor √2 higher than that of an O-D bond.

Since the vibration frequency can be equated to the attempt frequency of proton transport, the mobility of a proton will also be a factor of √2 higher than that of a deuteron. If the problem is instead treated semi-classically, and the difference in zero-point energy is taken to account, an expected difference in activation energy of 0.055 eV is found [183], while the pre-exponential factor is still expected to be a factor √2 higher for transport of protons than for deuterons. This has been treated in more detail elsewhere [183-184].

As seen in chapter 1.2.4, the conductivity depends not only on the mobility, but also on the concentration of the charge carrier. Since the electronic structure of different hydrogen isotopes is identical, the enthalpy of uptake in an oxide should also be the same. However, again due to the difference in vibrational frequency, the entropy, and therefore the Gibb's free energy of uptake will be different [185], giving rise to the thermodynamic isotope effect. This means that the concentration of protons and deuterons in a proton conducting oxide can be different at identical partial pressures of H_2/H_2O and D_2/D_2O. This difference is not as straightforward to calculate as the mobility isotope effect, but the ratio in concentration between protonated and deuterated samples can be large, possibly up to 3.5. Lower temperature and saturation increases the ratio [185].

It should also be noted that applying identical partial pressures of H_2/H_2O and D_2/D_2O to a sample experimentally is difficult. Vapour pressures over water and heavy water at the same temperature are slightly different, and thus, gas bubbled through bottles of the two will have slightly different partial pressures of H_2O or D_2O. Furthermore, the equilibrium constants for the gas phase reaction between oxygen, hydrogen and water and the corresponding deuterium reaction are also not identical, again due to the difference in vibrational frequency of the O-H/O-D bond. Thus, if the same partial pressures of H_2/H_2O and D_2/D_2O are applied to a sample, the p_{O_2} in the two cases will differ slightly.

4.1. The hydrogen isotope EMF cell

It has been shown [186-187] that if an EMF cell is constructed using hydrogen and water vapour in one compartment and the same partial pressures of deuterium and heavy water vapour in the other, a voltage will develop over a proton conducting sample in the cell. The possibility for using such a cell as a hydrogen isotope sensor has also been explored [188-189]. For a pure proton conductor, the open circuit voltage can be calculated as [187]:

$$E_{th} = -\ln\frac{\left(2\mu^0_{D^+} - \mu^0_{D_2}\right) - \left(2\mu^0_{H^+} - \mu^0_{H_2}\right)}{2F} + \frac{RT}{2F}\ln\frac{p_{H_2}}{p_{D_2}}\frac{\gamma^2_{D^+}}{\gamma^2_{H^+}}\frac{u^2_{D^+}}{u^2_{H^+}} \qquad \textbf{(50)}$$

Here, p, γ, and u are partial pressures, activity coefficients and mobilities of the denoted species. μ^0 is the standard chemical potentials of the given species, and so the first term in equation (50) is related to the difference in equilibrium constants for hydrogen and deuterium uptake in the oxide investigated, that is, the thermodynamic isotope effect. As described above, the value of this first term is not well known. From [185] it is known that it will likely be negative, but also that it is likely to be smaller than the mobility term at high temperature, meaning that the overall sign of the EMF cell is positive. This has also been shown experimentally for a series of materials [189].

If instead a pure oxide ion conductor is used, the EMF sign is reversed. This is due to the difference in gas phase equilibrium constant mentioned above, which leads to a slightly higher p_{O_2} in the hydrogen compartment than in the deuterium compartment.

In this work, isotope EMF measurements were conducted on $SrCe_{0.95}Y_{0.05}O_3$ in the temperature range 600 – 950 °C in steps of 25 °C. The results are shown in Figure 22.

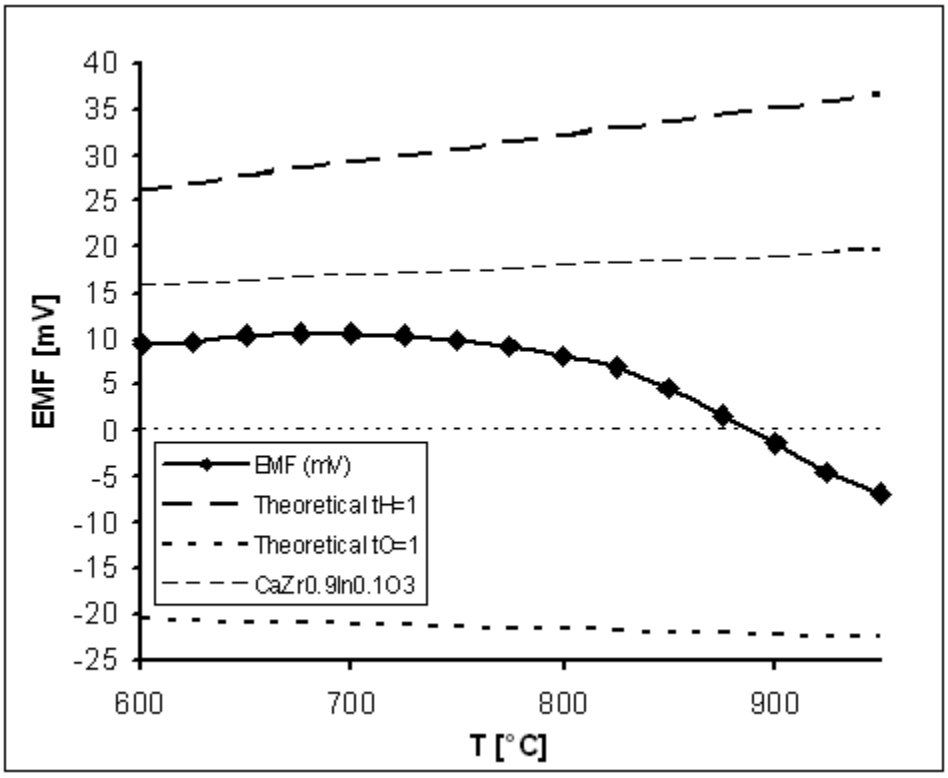

Figure 22 EMF of a H_2/H_2O vs. D_2/D_2O cell, showing the measured data on SCY with the theoretical line for a pure oxide ion conductor, for a pure proton conductor at the top, and for a pure proton conductor ($CaZr_{0.9}In_{0.1}O_3$) from [186].

The theoretical line for pure proton conductivity is calculated under the assumption that protons and deuterons are equally soluble in the material, that is, the first term of equation (50) equals zero. This assumption is likely to be invalid, and the given theoretical values too high. Measured EMF values for known pure proton conductor $CaZr_{0.9}In_{0.1}O_3$ are also shown. Again, this line might not be valid as a theoretical maximum for pure protonic conductivity in other oxides, since the thermodynamic isotope effect may have different values. The theoretical line for t_O is calculated using well established thermodynamic data for the two gas phase equilibria. For example, the SCY used here was doped to a smaller degree (5 %), which is expected to have some influence. Lacking data to estimate a proper value for the first term in equation (50), the data can only be qualitatively analysed. It is clear that the slope of the measured curve is almost identical to the one measured for indium doped calcium zirconate up to around 700 °C. This is an indication that the conductivity is mainly protonic. This is in good agreement with the regular EMF

measurements reported in paper I, where the t_H was found to be >0.98 in wet reducing conditions at 600 °C. Above 700 °C, the EMF drops off as the temperature is increased, indicating a decreasing transport number for protons. Since it becomes negative rather than zero at higher temperatures, it must be oxide ionic conductivity taking over, rather than electronic. If an extrapolation of data up to 700 °C is taken as the correct theoretical EMF value for pure proton conductivity, transport numbers for oxide ions and protons as a function of temperature can be calculated from the data. This is shown in Figure 23.
These values do not take electronic conductivity into account however, and it would probably be more accurate to see them as a measure of how large a part of the ionic conductivity the two charge carriers contribute to, rather than true transport numbers.

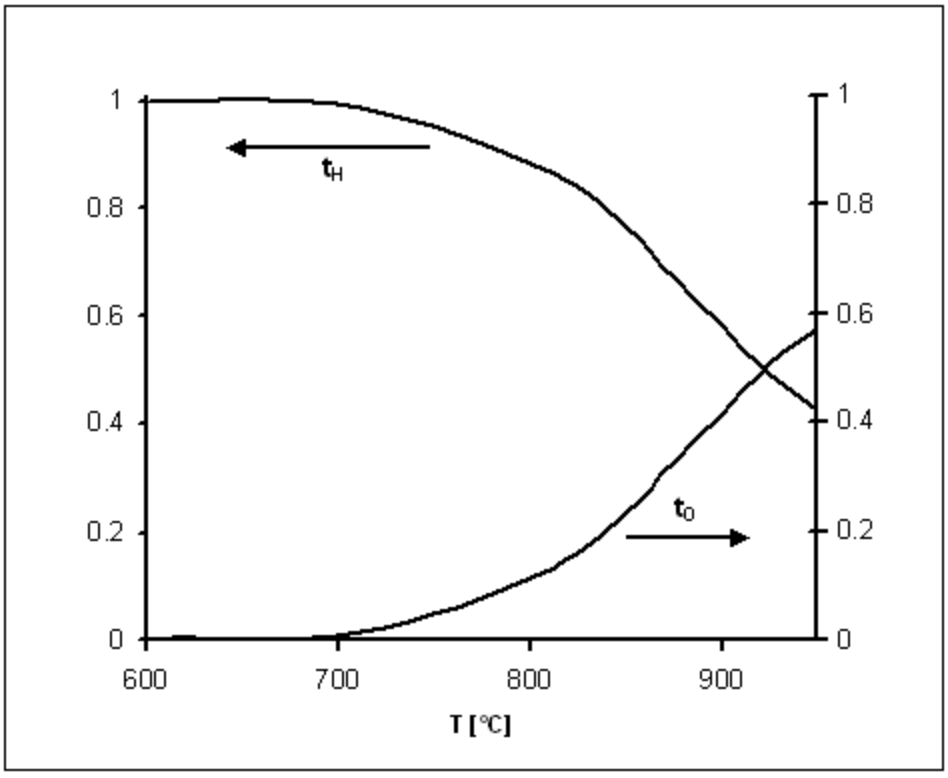

Figure 23 Transport numbers for protons and oxide ions in SCY from the isotope concentration cell

5. Flux measurements

While the previous measurement methods have focused on determining partial conductivities and transport numbers and, from those, calculating a possible ambipolar transport of hydrogen through a material. The most direct way to experimentally determine whether a substance is suitable for a hydrogen membrane is to measure the flux of hydrogen through a sample of it. Therefore, a number of such measurements were made in this work.

The same rig was used as for the EMF measurements, after replacing the harness held in place by kanthal wires with an alumina ring held in place by two alumina pull-rods, see Figure 24. This modification leaves only ceramic parts in the hot part of the furnace, allowing a higher temperature to be used for the sealing process and thus obtaining a better seal.

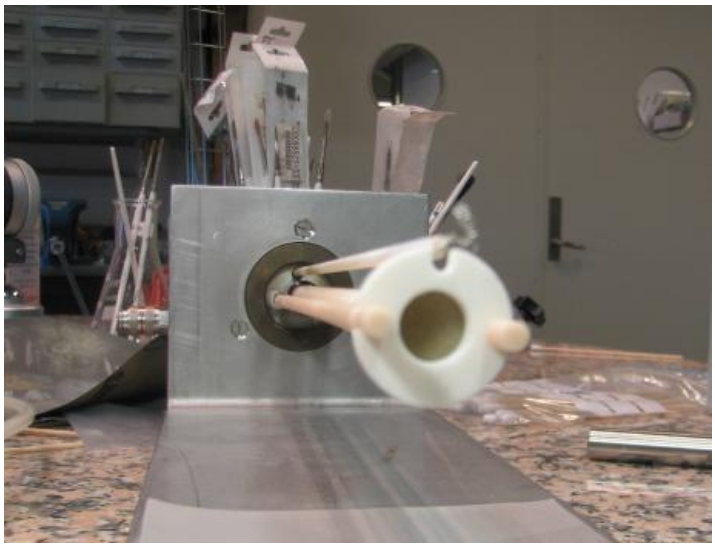

Figure 24 The flux rig, showing the alumina sample holder and pull rods.

No electrodes were used on the samples for these measurements, and the alumina tube containing a platinum wire for electric contact to the inner surface of the sample was removed, since no electrical measurements were necessary. The gas mixing system for

supplying gas to the in- and outside of the sample was the same as described in the chapter on EMF measurements.

By far the most common method in literature of measuring hydrogen fluxes is gas chromatography (GC). Using a thermal conductivity detector (TCD) and a column specifically designed for hydrogen detection, reliable measurements of down to 10 ppm can be made (see e.g.[191]), with 100 % selectivity for hydrogen. The robustness and ease of use of dedicated systems easily outweighs the minor drawbacks of not being able to measure in line, but having to sample gas and a typical analysis time of around 3 minutes.

Mass spectrometry (MS) is also commonly used, despite having a high detection limit for hydrogen and requiring relatively high maintenance. Ideally, MS is not used as a stand-alone detection system, but coupled with a gas chromatograph. This gives the benefit of the detection limit of the GC with the capability to easily detect leaks with the MS by including e.g. helium or argon in the feed stream.

For the measurements in this work, a different detection system was used, utilizing the moisture meter described earlier. The permeate gas was mixed with a small flow of pure dry oxygen, and then led through a small furnace, consisting of an insulated heating winding and an alumina tube, held at 800 °C. Although hydrogen and oxygen should react spontaneously at this temperature, a catalyst was employed to ensure that full reaction took place. The catalyst consisted of finely dispersed platinum on a fibrous alumina support. The catalyst was made by first preparing a hexacholoroplatinic acid solution by dissolving used but clean platinum wire in hot aqua regia [192]. Nitric acid was constantly added to compensate for the evaporation of nitrogen dioxide.

$$Pt + 4HNO_3 + 6HCl \rightarrow H_2PtCl_6 + 4NO_2 + 4H_2O$$

When all the platinum had been dissolved, the solution was evaporated almost fully and further hydrochloric added several times to remove any $(NO)_2PtCl_6$. The support material was cut in strips to fit within the furnace tube, and infiltrated with the hexachloroplatinate solution. The strips were then heat treated at 600 °C to get metallic platinum according to the following reactions [193]:

$$H_2PtCl_6 \cdot nH_2O \xrightarrow{220°C} PtCl_4 + 2HCl + nH_2O$$
$$PtCl_4 \xrightarrow{350°C} PtCl_2 + Cl_2$$
$$PtCl_2 \xrightarrow{510°C} Pt + Cl_2$$

The gas was led from the reaction furnace to the moisture meter, and the content of hydrogen or water calculated from the water content. To verify that all the hydrogen had been converted, the p_{O2} of the gas was measured after the moisture meter. A diagram of the setup is shown in Figure 25.

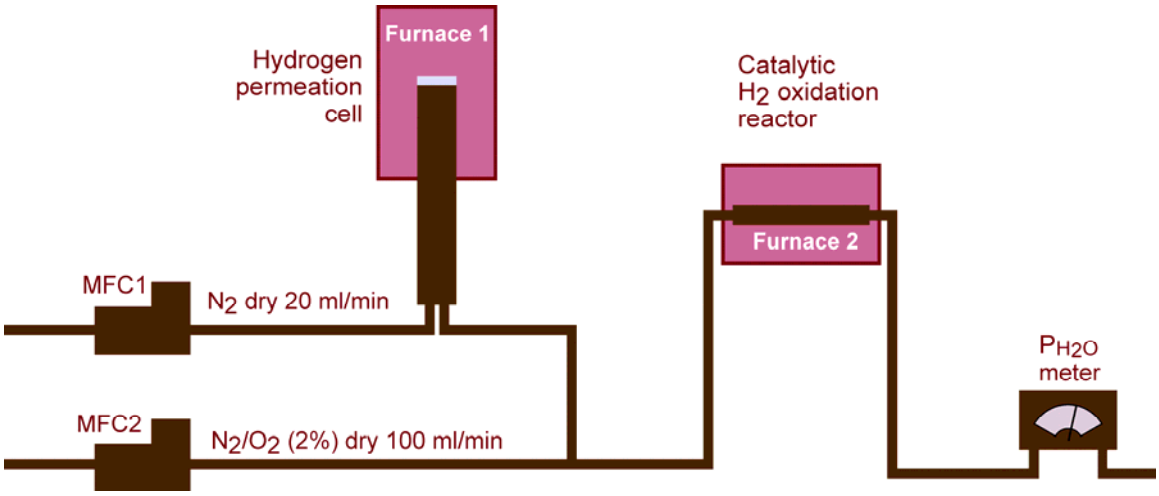

Figure 25 Diagram of the flux measurement setup

The sensitivity of this detection method is determined by the sensitivity of the moisture meter, and a detection limit of around 200 ppm of hydrogen is expected, with a precision of ±2%, which is sufficient for our purposes as long as flow rates are kept reasonably low. The response time was shown to be entirely determined by the flow of the gas through the tubes, provided the reaction furnace remained hot. If it was allowed to cool, 2-4 hours was needed for start up, due to a large amount of water vapour in the system. Most probably, this is due to water adsorption on the surface of the catalyst.

A comparable setup has previously been used in our labs for determination of oxygen permeation, mixing the permeate gas with a dilute hydrogen stream [194], and

conceptually similar detection methods have also been applied in measurements of hydrogen permeability [195].

One great disadvantage of this detection method is the lack of a "built in" check for leaks. The moisture meter is only sensitive to water vapour. This was solved by performing leak checks using a modified setup originally constructed for leak testing ceramic samples. The setup consists of a vacuum pump, a digital flow meter and a manometer connected in series, with a footswitch to direct the flow through the end piece or a bypass. In the original setup, the end piece consists of a stainless steel tube with a soft rubber ring at the end. This allows for easy spot wise leak testing of ceramic samples, to reveal pinholes, but is not useful for testing the flux setup. Instead, the end piece was replaced by a t-piece nylon tube that could be attached to the in- and outlet of the permeate side of the rig, creating a closed system provided the seal and sample were tight. This method does not give a quantitative measure of the leak rate, but as a qualitative test this method is strong, even small leaks give a clear reading. However, when looking for future improvements for the rig, a reliable and continuous way to get quantitative measurements of the leak rate should be strongly considered. Measurements of hydrogen content in the permeate gas at room temperature, where there will be no electrochemical transport, can also serve as a check for leaks. Again, the method gives no qualitative measure of the leak rate, since it is temperature dependent (although to a far lesser degree than electrochemical transport). Performing room temperature measurements at a regular basis during a measurement series would be impractical as it is very time consuming, since cooling and heating must take place at low rates to protect the seal and sample from damage due to TEC (thermal expansion coefficient) mismatch. A single measurement of this type was performed at the end of each measurement series though, since the cell was cooled regardless.

The first set of flux measurements was made on $SrCe_{0.95}Y_{0.05}O_{3-\delta}$, the same sample that was used for EMF measurements. The platinum electrodes were removed, and the surface ground with increasingly fine silicon carbide paper to remove any remnants of the platinum paint and smooth the surface of the pellet. As before, the finest paper used was grit 1000, since polishing the samples finer seemed to decrease the likeliness of forming a

good seal. After grinding, the pellet was 1.45 mm thick. It was sealed on the alumina tube using two 0.2 mm thick gold rings at 1020 °C.

Measurements were performed at 5 different gas settings; a measurement of nitrogen with 1 % water vapour versus dry nitrogen, and dry and wet (1 % water vapour) measurement of 6 % hydrogen in nitrogen versus dry nitrogen and versus dry nitrogen with approximately 0.25 % hydrogen. The first measurement gives a measure for water permeation due to mixed oxide ionic and protonic conduction, although at an undefined gradient. Measurements with no hydrogen in the carrier gas give a large, but undefined gradient in hydrogen, while putting hydrogen in the stream gives a fixed gradient but smaller in magnitude, and thus a smaller expected flux. Dry and wet measurements were made to see the effect of water vapour on the flux. All five gas settings described above were tested at 750, 800, 850 and 900 °C. In this measurement series, measurements were also made with varying total flow rates to see if that would influence the results. Since the sample is thick enough that the electrochemical transport of hydrogen is expected to be entirely controlled by sample thickness, and not on surface kinetics, and therefore not on the flow rate of the feed stream, only the partial pressure of hydrogen and water, and a dependency of the flux on the flow rate could indicate leaks. No such dependency was found, and thus only results from measurements at one constant flow rate will be presented. No pure water flux was found at any of the temperatures either. The fluxes measured on SCY are presented in Figure 26.

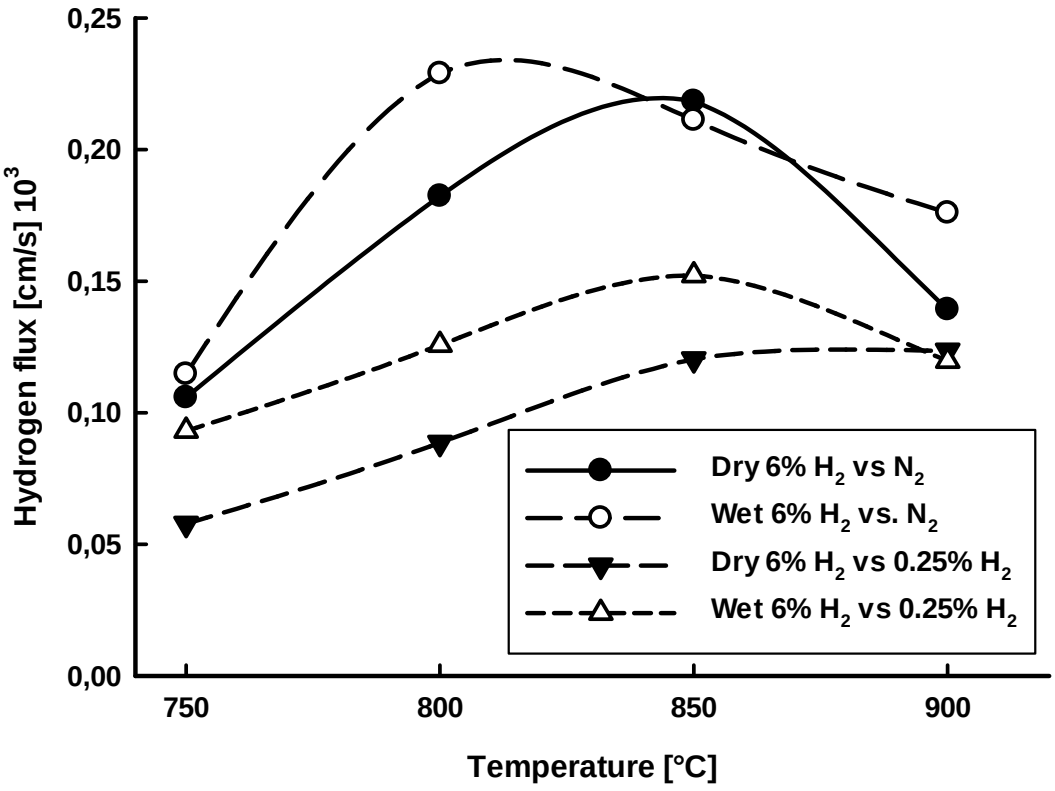

Figure 26 Hydrogen flux measured through $SrCe_{0.95}Y_{0.05}O_{3-\delta}$

The maximum flux of 0.23 10^{-3} cm/s was found in the measurement of wet 6 % hydrogen versus dry nitrogen at 800 °C. As expected, the measurements where dilute hydrogen was also used on the inside of the membrane showed a lower flux. At lower temperatures, using wet gas on the feed side of the membrane gave a higher flux, at higher temperatures this effect was less pronounced. The general drop off in flux seen at 900 °C is due to the diminished concentration of protons in the sample at this temperature.

Flux measurements were also performed on the nickel-containing sample with nominal composition $SrCe_{0.85}Y_{0.15}Ni_{0.02}O_{3-\delta}$. The sample was ground as described previously to a thickness of 1.80 mm and sealed to the alumina rig using two gold sheet rings with a total thickness of 0.4 mm. The sealing temperature used was 1020 °C and the system was found to be leak tight before the measurements. As described in the previous chapter, the actual composition of this sample, including the nickel content, was not well defined. Measurements were performed at the same temperatures and gas settings as for the SCY sample. The data are presented in Figure 27.

During these measurements, there were some fluctuations in the reading of the moisture meter, particularly when using hydrogen in the carrier gas. The reason for this has not been found, but it probably influenced the accuracy of the measurements. It must also be noted that after the measurement was finished, the system was found not to be leak tight. A significant hydrogen flux was measured at room temperature, where electrochemical transport is completely implausible. However, a flux of water, using 1% water in the feed stream, was also measured at room temperature. No water flux was measured at 800 or 750 °C, the latter of which was the last temperature measured at. It is therefore concluded that the leak was formed during cool down of the cell, after the measurements were concluded, possibly due to using an excessive cooling rate. However, the possibility that the system was already leaking while the measurements were made and the leak worsened during cool down cannot be discounted entirely.

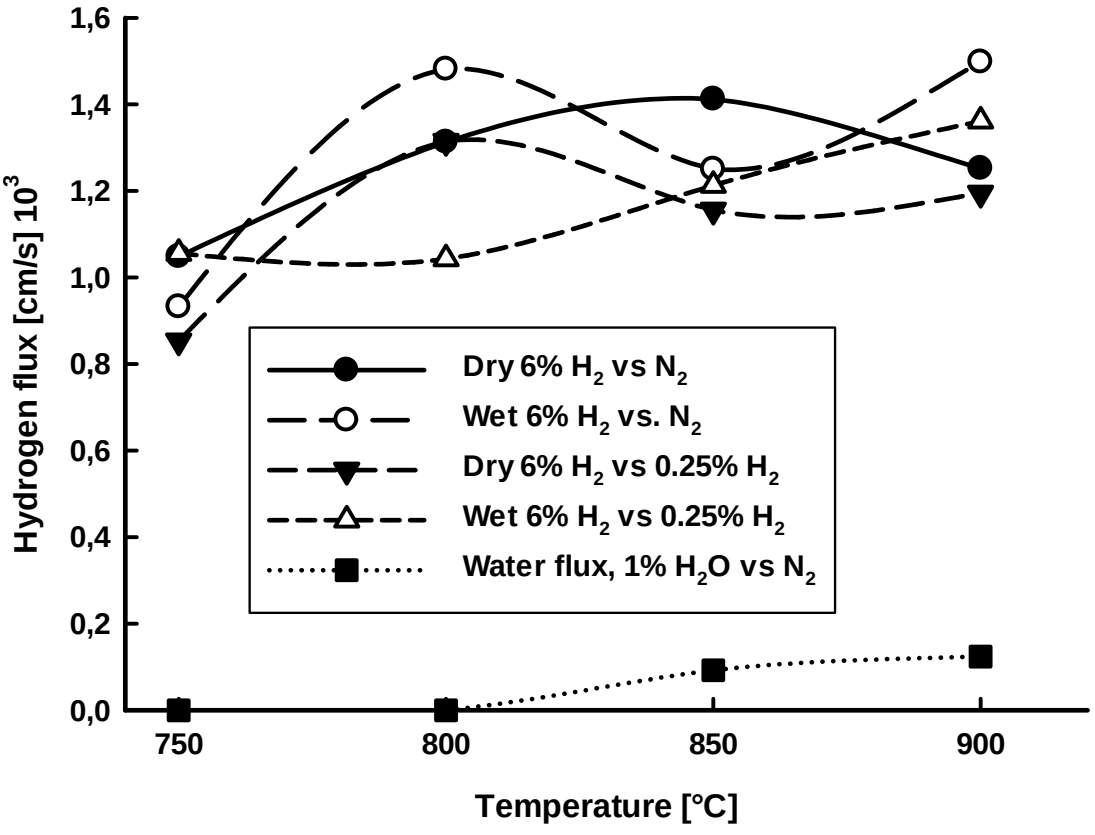

Figure 27 Hydrogen and water fluxes measured through "$SrCe_{0.83}Y_{0.15}Ni_{0.02}O_{3-\delta}$"

The of water that becomes measurable at 850 and 900 °C indicates (assuming that it is not due to leakage) a significant oxide ionic conductivity in the sample, and the overall increased hydrogen flux indicates increased electronic conductivity, since that is what is limiting the flux in SCY with no nickel. It is known that some K_2NiF_4-type oxides exhibit mixed oxide-ionic electronic conductivity, and the presence of such a phase could explain the measured fluxes.

Flux measurements were also attempted on other compositions, including $BaCe_{0.2}Zr_{0.7}Y_{0.1}O_{3-\delta}$ (BCZY27) with 2 % nickel and $La_2Ce_2O_7$, but, despite several attempts on both systems, good enough sealing could not be achieved with the same method used for the SCY systems above. The temperature was increased to circa 1050 °C for some of the latter sealing attempts, but since some joints in the of the furnace and rig were tightened using an epoxy, too high a temperature might cause leaks here instead due to decomposition of organic adhesives. The reason for the lack of success with sealing these materials even at a higher temperature than what was used for SCY has still not been found. The most obvious explanation would be a larger mismatch in thermal expansion coefficient between the alumina tubes and the sample of the materials for which no seal was achieved than for SCY. The TEC for alumina in the relevant temperature range is 7.8 – 8.5 10^{-6} K^{-1} [196-197]. That of $SrCe_{0.95}Y_{0.05}O_{3-\delta}$ was measured to be 10.05 10^{-6} K^{-1} in this work, using dilatometry in the temperature range 25 – 1000 °C with a ramp rate of 2 °C/min. The TEC of BCZY27 is lower, around 8.9 10^{-6} K^{-6}, and thus matches that of alumina better than SCY. The expansion coefficient of $La_2Ce_2O_7$ has not been investigated.

Gold has a significantly higher TEC, 18.3 10^{-6} K^{-1} at 878 °C. Since very low cooling rates (0.1-0.3 °C/min) were used after heat treatment in each sealing attempt, the large TEC mismatch between the gold and the ceramic components should not cause a good seal to fail during cooling; the gold should have ample time to relieve any thermal stress at the temperatures employed. Further work would be required to fully understand this matter.

6. Membrane materials

In this chapter, the values for hydrogen flux reported in the previous chapter will be compared to those calculated from the equations given in 1.2.4, as well as to values found for other similar materials studied in literature. We remind ourselves that the US DOE target value for hydrogen permeation for applications is 91.5 $m^3/h/m^2$ (see Table 1), or in the units used here, 2.54 cm/s, which is equivalent to 6.81 mmol hydrogen pr. minute pr. square centimetre. When those flux values are far from being achieved for any of the materials presented, it is due to the fact that those measurements are all performed on thick samples. Significantly increased fluxes would be expected from dense thin supported membranes.

The comparison to literature data is limited to oxide systems, rather than also including metal based membrane materials. For several metals, the DOE 2015 flux targets are met, and their practical applicability is limited by stability and surface kinetics [198].

To calculate theoretical values for the flux in SCY, equation (28) was used. Conductivity values were calculated from the measurements performed in this work at 600 °C, using the activation energies found in [19] for ionic conductivity and σ_n^0. Ionic conductivity was assumed constant over the membrane, but since oxide-ionic conductivity becomes prevalent as temperature increases, it was corrected by the transport number found in the hydrogen isotope EMF measurement, Figure 23. The hydrogen partial pressure gradient was assumed to be linear over the sample. This allowed for a numerical integration of the ambipolar conductivity over the sample. The resulting calculated fluxes are compared to those measured in Figure 28. As shown, the measured fluxes are approximately 1.5-2 times higher than the calculated ones, with the difference increasing with temperature. The general trend of the data agrees well with the theoretical calculations. The difference is most likely caused by underestimation of the electronic conductivity in the calculations, or by undetected leaks in the measurements. Since the error grows larger as the temperature increases, it seems likely that at least part of the error is due to using too small an activation energy for one or both of the conductivities.

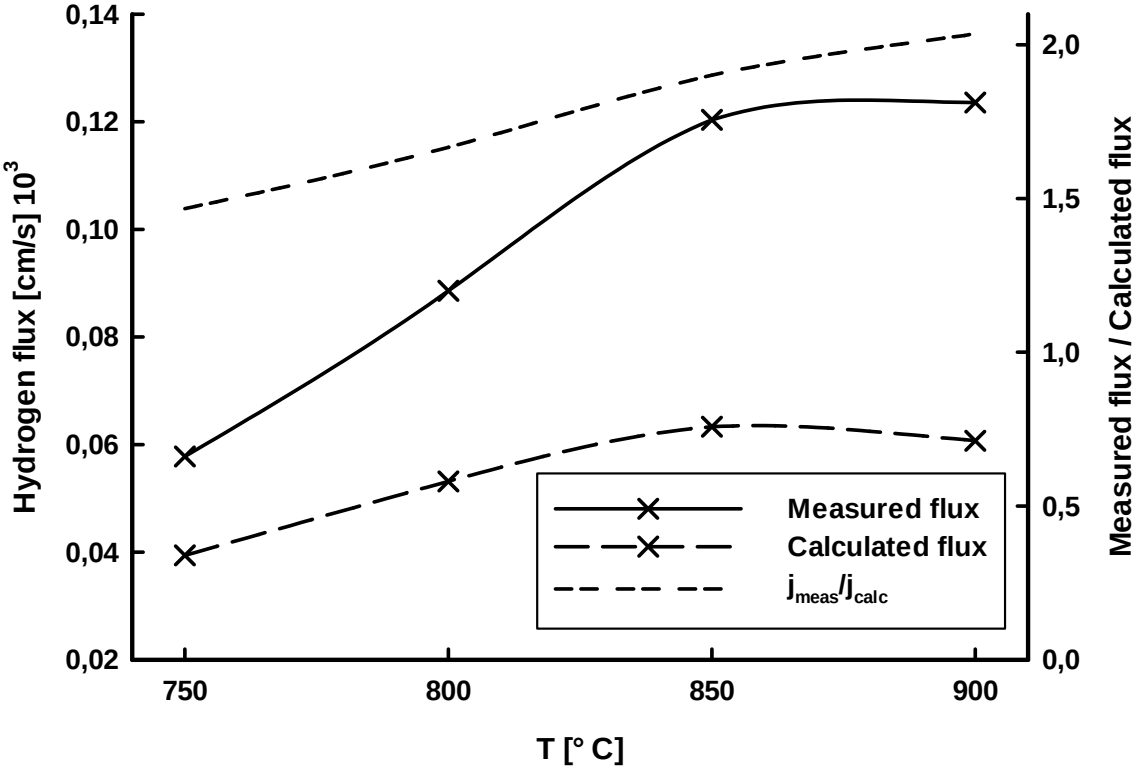

Figure 28 Comparison between measured and calculated hydrogen fluxes for $SrCe_{0.95}Y_{0.05}O_{3-\delta}$

A comparison between measured and fluxes will not be made for the nickel-containing sample. The measured conductivities do not justify the increased flux compared to SCY without nickel. This flux therefore must stem from one of two sources, neither of which can be calculated without further information; either it is due to incomplete sealing of the sample, or it is due to the secondary K_2NiF_4 type phase. XRD showed only a small amount of this phase remaining in the sample after the surface layer had been removed, and it seems somewhat unlikely that it percolates the sample contributing enough to the conductivity to explain the flux measured.

We will now compare the flux measured on SCY here with other similar studies reported in literature where good agreement between the theoretical and measured fluxes has been found. All systems are based on perovskite materials. Three are single phase, $BaCe_{0.8}Y_{0.1}Ru_{0.1}O_{3-\delta}$ [199], $SrCe_{0.95}Eu_{0.05}O_{3-\delta}$ and $SrCe_{0.95}Sm_{0.05}O_{3-\delta}$ [35]. The last two are

composites; one cer-cer based on two different perovskites, 0.8 $SrZrO_3$ 0.2 $SrFeO_3$ [200], and the other a cermet consisting of 40 volume % Ni and 60 % $SrCe_{0.8}Yb_{0.2}O_{3-\delta}$ [166].

The measurements on these samples were not all performed under the same experimental conditions and are therefore not directly comparable as is. However, for all of the above compositions, measurements have been made at 800 and/or 850 °C in dry conditions. For the measurements in [166], the sweep gas contained a small amount of hydrogen, thus allowing for normalisation with regards to both sample thickness and hydrogen gradient. In [199] and [200], the logarithm to the hydrogen partial pressure ratio is given. This enables a comparison of the results if the ambipolar conductivity is assumed to take an average value over the sample. Comparisons of measured fluxes normalised to the sample thickness and hydrogen gradient used in this work is given in Table 6.

In [35], pure helium was used as a sweep gas. The fluxes measured in that work will be compared to those measured using pure nitrogen in the permeate side in this work, noting that higher concentration of hydrogen in the feed stream (10 %) was used in that work as compared to here (6 %). These values are harder to compare. In this work, a flux of 0.218×10^3 cm/s was measured at 850 °C using dry 6 % hydrogen on the feed side and dry nitrogen as the sweep gas. With He as the sweep gas and 10 % hydrogen as feed gas, fluxes of 0.012×10^3 and 0.025×10^3 cm/s were measured for samarium and europium doped strontium cerate respectively, normalising to the sample thickness of this work.

Table 6 Comparison of hydrogen flux measurements normalized to sample thickness and hydrogen gradient used in this work.

Composition	Temperature [°C]	Reference	Normalised flux [cm/s]×1000
$SrCe_{0.95}Y_{0.05}O_{3-\delta}$	800	This work	0.053
$SrCe_{0.95}Y_{0.05}O_{3-\delta}$	850	This work	0.063
$SrCe_{0.83}Y_{0.15}Ni_{0.02}O_{3-\delta}$	800	This work	1.32
$BaCe_{0.8}Y_{0.1}Ru_{0.1}O_{3-\delta}$	800	[199]	0.289
0.8 $SrZrO_3$ 0.2 $SrFeO_3$	850	[200]	0.085
$SrCe_{0.8}Yb_{0.2}O_{3-\delta}$:Ni	800	[166]	0.200
$SrCe_{0.8}Yb_{0.2}O_{3-\delta}$:Ni	850	[166]	0.249

Of the values shown here, the ones found in this work are the lowest. Yttrium and ruthenium doped barium cerate showed the highest flux, but the material was also shown to have significant oxide ionic conductivity. The two composite materials also show higher hydrogen permeability than SCY, indicating that such mixtures of proton conducting and electron conducting phases may prove a viable way of reaching higher hydrogen fluxes if explored further.

7. Summary

This work has treated some experimental aspects of development of high temperature oxide based hydrogen permeable membranes. Relevant background material and theoretical considerations have been treated in depth. Four materials have been treated; $SrCe_{0.95}Y_{0.05}O_{3-\delta}$, $SrCe_{0.85}Y_{0.15}O_{3-\delta}$ with small amounts of nickel, La_2MgTiO_6 and $Sm_{1.92}Ca_{0.08}Ti_2O_7$.

The samarium titanate was characterised using conductivity and EMF measurements in the temperature range 300 – 500 °C. It was found to be primarily an oxide ion conductor at 500 °C and a proton conductor at lower temperatures. The low conductivity and lack of electronic component makes the material unsuitable for use in hydrogen membrane applications, but the EMF measurements clearly demonstrated the value of being able to correct for electrode polarisation resistances.

Only a small number of measurements were made on La_2MgTiO_6. It was shown that the electronic conductivity of this material can be increased dramatically by sintering samples in reducing conditions. The protonic conductivity of this material has been demonstrated, although it is fairly low. If it can be retained, or even increased, in the reduced state, it could potentially allow for reasonable hydrogen fluxes.

The strontium cerates were characterised using conductivity measurements, and for the non-nickel containing material also EMF. Hydrogen flux measurements were also performed on $SrCe_{0.95}Y_{0.05}O_{3-\delta}$ and $SrCe_{0.83}Y_{0.15}Ni_{0.02}O_{3-\delta}$. Measurements on the composition without nickel agreed well with literature. The EMF measurements emphasised the difficulties of using this method to determine both transport numbers for protons and for oxide ions in materials where both contribute significantly to the total conductivity. The conductivity measurements did not show an improvement of ionic conductivity, but a slight increase in p-type electronic conductivity in dry oxidising conditions. From the conductivity data, the hydrogen flux was not expected to be higher in the Ni-containing sample, but a significant increase was found. This could be due to a small amount of secondary phase in the sample which was not present in the conductivity measurement sample, but was more likely due to insufficient sealing of the sample.

Reasonable agreement was found between measured and calculated flux for $SrCe_{0.95}Y_{0.05}O_{3-\delta}$ and other similar studies in literature.

8. Outlook

High temperature proton conducting oxides is still a relatively young research field, being started only 30 years ago by the work of Iwahara. Most of the scientific effort has been going into fundamental research and developing pure proton conductors for use in fuel cells. Research specifically targeting mixed protonic-electronic conductivity for hydrogen permeation membranes has of course also been performed, but not in the same volume. If materials could be found that exhibit a high enough hydrogen flux, they would have a very high potential for use in a wide variety of technological applications in a society based on sustainable energy, as well as in the transition towards such a society.

In oxide based proton conductors, there is always a potential for oxide-ion conductivity being present as well, especially at increased temperatures. Methods for accurately assessing transport numbers for minor contributions of oxide-ion conductivity in a primarily protonic conductor and vice versa should be developed, as it is difficult to get reliable figures under such circumstances with the commonly used EMF method. Conductivity relaxation measurements would present a viable alternative, and measurements on suitable model compounds should be undertaken.

In this work, some interesting preliminary results were achieved on off stoichiometric La_2MgTiO_6 and the hydrogen flux through yttrium doped $SrCeO_3$ was increased by introducing nickel. As outlined in the respective chapters, in both cases, a number of new questions arose from the measurements, and attempting to answer those could lead to both a better understanding of proton conductors in general and to development of materials with significant ambipolar conductivity.

9. Acknowledgement

First and foremost I would like to thank my main supervisor, Nikolaos Bonanos, for excellent scientific guidance, inspirational discussions and great support. I could not have wished for a better supervisor.

I would also like to thank my second supervisor, John W. Phair for great advice and assistance throughout my work.

I am grateful to Risø – DTU for giving me the opportunity and funding for this work through the "Initiative for Hydrogen Permeable Membranes".

The great open working environment of the Solid State and Fuel Cells Division at Risø and the many discussions with colleagues will be missed. Especially fellow protonic workers Nicolai Bork, Sandrine Ricote, Finn Willy Poulsen and Francesco Bozza have contributed to this work with valuable discussions and exchange of experiences, as has Henrik Lund Frandsen and the members of the membrane work group. Associate Prof. Torben Jacobsen provided valuable advice concerning the hydrogen catalytic oxidiser.

The extraordinary technical personnel of the division have also greatly facilitated this work, solving problems in mere hours that would otherwise keep me stuck for months. I am very grateful for their help.

A big thank you should also go to the group of Truls Norby at the University of Oslo, including Skjalg Erdal and Camilla Vigen, for many interesting and fruitful discussions, as well as economic support for several well-arranged meetings.

The great collaboration with colleagues at Gothenburg University, Karinh Eurenius, Elisabet Ahlberg and Chris Knee was much appreciated, as was their hospitality.

I am grateful for economic support from the TYK fund in connection with the SSPC 14 conference, and from Dr. Koji Amezawa for the 4th meeting on nano ionics in Sendai.

And last but not least I would like to thank my lovely family for their never ending support throughout the project.

10. References

[1] R. Carson, *Silent Spring,* Houghton Mifflin, New York, USA, 1962
[2] D. H. Meadows, D. L. Meadows, J. Randers and W. W. Behrens, *Limits to Growth,* Universe Books, New York, USA, 1972
[3] H. Rodhe, *Science,* 248 (1990), p. 1217
[4] *World Energy Outlook 2008*, International Energy Agency, Paris, France, 2008
[5] US Energy Information Administration, http://www.eia.gov/cfapps/ipdbproject/iedindex3.cfm, accessed Nov 15th 2010
[6] C. J. Campbell and J. H. Lahèrrere, *Scientific American,* 278 (1998), p. 1528
[7] C. J. Cleveland, *Energy,* 30 (2005), p. 769
[8] C. A. S. Hall, M. C. Herweyer and A. Gupta, *Unconventional Oil: Tar Sands and Shale Oil – EROI on the Web, Part 3 of 6,* The Oil Drum, http://www.theoildrum.com/node/3839, accessed Nov. 10th 2010
[9] H. L. MacLean and L. B. Lave, *Progress in Energy and Combustion Science,* 29 (2003), p. 1
[10] K. L. Lim, H. Kazemian, Z. Yaakob and W. R. W. Daud, *Chemical Engineering & Technology,* 33 (2010), p. 213
[11] C. Graves, S. D. Ebbesen, M. Mogensen and K. S. Lackner, *Renewable and Sustainable Energy Reviews,* 15 (2011), p. 1
[12] D. G. Thomas and J. J. Lander, *Journal of Chemical Physics,* 25 (1956), p. 1136
[13] J. D. Fowler, D. Chandra, T. S. Elleman, A. W. Payne and K. Verghese, *Journal of the American Ceramic Society,* 60 (1977), p. 155
[14] R. M. Roberts, T. S. Elleman, H. Palmour III and K. Verghese, *Journal of the American Ceramic Society,* 62 (1979), p. 495
[15] T. Takashami, H. Iwahara, *Revue de Chimie Mineale,* 17 (1981), p. 243
[16] T. Yajima, H. Suzuki, T. Yogo and H. Iwahara, *Solid State Ionics,* 51 (1992), p. 101
[17] H. Iwahara, T. Esaka, H. Uchida and N. Maeda, *Solid State Ionics,* 3-4 (1981), p. 359
[18] R. J. Phillips, N. Bonanos, F. W. Poulsen and E. O. Ahlgren, *Solid State Ionics,* 125 (1999), p. 389
[19] E. O. Ahlgren, Hansen, N. Bonanos, F. W. Poulsen, M. Mogensen, in the Proceedings of the 17th Risø International Symposium on Materials Science, Risø, Denmark, 1996
[20] H. Iwahara, H. Uchida, K. Ono and K. Ogaki, *Journal of the Electrochemical Society,* 135 (1988), p. 529
[21] N. Bonanos, B. Ellis, K. S. Knight and M. N. Mahmood, *Solid State Ionics,* 35 (1989), p. 179
[22] N. Bonanos, B. Ellis and M. N. Mahmood, *Solid State Ionics,* 44 (1991), p. 305
[23] J. F. Liu and A. S. Nowick, *Solid State Ionics,* 50 (1992), p. 131
[24] R. C. T. Slade and N. Singh, *Solid State Ionics,* 61 (1993), p. 111
[25] H. Iwahara, T. Yajima, T. Hibino, K. Ozaki and H. Suzuki, *Solid State Ionics,* 61 (1993), p. 65
[26] R. C. T. Slade, S. D. Flint and N. Singh, *Solid State Ionics,* 82 (1995), p. 135
[27] S. Weinströer and H.-D. Weimhöfer, *Solid State Ionics,* 101-103 (1997), p. 1113
[28] K. H. Ryu and S. M. Haile, *Solid State Ionics,* 125 (1999), p. 355
[29] K. Katahira, Y. Kohchi, T. Shimura and H. Iwahara, *Solid State Ionics,* 138 (2000), p. 91
[30] S. Ricote, N. Bonanos and G. Caboche, *Solid State Ionics,* 180 (2009), p. 990
[31] S. Ricote, N. Bonanos, M. C. Marco de Lucas and G. Caboche, *Journal of Power Sources,* 193 (2009), p. 189
[32] J. Guan, S. E. Dorris, U. Balachandran and M. Liu, *Solid State Ionics,* 110 (1998), p. 303
[33] D. Dionysiou, X. Qi, Y. S. Lin, G. Meng and D. Peng, *Journal of Membrane Science,* 154 (1999), p. 143
[34] T. Tsuji and T. Nagano, *Solid State Ionics,* 136-137 (2000), p. 179
[35] S.-J. Song, E. D. Wachsman, J. Rhodes, S. E. Doris and U. Balachandran, *Solid State Ionics,* 167 (2004), p. 99
[36] S.-J. Song, E. D. Wachsman, J. Rhodes, H.-S. Yoon, K.-H. Lee, G. Zhang, S. E. Dorris and U. Balachandran, *Journal of Materials Science,* 40 (2005), p. 4061
[37] M. Matsuka, R. Braddock and I. Agranovski, *Solid State Ionics,* 178 (2007), p. 1011
[38] X. Wei and Y. S. Lin, *Solid State Ionics,* 178 (2008), p. 1804

[39] T.-K. Oh, H. Yoon and E. D. Wachsman, *Solid State Ionics,* 180 (2009), p. 1233
[40] X. Wei, J. Kniep and Y. S. Lin, *Journal of Membrane Science,* 345 (2009), p. 201
[41] G. C. Mather, D. Poulidi, A. Thursfield, M. J. Pascual, J. R. Jurado and I. S. Metcalfe, *Solid State Ionics,* 181 (2010), p. 230
[42] S. Shin, H. H. Huang and M. Ishigame, *Solid State Ionics,* 40-41 (1990), p. 910
[43] M. Glerup, F. W. Poulsen and R. W. Berg, *Solid State Ionics,* 148 (2002), p. 83
[44] I. Kosacki, J. G. M. Becht, R. van Landschoot and J. Schoonman, *Solid State Ionics,* 59 (1993), p. 287
[45] R. Hempelmann, *Physica B,* 226 (1996), p. 72
[46] H. Iwahara, H. Uchida and N. Maeda, *Journal of Power Sources,* 7 (1982), p. 293
[47] T. Norby and P. Kofstad, *Solid State Ionics,* 20 (1986), p. 169
[48] K. D. Kreuer, E. Schönherr and J. Maier, *Solid State Ionics,* 70-71 (1994), p. 278
[49] C. J. T. de Grotthuss, *Ann. Chim.*, 58 (1806), p. 54
[50] A. S. Nowick and Y. Du, *Solid State Ionics,* 77 (1995), p. 137
[51] H. G. Bohn, T. Schober, T. Mono, W. Schilling, *Solid State Ionics,* 117 (1999), p. 219
[52] T. Norby and N. Christiansen, *Solid State Ionics,* 77 (1995), p. 240
[53] K. Amezawa, H. Maekawa, Y. Tomii and N. Yamamoto, *Solid State Ionics,* 145 (2001), p. 233
[54] N. Kitamura, K. Amezawa, Y. Tomii and N. Yamamoto, *Solid State Ionics,* 162-163 (2003), p. 161
[55] N. Kitamura, K. Amezawa, Y. Tomii, T. Hanada, N. Yamamoto, T. Omata and S. Otsuko-Yao-Matsuo, *Journal of the Electrochemical Society,* 152 (2005), p. A658
[56] K. Amezawa, Y. Kitajima, Y. Tomii, N. Yamamoto, M. Widerøe and T. Norby, *Solid State Ionics,* 176 (2005), p. 2867
[57] K. Amezawa, Y. Uchimoto and Y. Tomii, *Solid State Ionics,* 177 (2006), p. 2407
[58] R. Haugsrud and T. Norby, *Solid State Ionics,* 177 (2006), p. 1129
[59] R. Haugsrud and T. Norby, *Nature Materials,* 5 (2006), p. 193
[60] F. Schönberger, E. Kendrick, M. S. Islam and P. R. Slater, *Solid State Ionics,* 176 (2005), p. 2951
[61] E. Kendrick, J. Kendrick, K. S. Knight, M. S. Islam and P. R. Slater, *Nature Materials,* 6 (2007), p. 871
[62] Ph. Colomban, Ed., *Proton Conductors: Solids, membranes and gels – materials and devices,* Cambridge University Press, Cambridge, UK, 1992
[63] H. Iwahara, in the Proceedings of the 17th Risø International Symposium on Materials Science, Risø, Denmark, 1996
[64] K. D. Kreuer, *Chemistry of Materials,* 8 (1996), p. 610
[65] K. D. Kreuer, *Solid State Ionics,* 97 (1997), p. 1
[66] T. Norby and Y. Larring, *Current Opinion in Solid State & Materials Science,* 2 (1997), p. 593
[67] K. D. Kreuer, *Annual Review of Materials Science,* 33 (2003), p. 333
[68] T. Norby, M. Widerøe, R. Glöckner and Y. Larring, *Dalton Transactions,* 19 (2004), p. 3012
[69] L. Malavasi, C. A. J. Fisher and M. S. Islam, *Chemical Society Reviews,* 39 (2010), p. 4370
[70] E. Fabbri, D. Pergolesi and E. Traversa, *Chemical Society Reviews,* 39 (2010), p. 4355
[71] T. Schober and H. G. Bohn, *Solid State Ionics,* 127 (2000), p. 351
[72] K. S. Knight and N. Bonanos, *Materials Research Bulletin,* 30 (1995), p. 347
[73] K. S. Knight, *Solid State Ionics,* 145 (2001), p. 275
[74] W. Münch, K. D. Kreuer, S. Adams, G. Seifert and J. Maier, *Phase Transitions,* 68 (1999), p. 567
[75] T. Shimura, K. Suzuki and H. Iwahara, *Solid State Ionics,* 113-115 (2008), p. 355
[76] V. V. Kharton, A. P. Viskup, E. N. Naumovich and F. M. B. Marques, *Journal of Materials Chemistry,* 9 (1999), p. 2623
[77] V. V. Kharton, A. P. Viskup, A. V. Kovalevsky, E. N. Naumovich and F. M. B. Marques, *Solid State Ionics,* 143 (2001), p. 337
[78] C. Chatzichristodoulou, Defect chemistry, thermomechanical and transport properties of mixed oxide-ionic and electronic conductors for application in oxygen permeation membranes, PhD thesis, University of Copenhagen, Copenhagen, Denmark, 2009
[79] J. B. Goodenough, A. Manthiram and J. F. Kuo, *Materials Chemistry and Physics,* 35 (1993), p. 221
[80] G. B. Zhang and D. M. Smyth, *Solid State Ionics,* 82 (1995), p. 153
[81] C. A. J. Fisher and M. S. Islam, *Solid State Ionics,* 118 (1999), p. 355
[82] T. Shimura, M. Komori and H. Iwahara, *Solid State Ionics,* 86-88 (1996), p. 685
[83] J. A. Labrincha, J. R. Frade and F. M. B. Marques, *Solid State Ionics,* 99 (1997), p. 33
[84] T. Omata, K. Ikeda, R. Tokashiki and S. Otsuko-Yao-Matsuo, *Solid State Ionics,* 167 (2004), p. 389

[85] M. E. Björketun, C. S. Knee, J. B. Nyman and G. Wahnström, *Solid State Ionics,* 178 (2008), p. 1642
[86] K. E. J. Eurenius, E. Ahlberg, I. Ahmed, S. G. Eriksson and C. S. Knee, *Solid State Ionics,* 181 (2010), p. 148
[87] K. E. J. Eurenius, E. Ahlberg and C. S. Knee, *Solid State Ionics,* 181 (2010), p. 1258
[88] K. E. J. Eurenius, E. Ahlberg and C. S. Knee, *Solid State Ionics,* 181 (2010), p. 1577
[89] D. M. Giaquinta and H.-C. zur Loye, *Chem. Mater.* 6 (1994), p. 365
[90] V. W. Goldschmidt, *J. Math. Naturvid. Klass.,* 2 (1926), p. 97
[91] C. Li, K. C. Soh and P. Wu, *Journal of Alloys and Compounds,* 372 (2004), p. 40
[92] Yu. V. Kabirov, M. F. Kupriyanov and E. V. Chebanova, *Journal of Structural Chemistry*, 50 (2009) p. 470
[93] P. Kofstad and T. Norby, Defects and Transport in Crystalline Solids, Oslo, 2009
[94] T. Schober and H. Wenzl, *Ionics,* 1 (1995), p. 311
[95] T. Schober, W. Schilling and H. Wenzl, *Solid State Ionics,* 86-88 (1996), p. 653
[96] N. Bonanos and F. W. Poulsen, *Journal of Materials Chemistry,* 9 (1999), p. 431
[97] F. W. Poulsen, *Journal of Solid State Chemistry,* 143 (1999), p. 115
[98] N. Bonanos, *Solid State Ionics,* 145 (2001), p. 265
[99] F. W. Poulsen, *Methods and Limitations in Defect Chemistry Modelling,* Fuel Cells and Solid State Department, Risø – DTU (2007)
[100] N. Bork, N. Bonanos, J. Rossmeisl and T. Vegge, Ab initio Charge Analysis of Pure and Hydrogenated Perovskites, Submitted to Journal of Applied Physics
[101] F. W. Poulsen, *Solid State Ionics,* 145 (2001), p. 387
[102] T. Norby and R. Haugsrud, in *Nonporous Inorganic Membranes,* A. F. Sammels and M. V. Mundschau (Ed), 1st Ed., Ch. 1, Wiley-VCH, 2006
[103] T. Norby and R. Haugsrud, *Solid State Ionics,* 136-137 (2000), p. 139
[104] N. Fukatsu and N. Kurita, *Ionics,* 11 (2005), p. 54
[105] Y. S. Lin, X. Qi, M. Pan and G. Meng, *Ionics,* 4 (1998), p. 444
[106] K. D. Kreuer, M. Schuster, S. J. Paddison and E. Spohr, *Chemical Reviews,* 104 (2004), p. 4637
[107] F. Lefebvre-Joud, G. Gauthier and J. Mougin, *Journal of Applied Electrochemistry,* 39 (2009), p. 535
[108] J. Hartvigsen, S. Elangovan and A. Khandkar, *A Comparison of Proton and Oxygen Ion Conducting Electrolytes for Fuel Cell Applications*, Presented at AIChE Annual Meeting Fuel Cells for Utility Applications and Transportation: Engineering and Design II, 1993
[109] P. A. Stuart, J. A. Kilner, S. J. Skinner and T. Unno, *Solid State Ionics,* 179 (2008), p. 1120
[110] C. A. Scholes, K. H. Smith, S. E. Kentish and G. W. Stevens, *International Journal of Greenhouse Gas Control,* 4 (2010), p. 739
[111] U. Balachandran, B. Ma, T. H. Lee, S. J. Song, L. Chen and S. E. Dorris, *Materials Research Society Symposium Proceedings,* 972 (2007), p. 3
[112] J. A. Ritter and A. D. Ebner, *Separation Science and Technology,* 42 (2007), p. 1123
[113] V. V. Latyshev, *Atomic Energy,* 68 (1990), p. 49, translated from *Atomnaya Énergiya,* 68 (1990), p. 38
[114] D. K. Ross, *Journal of The Less-Common Metals,* 89 (1983), p. 407
[115] V. Violante, A. Basile and E. Drioli, *Fusion Engineering and Design,* 22 (1993), p. 257
[116] C. Athanassiou, G. Pekridis, N. Kaklidis, K. Kalimeri, S. Vartzoka and G. Marnellos, *International Journal of Hydrogen Energy,* 32 (2007), p. 38
[117] T. Hibino, S. Hamakawa and H. Iwahara, *Chemistry Letters,* 9 (1992), p. 1715
[118] S. Hamakawa, T. Hibino and H. Iwahara, *Journal of the Electrochemical Society,* 140 (1993), p. 459
[119] M. Nagao, T. Yoshii, T. Hibino, M. Sano and A. Tomita, *Electrochemical and Solid-State Letters,* 9 (2006), p. J1
[120] K. K. Kalimera, C. I. Athanasiou and G. E. Marnellos, *Solid State Ionics,* 181 (2010), p. 223
[121] United States Department of Energy, Small Business Innovation Research Program and Small Business Technology Transfer Program FY 2005 Solicitations, Technical Topic Descriptions, 15. Materials Research, Office of Fossil Energy, 2005, http://www.science.doe.gov/sbir/solicitations/fy 2005/15_FE3.htm
[122] *Hydrogen From Coal Program*; Office of Fossil Energy, U.S. Department of Energy, Washington DC, 2005
[123] J. W. Phair and R. Donelson, *Industrial and Engineering Chemistry Research,* 45 (2006), p. 5657
[124] H. Uchida, A. Yasuda and H. Iwahara, *Denki Kagaku,* 57 (1989), p. 153

[125] M. J. Scholten, J. Schoonman, J. C. van Miltenburg and H. A. J. Oonk, *Solid State Ionics,* 61 (1993), p. 83
[126] K. H. Ryu and S. M. Haile, *Solid State Ionics,* 125 (1999), p. 355
[127] N. Zakowsky, S. Williamson and J. T. S. Irvine, *Solid State Ionics,* 176 (2005), p. 3019
[128] J. W. Phair and S. P. S. Badwal, *Science and Technology of Advanced Materials,* 7 (2006), p. 792
[129] T. L. Ward and T. Dao, *Journal of Membrane Science,* 153 (1999), p. 211
[130] P. L. Andrew and A. A. Haasz, *Journal of Applied Physics,* 72 (1992), p. 2749
[131] S. N. Paglieri, in *Nonporous Inorganic Membranes,* A. F. Sammels and M. V. Mundschau (Ed), 1st Ed., Ch. 1, Wiley-VCH, 2006
[132] S. Uemiya, *Membrane,* 30 (2005), p. 13
[133] H. Suda, *Membrane,* 31 (2006), p. 267
[134] J. Caro, M. Noack, P. Kölsch and R. Schäfer, *Microporous and Mesoporous Materials,* 38 (2000), p. 3
[135] N. Tanihara, H. Shimazaki, Y. Hirayama, S. Nakanishi, T.Yoshinaga, Y. Kusuki, *Journal of Membrane Science,*. 160 (1999) p. 179
[136] M. Freemantle, *Chemical Engineering News,* 83 (2005), p. 49
[137] E. Barsoukov and J. R. Macdonald (ed.) *Impedance Spectroscoy,* 2nd Edition, John Wiley & Sons, Inc. Hoboken, NJ, USA, 2005
[138] M. E. Orazem and B. Tribollet, *Electrochemical Impedance Spectroscopy,* John Wiley & Sons, Inc., Hoboken, NJ, USA, 2008
[139] J. Jamnik and J. Maier, *Journal of the Electrochemical Society,* 146 (1999), p. 4183
[140] W. Lai and S. M. Haile, *Journal of the American Ceramic Society,* 88 (2005), p. 2979
[141] www.echemsw.com
[142] T. van Dijk and A. J. Burggraaf, *Physica Status Solidi A,* 63 (1981), p. 229
[143] M. J. Verkerk, B. J. Middelhuis and A. J. Burggraaf, *Solid State Ionics,* 6 (1982), p. 159
[144] J. Fleig and J. Maie7r, *Journal of the Electrochemical Society,* 145 (1998), p. 2081
[145] A. Patterson, *Physical Review*, 56 (1939), p. 978
[146] D. A. G. Bruggeman, *Annalen der Physik,* 24 (1935), p. 636
[147] R. D. Shannon, *Acta Crystallographica,* A32 (1976), p. 751
[148] L. Pauling, *Journal of the American Chemical Society,* 54 (1932), p. 3570
[149] N. Ito and H. Matsumoto, *Proton conducting electrolyte and electrochemical cell includinc proton conducting electrolyte,* US patent application no. 20080241681 A1, October 2nd, 2008
[150] C. K. Vigen, *Transport og defekter I akseptordopet $LaScO_3$ og $LaMg_{0,5}Ti_{0,5}O_3$,* Master thesis, University of Oslo, Oslo, Norway, 2009
[151] D. Lybye and N. Bonanos, *Solid State Ionics,* 125 (1999), p. 339
[152] C. Hatchwell, N. Bonanos and M. Mogensen, *Solid State Ionics,* 167 (2004), p. 349
[153] K. Nomura, T. Takeuchi, S. I. Kamo, H. Kageyama and Y. Miyazaki, *Solid State Ionics,* 175 (2004), p. 553
[154] R. Roy, *Journal of the American Ceramic Society,* 37 (1954), p. 581
[155] A. Meden and M. Čeh, *Materials Science Forum¸* 278-281 (1998), p. 773
[156] D. Y. Lee, S. J. Yoon, J. H. Yeo, S. Nahm, J. H. Paik, K. C. Whang and B. G. Ahn, *Journal of Materials Science Letters,* 19 (2000), p. 131
[157] M. P. Seabra, M. Avdeev, V. M. Ferrerira, R. C. Pullar and N. McN. Alford, *Journal of the European Ceramic Society,* 23 (2003), p. 2403
[158] I. Levin, T. A. Vanderah, T. G. Amos and J. E. Maslar, *Chemistry of Materials,* 17 (2005), p. 3273
[159] A. N. Salak, O. Prokhnenko and V. M. Ferreira, *Journal of Physics: Condensed Matter,* 20 (2008), p. 1
[160] Z. Chaogui, W. Shuangyan, L. Fuhui, T. Shujian and L. Guobao, *Journal of Alloys and Compounds,* 289 (1999), p. 257
[161] P. Babilo and S. M. Haile, *Journal of the American Ceramic Society,* 88 (2005), p. 2362
[162] S. Tao and J. T. S. Irvine, *Journal of Solid State Chemistry,* 180 (2007), p. 3493
[163] J. S. Park, J. H. Lee, H. W. Lee and B. K. Kim, *Solid State Ionics,* 181 (2010), p. 163
[164] R. Costa, N. Grünbaum, M. H. Berger, L. Dessemond and A. Thorel, *Solid State Ionics, Diffusion & Rections,* 180 (2009), p. 891
[165] E. Gorbova, V. Maragou, D. Medvedev, A. Demin and P.Tsiakaras, *Solid State Ionics,* 179 (2008), p. 887

[166] S. J. Song, T. H. Lee, E. D. Wachsman, L. Chen, S. E. Dorris and U. Balachandran, *Journal of the Electrochemical Society,* 152 (2005), p. J125
[167] U. Balachandran, T. H. Lee, L. Chen, S. J. Song, J. J. Picciolo and S. E. Dorris, *Fuel,* 85 (2006), p. 150
[168] M. James and J. P. Attfield, *Journal of Solid State Chemistry,* 105 (1993), p. 287
[169] M. James and J. P. Attfield, *Chemistry of Materials,* 7 (1995), p. 2338
[170] M. James, J. P. Attfield and J. Rodriguez-Carvajal, *Chemistry of Materials,* 7 (1995), p. 1448
[171] M. Greenblatt, *Current Opinion in Solid State & Materials Science,* 2 (1997), p. 174
[172] V. P. Gorelov, *Elektrokhimiya*, 24 (1988), p. 1380
[173] M. Liu and H. Hu, *Journal of the Electrochemical Society*, 143 (1996), p. L109
[174] V. V. Kharton and F. M. B. Marques, *Solid State Ionics,* 140 (2001), p. 381
[175] J. R. Frade, V. V. Kharton, A. A. Yaremchenko and E. V. Tsipis, *Journal of Solid State Electrochemistry,* 10 (2006), p. 96
[176] A. R. Potter and R. T. Baker, *Solid State Ionics,* 177 (2006), p. 1917
[177] T. Norby, *Solid State Ionics,* 28-30 (1988), p. 1586
[178] D. P. Sutija, T. Norby and P. Björnbom, *Solid State Ionics*, 77 (1995), p. 167
[179] H.-I. Yoo and M. Martin, *Physical Chemistry Chemical Physics*, 12 (2010), p. 14699
[180] J.-H. Yu, J.-S. Lee and J. Maier, *Solid State Ionics,* 181 (2010), p. 154
[181] H.-I. Yoo and C.-E. Lee, *Solid State Ionics,* (2009), p. 326-337
[182] J. I. Yeon and H.-I. Yoo, *Solid State Ionics,* 181 (2010), p. 1323
[183] A. S. Nowick and A. V. Vaysleyb, *Solid State Ionics,* 97 (1997), p. 17
[184] E. Matsushita and T. Sasaki, *Solid State Ionics,* 125 (1999), p. 31
[185] V. I. Tsidilkovski, *Solid State Ionics,* 162-163 (2003), p. 47
[186] H. Matsumoto, K. Takeuchi and H. Iwahara, *Journal of the Electrochemical Society,* 146 (1999), p. 1486
[187] H. Matsumoto, K. Takeuchi and H. Iwahara, *Solid State Ionics,* 125 (1999), p. 377
[188] H. Matsumoto, H. Hayashi and H. Iwahara, *Journal of Nuclear Science and Technology,* 39 (2002), p. 367
[189] H. Matsumoto, H. Hayashi, T. Shimura, K. Amezawa, T. Otake, K. Yashiro, Y. Nigara, A. Kaimai, T. Kawada, H. Iwahara and J. Mizusaki, *Solid State Ionics,* 175 (2004), p. 491
[190] M.W. Chase, C.A. Davies, J.R. Downey, D.J. Frurip, R.A. McDonald, A.N. Syverud, *JANAF thermochemical tables. Vol. 1-2*, 3rd ed., New York, American Institute of Physics Inc. (1985)
[191] Datasheet for Inficon (formerly Agilent) 3000 Micro GC, http://www.inficon.com/download/en/Datasheet%20-%203000%20Micro%20GC.pdf, accessed Nov 4th 2010
[192] G. B. Kaufmann, J. J. Thurner and D. A. Zatko, *Ammonium Hexachloroplatinate(IV)*, in *Inorganic Syntheses, Vol. 9* (ed. S. E. Tyree), John Wiley & Sons, Inc., Hoboken, NJ, USA
[193] A. E. Schweizer and G. T. Kerr, *Inorganic Chemistry,* 17 (1978) p. 2326
[194] B. Dalslet, P. Blennow, P. V. Hendriksen, N. Bonanos, D. Lybye and M. Mogensen, *Journal of Solid State Electrochemistry,* 10 (2006), p. 547
[195] S. Cheng, V. K. Gupta and J. Y. S. Lin, *Solid State Ionics,* 176 (2005), p. 2653
[196] R. Morrell, Handbook of Properties of Technical and Engineering Ceramics, Part 2, 1987
[197] Smithells Metals Reference Book, 7th Ed. Edited by E. A. Brandes and G. B. Brook, Butterworth and Henemann, 1992
[198] M. D. Dolan, *Journal of Membrane Science,* 362 (2010), p. 12
[199] H. Matsumoto, T. Shimura, T. Higuchi, H. Tanaka, K. Katahira, T. Otake, T. Kudo, K. Yashiro, A. Kaimai, T. Kawada and J. Mizusaki, *Journal of the Electrochemical Society,* 152 (2005), p. A488
[200] A. Unemoto, A. Kaimai, K. Sato, K. Yashiro, H. Matsumoto, J. Mizusaki, K. Amezawa and T. Kawada, *Solid State Ionics,* 178 (2008), p. 1663

Paper I

Solid State Ionics xxx (2009) xxx–xxx

Contents lists available at ScienceDirect

Solid State Ionics

journal homepage: www.elsevier.com/locate/ssi

EMF measurements on mixed protonic/electronic conductors for hydrogen membrane applications

Henrik K. Bentzer *, Nikolaos Bonanos, John W. Phair

Department for Fuel Cells and Solid State Chemistry, Risø National Laboratory for Sustainable Energy, Technical University of Denmark, PO Box 49, DK-4000, Roskilde, Denmark

ARTICLE INFO

Article history:
Received 20 August 2008
Received in revised form 1 July 2009
Accepted 2 November 2009
Available online xxxx

Keywords:
EMF
Proton conductors
Mixed conductors
Strontium cerate

ABSTRACT

Electromotive force (EMF) measurements are often used to estimate the transport number of conducting species in ionic and mixed conductors. In this work, the applicability of the method to systems, where both protonic, oxide-ionic and electronic conduction is significant, was examined. The effect of electrode polarisation resistance, water vapour concentration and impurities was analysed. Samples of $SrCe_{0.95}Y_{0.05}O_{3-\delta}$ were prepared and used in a number of EMF measurements, including wet and dry hydrogen and oxygen concentration cells. It was found that concentration cells including water vapour gave large errors in the determination of the oxide-ionic transport number, but gave good estimates of the protonic transport number. The protonic transport number was estimated to around 0.80 at 600 °C, decreasing to around 0.65 at 800 °C, consistent with previous investigations on similar materials.

1. Introduction

In ceramic high temperature proton conductors, the transport numbers for protons, electrons and oxide-ions are of great interest, since they govern the materials' applicability in various devices. For sensor and fuel cell applications, the protonic transport number should be as close as possible to unity. Whereas for hydrogen membrane applications, it should be close to a value of one half, with electronic conduction making up the remainder. In the oxide based proton conductors, where the protonic defects are formed by interaction of a hydrogen- containing gas and oxygen vacancies in the lattice, oxide ion conductivity may also be present. Higher temperature is expected to increase oxide ion conductivity at the cost of protonic, due to the exothermic nature of proton defect creation. In such cases, oxide-ions present a third conduction path, and another transport number to be determined.

Three common ways to determine transport numbers are faradaic efficiency measurements [1–3], the Hebb–Wagner technique [4,5] and electromotive force (EMF) measurements, the last of which will be investigated here. Often, EMF measurements are used to determine a single ionic transport number in a material, and the rest of the conductivity is assumed to be electronic. Use of methods to correct for electrode polarization resistance is not widespread, and to our knowledge has not been applied to systems where both oxide-ionic and protonic transport numbers are significant. In this work, the possibilities for using the EMF method to measure both protonic and a minor oxide-ionic transport numbers at high and low oxygen partial pressure, as well as using well known methods for correcting for electrode irreversibility in such systems has been explored, using the well known high temperature proton conductor $SrCe_{0.95}Y_{0.05}O_3$. The material was chosen on basis of its reasonable electronic conductivity and well known defect chemistry, which predicts possible oxide ion conductivity at high temperature. These factors make it a good material for investigating EMF measurements on systems with three conduction paths.

2. Background

2.1. Determination of transport numbers via EMF measurements

The electromotive force technique is based on open cell voltage measurements on a sample equipped with two reversible electrodes and subjected to a gradient in chemical potential. The equations for calculating the voltage developed over an oxide-ion conducting sample of a binary compound were first derived by Wagner [6].

For an ionic or mixed conductor subjected to a gradient in chemical potential of the ionic species i, the EMF may be defined as:

$$E_{EMF} = -\int_{\mu_1}^{\mu_2} \frac{t_i}{nF} d\mu_i \quad (1)$$

or if the gradient is in a gaseous species

$$E_{EMF} = -RT\int_{p_1}^{p_2} \frac{t_i}{nF} d\ln p_i \quad (2)$$

where t_i is the transport number for species i, n the number of electrons transferred, F Faraday's constant, R the universal gas constant and T the temperature. μ_1 and μ_2 are the chemical potential of species

* Corresponding author. Tel.: +45 4677 5669.
E-mail address: henrik.bentzer@risoe.dk (H.K. Bentzer).

0167-2738/$ – see front matter © 2009 Elsevier B.V. All rights reserved.
doi:10.1016/j.ssi.2009.11.002

i at either end of the gradient, with p_1 and p_2 the corresponding partial pressures of the active gas in the inner and outer compartment of an EMF setup. If the gradient is small, an average transport number can be used, and the integrated equation simplifies to:

$$E_{\mathrm{EMF}} = -\frac{RT}{nF} t_i \ln\frac{p_2}{p_1} \tag{3}$$

while the theoretical voltage calculated from the Nernst equation is:

$$E_{\mathrm{Nernst}} = -\frac{RT}{nF} \ln\frac{p_2}{p_1} \tag{4}$$

The average transport number can be calculated as the ratio between measured and theoretical voltages:

$$t_{\mathrm{avg}} = \frac{E_{\mathrm{EMF}}}{E_{\mathrm{Nernst}}} \tag{5}$$

The transport number thus found is the total transport number for mobile ions in the compound [7]. In ternary or higher oxides where the cation mobility is significant, the transport number for a given charge carrier cannot uniquely be defined from the EMF measurements due to the extra degrees of freedom. Transport number determinations of constituent ions are thus only possible for oxides where one of the ions is significantly more mobile than any other, or where different gradients can be applied for the different mobile species. In the following, it is assumed that the mobility of cations other than H^+ is negligible.

The expansion of the original Wagner theory for oxides to include proton transport has been covered previously [8,9]. It was shown that the voltages created by gradients in different species are additive. Thus, for an oxide material showing conductivity of both native oxide-ions and protons, the EMF developed can be expressed as

$$E_{\mathrm{th}} = \frac{RT}{4F}(t_{\mathrm{O}}) \ln\frac{p^2_{\mathrm{O}_2}}{p^1_{\mathrm{O}_2}} - \frac{RT}{2F}(t_{\mathrm{H}}) \ln\frac{p^2_{\mathrm{H}_2}}{p^1_{\mathrm{H}_2}} \tag{6}$$

where t_{O} and t_{H} are transport numbers for oxide-ions and protons, and the ps signify the partial pressure of the respective gasses in the inner and outer compartments.

While other studies have included hydroxide, hydride and hydronium ions as conducting species in high temperature hydrogen transport in oxides, in this work the mobile hydrogen species will be assumed to be protons, ignoring other hydrogen species [10–12]. The protons will always exist in the electron cloud of a lattice oxygen, forming a hydroxide on an oxide-ion site, and are denoted as $OH^{\bullet}_{O}$ using Kröger–Vink notation.

In EMF measurements on systems where protons or oxide-ions might be one of the conducting species, the equilibrium between hydrogen, oxygen and water vapour needs to be taken into account. Even more so in systems where both charge carriers might be relevant.

$$^1/_2\,O_2 + H_2 \rightleftharpoons H_2O \tag{7}$$

$$K = \frac{p_{\mathrm{H_2O}}}{p_{\mathrm{H_2}}\sqrt{p_{\mathrm{O_2}}}} \tag{8}$$

Using this, the equation for calculating the EMF can be rewritten as

$$E_{\mathrm{th}} = \frac{RT}{4F}(t_{\mathrm{O}} + t_{\mathrm{H}}) \ln\frac{p^2_{\mathrm{O}_2}}{p^1_{\mathrm{O}_2}} - \frac{RT}{2F}(t_{\mathrm{H}}) \ln\frac{p^2_{\mathrm{H_2O}}}{p^1_{\mathrm{H_2O}}} \tag{9}$$

or

$$E_{\mathrm{th}} = \frac{RT}{2F}(t_{\mathrm{O}}) \ln\frac{p^2_{\mathrm{H_2O}}}{p^1_{\mathrm{H_2O}}} - \frac{RT}{2F}(t_{\mathrm{O}} + t_{\mathrm{H}}) \ln\frac{p^2_{\mathrm{H}_2}}{p^1_{\mathrm{H}_2}} \tag{10}$$

The equation used depends on the experimental setup, as discussed below. These expressions illustrate the importance of controlling and monitoring the water vapour pressure in EMF experiments on proton conducting oxides. It also gives the possibility for designing experiments for determining transport numbers for protons and oxide-ions at both high oxygen partial pressures (oxygen/nitrogen mixtures) and low ones (hydrogen/nitrogen).

As described by Sutija et al. [9], it is possible to set up a gradient in hydrogen while keeping the oxygen gradient negligible using the equilibrium in Eq. (7). Equal partial pressures of oxygen and inert gas are set in both cell compartments. The water vapour partial pressure is held constant in the outer compartment and varied in the inner. This allows t_{H} to be determined under oxidising wet conditions. To measure t_H at low $p_{\mathrm{O_2}}$, a gradient in hydrogen should be set up in either dry or wet conditions. As long as the hydrogen and water vapour partial pressures are varied in the same manner, and their ratio kept constant, no oxygen gradient will be introduced [9]. An experiment to verify the validity of the lack of a $p_{\mathrm{O_2}}$ gradient in the wet experiment was performed and the results are reported in this paper.

A gradient in dry oxygen gas will give the oxide ion transport number under dry oxidising conditions. Under wet reducing conditions, varying the water vapour partial pressure while keeping the hydrogen partial pressure fixed will induce an oxygen gradient similarly to the hydrogen case. However, a wet measurement at high $p_{\mathrm{O_2}}$ is hard to construct, since the hydrogen concentration is not proportional to the ratio between water vapour and oxygen partial pressures.

Thus, a full determination of all transport numbers at all $p_{\mathrm{O_2}}$–$p_{\mathrm{H_2O}}$ combinations is not possible using EMF measurements. In this work, it is shown that with proper experimental setup coupled with understanding of the defect chemistry of the material under examination, EMF measurements will give a good picture of the transport numbers under varied conditions.

2.2. Correction for polarisation resistance

The problem of irreversible electrodes and methods for correcting for the error are well known [13–16]. The problem occurs because Wagner theory only takes into account the electronic and ionic resistivities of the sample and treats them as ideal resistors connected in parallel. It does not take into account the polarisation resistance, R_η of the electrodes. The case most commonly treated in the literature is that where only one ionic conductivity component is significant [13]. An equivalent circuit for this situation is shown in Fig. 1. R_{o} and R_{e} are the electronic and oxide-ionic resistances, while E_{o} is the Nernstian voltage created by the oxygen gradient. The model is intended to describe voltage measurements across the sample, but is not valid for calculating potentials and currents at any given point inside the sample.

The current flowing through this cell is [14]

$$I = \frac{E_{\mathrm{Nernst}} - \eta}{R_{\mathrm{O}} + R_{\mathrm{e}}} \tag{11}$$

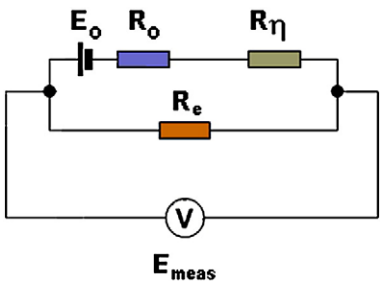

Fig. 1. Equivalent circuit for a mixed oxide-ion/electron conductor, adapted from [13].

Please cite this article as: H.K. Bentzer, et al., Solid State Ion. (2009), doi:10.1016/j.ssi.2009.11.002

where η is the total electrode overpotential, which is assumed to be in the linear regime, that is

$$\eta = IR_\eta \tag{12}$$

Under these conditions, it can then be shown that the ratio between observed voltage, E_{obs} and the voltage calculated from the Nernst equation, E_{Nernst} is given by

$$\frac{E_{obs}}{E_{Nernst}} = t_O\left(1 + \frac{R_\eta}{R_O + R_e}\right)^{-1} \tag{13}$$

which simplifies to the Wagner equation when $R_\eta << (R_i + R_e)$. Failure to take significant polarisation resistance into account will lead to underestimation of the ionic transport number when using the EMF technique. The relative error induced by not taking the polarisation resistance into account has been calculated for an oxide ion conductor elsewhere [13].

Two different methods can be applied to correct for electrode polarisation resistance. Both involve an AC conductivity measurement to determine the total (bulk) resistance of the sample. The final measurement can then be the active load method to where R_e is determined directly [14,16], or a low frequency impedance measurement, which will directly give the total resistance of sample plus electrodes [15]. Using the latter method, the corrected transport number can be calculated using the equation

$$t_i = 1 - \frac{R_b}{R_T}\left(1 - \frac{E_{obs}}{E_{Nernst}}\right) \tag{14}$$

where R_b and R_T are sample and total resistances, that is, the high and low frequency real axis intercepts of the impedance curve.

If there is reason to believe that the polarisation resistance varies significantly over measurement range of gradients, the impedance analysis method is preferable, since the active load approach cannot be applied in case of no gradient. While Eq. (14) obviously cannot be applied directly when E_{Nernst} is zero either, the relative size of R_b and R_T can be found under any conditions and their variation with gradient analysed. At low temperatures or low concentrations of electroactive gas species, the active load method is often preferable. Under such conditions, electrode polarisation resistance is expected to be large, and finding the low frequency intercept in the impedance plot will require either very low frequency data, or extrapolation of higher frequency data.

As the temperature is increased, the concentration of protons in the sample is expected to decrease and the concentration of oxygen vacancies to increase. Depending on the mobility of the ions, many oxide materials will therefore potentially have a temperature- and p_{O_2}-range where both ionic conductivities are significant. If one attempts to apply the methods for correcting for electrode polarisation described above to a material with both native ionic conductivity and a foreign species such as protons in an oxide, another Nernstian voltage, ionic resistance and polarisation resistance need to be introduced in parallel to the initial one, as shown in Fig. 2. Again, the circuit is only intended to visualise the voltage measurement across the sample, and is not valid for points inside the sample.

According to Millman's theorem [17], the measured voltage under these conditions will be

$$E_{obs} = \frac{\frac{E_O}{R_O + R_{\eta O}} + \frac{E_H}{R_H + R_{\eta H}}}{\frac{1}{R_O + R_{\eta O}} + \frac{1}{R_H + R_{\eta H}} + \frac{1}{R_e}} \tag{15}$$

As mentioned, the voltages are additive, and

$$E_{Nernst} = E_O + E_H \tag{16}$$

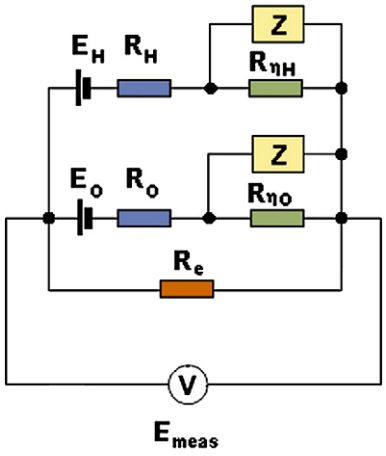

Fig. 2. Equivalent circuit for an EMF measurement setup on a material with both oxide-ion and proton conductivity.

Unfortunately, the ratio E_{obs}/E_{Nernst} does not reduce to a simple transport number and correction factor as is the case in Eq. (12). This severely limits the usability of Eq. (13). The active load method for electrode polarisation correction cannot be used since the necessary equations are invalid, and no simple linear response will be found in this system. The impedance spectroscopy method can only be used if all five resistances can be found using a mixture of EMF and impedance measurements. If the electronic conductivity is negligible and the two polarisation resistances can be properly resolved, all terms in Eq. (13) can be found. This, however, requires good knowledge of the electrode material under the conditions applied, and might be problematic even then. The amount of measurements needed to reliably determine all resistances in Eq. (13), and the possible errors in interpreting the results means that it will often be less time consuming to set up experiments to reduce the number of significant factors instead of trying to get all terms in Eq. (13). For example, electrode materials can be used which are highly reversible to one species, but irreversible to the other, effectively shutting off one branch in the equivalent circuit. The extreme of this approach is the Hebb–Wagner experiment, where a completely blocking electrode is employed.

2.3. The effect of impurities and unintended gradients

In any EMF setup, the effect of impurities must be taken into account. Any amount, however slight, of reducing or oxidising species in the inert gas employed must be known, and water vapour content carefully controlled and monitored. The effect of impurities is naturally greater the smaller the concentration of the active species. Electrode irreversibility to hydrogen but not to water vapour, may result in unintended gradients in oxygen [18].

Protons can be incorporated into the material from any gas containing hydrogen, including water. Eq. (17) shows the oxidation of hydrogen creating two protons and two electrons, while Eq. (18) shows proton creation by incorporation of water vapour.

$$H_2 + 2O_O^x \rightleftharpoons 2OH_O^\bullet + 2e^- \tag{17}$$

$$H_2O + V_O^{\bullet\bullet} + O_O^x \rightleftharpoons 2OH_O^\bullet \tag{18}$$

Water can be transported through the membrane via ambipolar transport of oxygen vacancies and protons, and although a water vapour gradient will not on its own lead to an EMF, net transport of water through the membrane can result in unwanted gradients. While their effects might be hard to control, it is important to review the experimental setup to see whether such errors might influence the results.

Please cite this article as: H.K. Bentzer, et al., Solid State Ion. (2009), doi:10.1016/j.ssi.2009.11.002

Problems of controlling transport through the sample, coupled with the possible problems with electrode polarisation resistances in systems with multiple conductivities, mean that it will not be possible to fully determine all transport numbers under all conditions using the technique.

3. Experimental

$SrCe_{0.95}Y_{0.05}O_{2.975}$ was produced using a solid state reaction technique detailed elsewhere [19]. Since the powder had been aged, it was heat-treated at 800 °C for 8 h prior to use. X-ray powder diffraction showed no signs of carbonates, hydroxides or other impurities. The powder was ball-milled for 12 h in ethanol using zirconia balls. The resulting slurry was sieved through a nylon cloth with 37 µm openings (~400 mesh), dried and crushed. The fine fraction was used for samples, while the coarse fraction was used as sacrificial powder during sintering. The powder was pressed uniaxially into pellet shape using an 18 mm diameter die at 60 MPa. The pellets were then isostatically pressed at 325 MPa in evacuated latex containers and sintered in air at 1450 °C for 12 h. Two pellets were selected for measurements; one was only lightly polished and had a thickness of 2.3 mm, the other ground down to 0.84 mm thickness before polishing. Both samples had a density of over 95% after polishing.

For electrochemical measurements, the samples were equipped with platinum electrodes on both sides by attaching a 10 mm diameter platinum mesh with a layer of platinum paste, drying and then firing at 1000 °C for 2 h.

The measurement rig consists of an alumina tube to which the sample is attached using a gold seal and a smaller inner spring-loaded tube containing a platinum lead for the inside electrode and thermocouple and through which gas is supplied, see Fig. 3. The sample is held in place by an alumina hood secured with spring-loaded kanthal wires. It is attached using a gold seal, heating up to 1000 °C in the test furnace and then slowly cooling to the measurement temperature. The rig is inserted into a tubular furnace which also functions as the outer gas compartment.

Gas to the inner and outer compartments was supplied through stainless steel tubes from a mixer setup allowing any composition $N_2/H_2/H_2O$ or $N_2/O_2/H_2O$ to be used on either side. Bubbling the dry gas through H_2O flasks and mixing the moisturised gas with dry gas allowed control of the water content of the gas. The water vapour concentration was measured using a *Dewlux* moisture meter (MCM Ltd, Wetherby, UK), with analog output. Impedance spectra were recorded using a *Solartron SI 1260* frequency analyser (Solartron Analytical, Hampshire, UK). An amplitude of 0.03 V was used without dc bias, in the frequency range 0.05 Hz–1 MHz. The fitting and analysis was performed using *ZSimpWin* 3.21 (EChem Software) [20].

EMF measurements were performed at 600 and 800 °C. At both temperatures, a series of wet experiments performed at both high and low p_{O_2} as outlined in Table 1. For all experiments, gradients of $p_{II}/p_I = 1$, 0.8, 0.5, 0.2, 0.1, 0.05 and 0.02 of the active species were used. It is likely that the larger gradients are so large that the assumption that an average transport number can be used still holds. They were still included in the interest of exploring the method further.

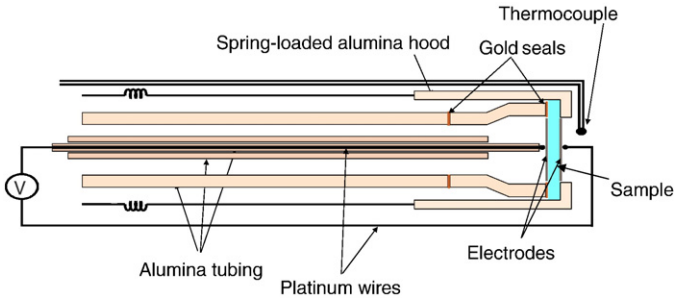

Fig. 3. Sketch of the measurement rig.

Table 1
Concentration cell configurations and transport no. determined.

Experimental conditions		Gas in outer compartment	Gas in inner compartment	Transport no. determined
High p_{O_2}	Dry	O_2/N_2	$O_2/N_2 + N_2$	t_O
	Wet	$O_2/N_2/H_2O$	$O_2/N_2/H_2O + N_2$	t_O
	Wet	$O_2/N_2/H_2O$	$O_2/N_2/H_2O + O_2/N_2$	t_H
Low p_{O_2}	Dry	H_2/N_2	$H_2/N_2 + N_2$	t_H
	Wet	$H_2/N_2/H_2O$	$H_2/N_2/H_2O + N_2$	t_H
	Wet	$H_2/N_2/H_2O$	$H_2/N_2/H_2O + H_2/N_2$	t_O

For comparison, dry oxygen and hydrogen concentration cell experiments were also performed. For all experiments, impedance spectra were recorded at the two end-points of the EMF measurement (no gradient and maximum gradient). The active load method was applied at the maximum gradient by introducing a variable resistor in parallel to the cell.

4. Results and discussion

To verify that the oxygen partial pressure of gas mixtures with the same hydrogen/water vapour ratio and a variable amount of inert gas (nitrogen) was constant, a simple experiment was set up. The $H_2/H_2O/N_2$ mixtures used in the EMF setup were led into a p_{O_2}-sensor consisting of a YSZ-tube kept at 1000 °C. The measured p_{O_2}s are shown in Fig. 4. From this graph, it is clear that the p_{O_2} is not entirely constant over the range of gas mixtures, and that the discrepancy grows greater the more dilute the mixture is. This indicates that the effect must be taken into account if using such gas mixtures. Only when using small gradients, the effect is negligible.

4.1. General impedance data treatment

The impedance data has been fitted using a Voigt type model, see Fig. 5. The number of RQ subcircuits was chosen to give the best fit. All measurements showed an inductance of around 2 µH, which was corrected for in the analysis. This fairly large inductance is due to the fact that the cell is designed for concentration cell measurements and not for impedance measurements. Calculating the pseudocapacitances from the Y_0-, n- and R values of the RQ subcircuits generally gives one pseudocapacitance in the nF range, one in the µF range and one with a higher value. This corresponds to grain boundary

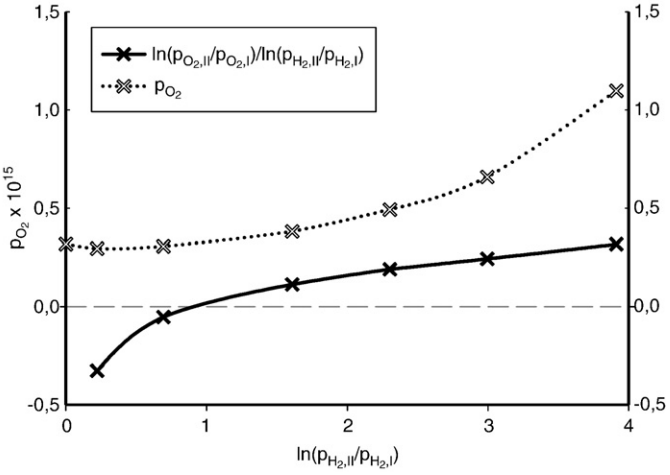

Fig. 4. Oxygen partial pressures measured on mixtures of hydrogen, water vapour and nitrogen. Water vapour partial pressure was varied along with hydrogen, with nitrogen making up the remainder of the gas.

Please cite this article as: H.K. Bentzer, et al., Solid State Ion. (2009), doi:10.1016/j.ssi.2009.11.002

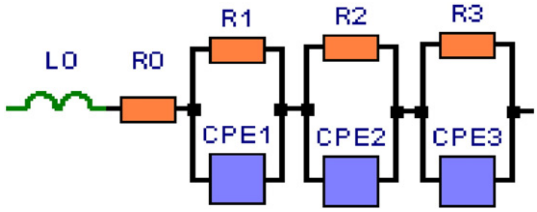

Fig. 5. Equivalent circuit used to analyze the impedance data.

conductivity, double layer charging and possibly a charge transfer reaction.

4.2. Proton transport number

Hydrogen concentration cell experiments were set up using a water vapour concentration gradient at constant oxygen partial pressure at high p_{O_2} and a gradient in hydrogen with and without water vapour at low p_{O_2} respectively. The results can be seen in Fig. 6.

For all measurements, the linear part of the EMF vs. gradient was used to determine the transport number. The transport number for protons is found to be 0.73 in the dry hydrogen experiment, 0.56 at high p_{O_2} and 0.52 at low p_{O_2} in the wet experiments. A large difference is seen in the impedance spectra between dry and wet measurements; the bulk resistance was slightly higher for the dry measurement, while the total conductivity was far higher (up to a factor of 10) for the wet measurements. This indicates that the electrode polarisation resistance is much larger in wet atmospheres, and applying the Liu and Hu correction method brings all transport number values up to between 0.76 and 0.80 for all measurements. The active load method of correction was only applied at the largest gradient. Here, corrected protonic transport numbers were 0.82 at high p_{O_2}, 0.78 in the wet hydrogen cell and 0.65 in the dry hydrogen cell. The active load method also shows that the large curvature in the wet measurement is due to a high electrode polarisation resistance, while electronic conductivity plays a larger role in the dry measurements, with the electronic resistance being only five times as large as the ionic. The lower transport number found using the active load method in the dry cell might be caused by the presence of a minority oxide ion conductivity.

At high p_{O_2} an uncorrected protonic transport number of 0.30 is found at 800 °C (Fig. 7). Using the impedance analysis correction for electrode polarisation gives a protonic transport number of 0.60. The slight curvature observed can be ascribed to an increase in the ratio between total and bulk resistances. Due to the increasing oxide ionic

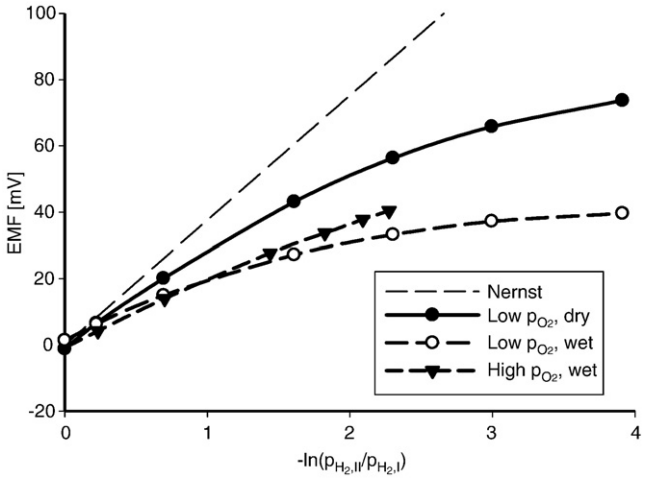

Fig. 6. Plot of measured EMFs vs hydrogen gradient at 600 °C for different experimental configurations as defined in Table 1.

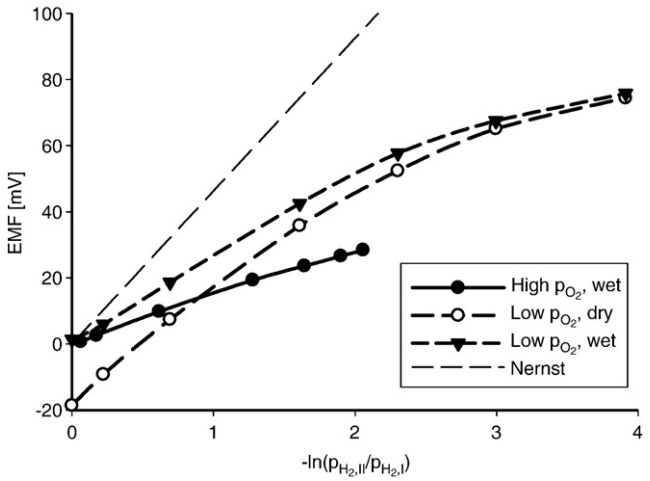

Fig. 7. Plot of measured EMFs vs hydrogen gradient at 800 °C for different experimental configurations as defined in Table 1.

transport number at this higher temperature, the active load correction method no longer works. Attempting to apply it yields negative transport numbers for protons. At low p_{O_2}, the linear part of the EMF vs gradient curve was used, and for the wet measurement a transport number of 0.55 was found. The dry low p_{O_2} measurement reveals a fairly large negative EMF measured at zero applied gradient, but approaches the number for the wet measurement with increasing gradient. This is most likely due to the part of the furnace used as the outer gas compartment not being completely leak-tight, letting in small amounts of air and moisture. Essentially, this just changes the zero point for the gradient, and finding the transport number from the slopes is still possible, even while presenting the data uncorrected. The uncorrected proton transport number was found to be 0.66. Again, attempting to use the active load correction method seems to fail, yielding a lower transport number of 0.51 for the wet measurement, while that for the dry yields a transport number of $>>1$. The corrected proton transport numbers found here are in agreement with previous studies on similar materials [21].

4.3. Oxide-ion transport number

At high p_{O_2} two types of EMF measurements were performed to find t_O; a simple oxygen concentration cell using dry oxygen and dry nitrogen, and a setup where wet oxygen was used and the water vapour was varied in the same way as the oxygen. Theoretically, both yield a gradient in oxygen but no gradient in hydrogen. At low p_{O_2}, the oxygen gradient was created using a water vapour gradient at constant hydrogen partial pressure. The results are shown in Fig. 8.

The analysis of the low p_{O_2} and dry oxygen measurements is straightforward. Before correction for electrode polarisation, the transport number for oxide-ions is found to be 0.11 at high p_{O_2} and 0.012 at low p_{O_2}. The results obtained using wet oxygen show a much larger transport number, despite using formally equal p_{O_2} gradients in dry and wet experiments. Using the initial, linear part of the curve yields a t_O-value of 0.51. The most plausible explanation for this large discrepancy is the large water gradient. Water can be dissociated in the material according to Eq. (18). Although this will cause no EMF of its own, it means that water can be transported through the material. As a result, the water gradient measured at the surface is much smaller than that measured in the bulk of the two gas compartments, creating a gradient in the oxygen/water ratio and hence in hydrogen in the opposite direction of the oxygen gradient. This unintended hydrogen gradient leads to an EMF with the same sign as the oxygen-induced EMF, enhancing the apparent oxygen transport number.

Please cite this article as: H.K. Bentzer, et al., Solid State Ion. (2009), doi:10.1016/j.ssi.2009.11.002

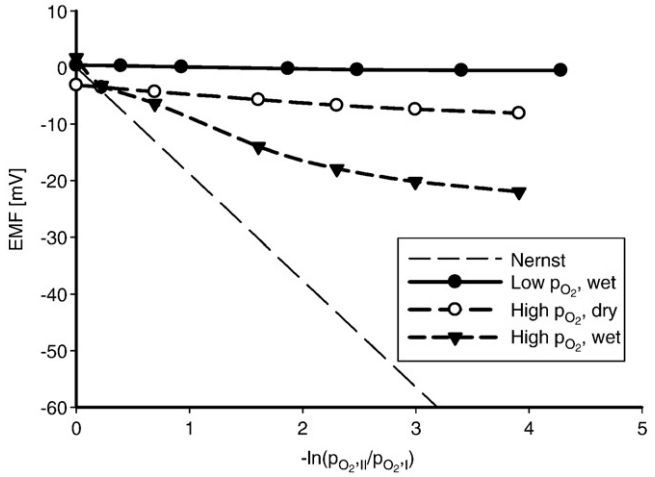

Fig. 8. Plot of measured EMFs vs. oxygen gradient at 600 °C for different experimental configurations as defined in Table 1.

Thus, the dry experiment is better suited for determining the transport number of the minor ionic conduction contributor. The effect also likely affects the low p_{O_2} measurement by reducing the water vapour gradient and hence the oxygen gradient, leading to possible underestimation of the transport number, although the effect in this case is likely much smaller than in the high p_{O_2} wet experiment. Since oxide-ions are a minority carrier in the material, the active load method is invalid. The individual polarisation resistances cannot be found from impedance data, and therefore, applying the impedance analysis correction is also impossible.

Analysis of the data from the dry oxygen concentration cell experiment is again straightforward, yielding an oxide-ion transport number of 0.07. The measurement performed at low p_{O_2} shows an unexpected, negative curvature (Fig. 9). Using only the first, linear part of the curve gives a transport number of 0.20. The sign of the EMF measured in wet oxygen is opposite to the expected, and the opposite of the enhancement observed at 600 °C. Gradients that could lead to such an EMF are one in oxygen in the opposite direction of the one applied, or one in hydrogen in the same direction as the oxygen gradient applied. Since the equilibrium in Eq. (7) gets pushed further to the left at higher temperatures and the concentration of water is higher in the inner gas compartment than in the outer, this might give rise to a sufficiently high hydrogen gradient to explain the EMF seen.

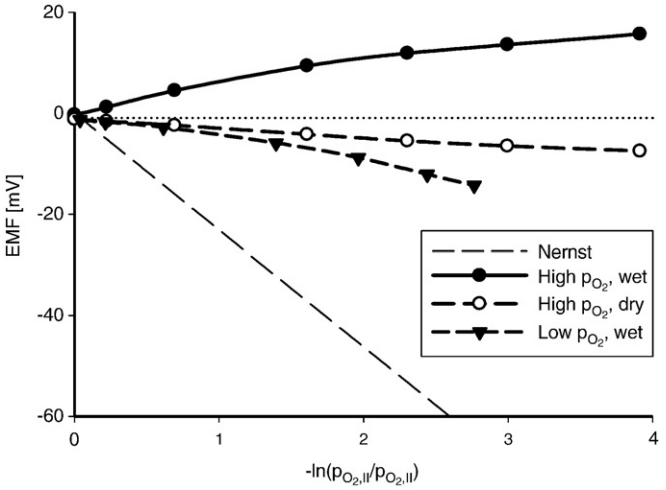

Fig. 9. Plot of measured EMFs vs. oxygen gradient at 800°Cfor different experimental configurations as defined in Table 1.

It would, however, need to be high enough to compete with both oxide-ion conductivity and the water transport error seen at 600 °C. The validity of this explanation remains untested, and further work on the exact temperature behaviour of a wet oxygen concentration cell is required to fully understand the effect. It does, however, remain clear that a wet concentration cell for EMF measurements is an error-prone experimental setup for determination of the transport number of the minor ionic conductor in mixed oxide-ion/proton conductors. Other methods, such as Hebb–Wagner techniques are recommended.

The transport numbers found in dry oxygen are in the range of those reported by Kharton et al. [22], who reported oxide-ion transport numbers of 0.19–0.80 in dry air in the temperature range of 700–950 °C for Y-doped $SrCeO_3$. The number found at 800 °C in this work is lower. One explanation is that it is due to the electrode polarisation effects which could not be taken into account, but which are not expected to be negligible when using platinum electrodes, but other explanations such as those stemming from difference in sample preparation cannot be discounted. Better knowledge of electrode behaviour under the conditions applied, achieved using e.g. more refined impedance spectroscopy measurements could potentially lead to more precise EMF since it would allow for correction for electrode polarisation.

5. Conclusion

Electromotive force measurements as a method for determining transport numbers of conducting species in oxide materials were examined. Two known methods for correcting for electrode polarisation resistance were described, and their application to systems where both protonic, oxide-ionic and electronic conductivity might be significant was discussed. Eight different concentration cell setups were tested at 600 and 800 °C on $SrCe_{0.95}Y_{0.05}O_{3-\delta}$ samples. Presence of water vapour was found to have a large effect on measurements of the minor, oxide-ionic transport number, while dry measurements were found to give reasonable results. All measurements of protonic transport number gave results comparable to those found in similar studies. The material was found to be an almost pure proton conductor at low temperatures in wet reducing atmospheres, with electronic conductivity increasing with decreasing water vapour partial pressure, and oxide-ion conductivity increasing with increasing temperature and decreasing water vapour partial pressure. In general, it is clear from this work that effects of water vapour and electrode polarisation must be taken into account when analysing EMF data from mixed protonic, oxide-ionic and electronic conductors. It also shows that the methods currently used for electrode polarisation correction only function for the systems with a single ionic carrier they were developed for, and that constructing methods for corrections in systems where both e.g. protonic and oxide ionic conductivity is significant will require additional work. When performing EMF measurements on systems where both ionic conduction paths are believed to be significant, electrode material and experimental conditions should be chosen so as to minimise the influence of electrode polarisation resistance.

Acknowledgements

This work has been internally funded by Risø-DTU as part of the project “Initiatives for Hydrogen Separation Membranes”.

References

[1] R. Haase, Thermodynamik der Irreversible Prozesse, Dr. Dietrich Steinkopff Verlag, Darmstadt, 1963.
[2] V.V. Kharton, A.A. Yaremchenko, A.P. Viskup, G.C. Mather, E.N. Naumovich, F.M.B. Marques, Solid State Ionics 128 (2000) 79.

[3] V.V. Kharton, A.P. Viskup, A.V. Kovalevsky, F.M. Figueiredo, J.R. Jurado, A.A. Yaremchenko, E.N. Naumovich, J.R. Frade, Journal of Materials Chemistry 10 (2000) 1161.
[4] M.H. Hebb, Journal of Chemical Physics 20 (1952) 185.
[5] C. Wagner, Z Elektrochem 60 (1956) 4.
[6] C. Wagner, Zeitschrift fuÉr physikalische Chemie Bd. 25 (1933) 25.
[7] H.-I. Yoo, Solid State Ionics 154–155 (2002) 873.
[8] T. Norby, Solid State Ionics 28–30 (1988) 1586.
[9] D.P. Sutija, T. Norby, P. Björnbom, Solid State Ionics 77 (1995) 167.
[10] S. Shin, H.H. Huang, M. Ishigame, Solid State Ionics 40/41 (1990) 910.
[11] M. Glerup, F.W. Poulsen, R.W. Berg, Solid State Ionics 148 (2002) 83.
[12] R. Hempelmann, Physica, B 226 (1996) 72.
[13] V.V. Kharton, F.M.B. Marques, Solid State Ionics 140 (2001) 381.
[14] V.P. Gorelov, Elektrokhimiya 24 (1988) 1380.
[15] M. Liu, H. Hu, Journal of the Electrochemical Society 143 (1996) L109.
[16] J.R. Frade, V.V. Kharton, A.A. Yaremchenko, E.V. Tsipis, Journal of Solid State Electrochemistry 10 (2006) 96.
[17] J. Millman, A. Grabel, Microelectronics2nd Ed, McGraw and Hill, 1988.
[18] M. Widerøe, R. Waser, T. Norby, Solid State Ionics 177 (2006) 1469.
[19] E. O. Ahlgren, J. R. Hansen, N. Bonanos, F. W. Poulsen, M. Mogensen, in F. W. Poulsen, N. Bonanos, S. Linderoth, M. Mogensen, B. Zachau-Christensen (Eds.), Proceedings of the 17th Risø International Symposium on Materials Science, Roskilde, Denmark, 2–6 Sept. (1996), p. 161
[20] http://www.echemsw.com.
[21] X. Wei, Y.S. Lin, Solid State Ionics 178 (2008) 1804.
[22] V.V. Kharton, I.P. Marozau, G.C. Mather, E.N. Naumovich, J.R. Frade, Electrochimica Acta 51 (2006) 6389.

Please cite this article as: H.K. Bentzer, et al., Solid State Ion. (2009), doi:10.1016/j.ssi.2009.11.002

Paper II

J Solid State Electrochem
DOI 10.1007/s10008-010-1235-1

ORIGINAL PAPER

Intermediate temperature ionic conductivity of $Sm_{1.92}Ca_{0.08}Ti_2O_{7-\delta}$ pyrochlore

Karinh E. J. Eurenius · Henrik Karnøe Bentzer · Nikolaos Bonanos · Elisabet Ahlberg · Christopher S. Knee

Received: 11 May 2010 / Revised: 3 November 2010 / Accepted: 4 November 2010

Abstract The results of concentration cell electromotive force methods (EMF) and electrochemical impedance spectroscopy measurements on the pyrochlore system $Sm_{1.92}Ca_{0.08}Ti_2O_{7-\delta}$ are presented. The data have been used to estimate total and partial conductivities and determine transport numbers for protons and oxide ions under various conditions. The EMF techniques employed include corrections for electrode polarisation resistance. The measurements were performed using wet and dry atmospheres in a wide p_{O_2} range using mixtures of H_2, N_2, O_2, and H_2O in the temperature region where proton conductivity was expected (500–300 °C). The impedance measurements revealed the conductivity to be mainly ionic under all conditions, with the highest total conductivity measured being 0.045 S/m under wet oxygen at 500 °C. Both bulk and grain boundary conductivity was predominantly ionic, but electronic conductivity appeared to play a slightly larger part in the grain boundaries. EMF data confirmed the conductivity to be mainly ionic, with oxide ions being the major conducting species at 500 °C and protons becoming increasingly important below this temperature.

Keywords Proton conductor · Pyrochlore · $Sm_2Ti_2O_7$ · Concentration cell electromotive force method (EMF) · Electrochemical impedance spectroscopy (EIS) · Transport numbers

K. E. J. Eurenius · E. Ahlberg · C. S. Knee
Department of Chemistry, University of Gothenburg,
SE-412 96, Gothenburg, Sweden

H. K. Bentzer (✉) · N. Bonanos
Fuel Cells and Solid State Chemistry Division,
Risø National Laboratory for Sustainable Energy,
Technical University of Denmark,
PO Box 49, DK-4000, Roskilde, Denmark
e-mail: henrik.bentzer@risoe.dk

Present Address:
K. E. J. Eurenius
Department of Materials Engineering, School of Engineering,
University of Tokyo,
7-3-1 Hongo, Bunkyo-ku,
Tokyo 113-8656, Japan

Introduction

Proton-conducting perovskite systems have been extensively examined as electrolyte materials [1–5]. Proton-conducting pyrochlores of general formula $A_2B_2O_7$ can be compared with perovskite-based compounds and may also be considered as potential candidates for electrolytes in solid-oxide fuel cells. Acceptor-doped pyrochlores generally exhibit an increase in the ionic conductivity compared with undoped system, with oxide ion charge carriers dominant at high temperature [6, 7], whilst significant proton conductivity can emerge at lower temperatures in hydrated gases [8, 9]. Studies of pyrochlores typically show proton conductivities of about one to two orders of magnitude lower than the best-performing perovskites in the intermediate temperature range (200–700 °C) [10]. Finding new electrolyte materials with adequate conductivity in this temperature interval would be beneficial from a technological point of view in particular with respect to reducing the operating temperature of fuel cells. Therefore, gaining a better understanding of the proton conductivity in pyrochlore systems and finding ways to increase it is of interest.

Studies have recently been presented on proton conductivity in acceptor-doped pyrochlore materials [11, 12]. $Er_{1.96}Ca_{0.04}Ti_2O_{7-\delta}$[11] was found to exhibit high levels

Published online: 25 November 2010

of proton mobility in the grain boundaries but the bulk conductivity showed no dependence on the presence of water vapour. Recently, a detailed study on the proton conduction in $Sm_{1.92}Ca_{0.08}Ti_2O_{7-\delta}$ and $Sm_2Ti_{1.92}Y_{0.08}O_{7-\delta}$ was published [12]. Characterisation by infrared spectroscopy and thermogravimetric analysis (TGA) were used to detect the presence of dissolved protons in the materials. An increase of the bulk conductivity was observed for both samples below 500 °C for wet conditions and measurements in O_2/D_2O and Ar/D_2O revealed an isotopic dependence, indicating that the increased conductivity is due to proton conduction. The A-site-doped sample, $Sm_{1.92}Ca_{0.08}Ti_2O_{7-\delta}$, displayed both a higher proton concentration and conductivity compared with the B-site-doped phase, and was therefore chosen for the more detailed investigations of the conduction species presented herein.

In this work electrochemical impedance spectroscopy (EIS) was carried out on $Sm_{1.92}Ca_{0.08}Ti_2O_{7-\delta}$ to determine the conductivity as a function of p_{O_2} in dry and wet atmospheres and at various temperatures. The results have been compared with the previously presented data from a single atmosphere supplied cell [12]. Furthermore, electromotive force (EMF) measurements combined with active load corrections [13], were carried out to determine the transport numbers associated with the conduction processes.

Theory

Defect chemistry

To understand the underlying processes giving rise to the conductivity, a defect chemical model is formulated. The concentration of the conducting species (i), denoted c_i, is directly related to its conductivity (σ_i) through its mobility (μ_i,) and charge (z_i):

$$\sigma_i = z_i e c_i \mu_i \tag{1}$$

Even if the mobility of the conducting species is not known, the p_{O_2} dependency of the conductivity will still reveal what the dominant point defects in the system are, as long as the mobility can be assumed not to be a function of oxygen partial pressure.

Kröger–Vink notation is used for all point defects. In this model, all oxygen sites will be treated as equal. Protonic defects are described as hydroxide ions on oxygen sites. This is believed to be an accurate description of the defect itself, with proton transport occurring via the Grotthuss mechanism [14].

In acceptor doped pyrochlores, the dopants are assumed to be primarily charge compensated by oxygen vacancies over a wide temperature and oxygen partial pressure range. These can also be formed according to the reaction in Eq. 2:

$$\begin{aligned} &O_O{}^X \rightleftharpoons 1/2O_{2(g)} + V_O{}^{\bullet\bullet} + 2e' \\ &K_O = p_{O_2}{}^{1/2}[V_O{}^{\bullet\bullet}]n^2 \end{aligned} \tag{2}$$

The internal electronic equilibrium is described by Eq. 3, where the K_e is the internal electronic equilibrium constant:

$$\begin{aligned} &\text{nil} \rightleftharpoons e' + h^{\bullet} \\ &K_e = \text{np} \end{aligned} \tag{3}$$

In hydrogen-containing atmospheres, protonic defects can be created according to Eq. 4:

$$\begin{aligned} &2O_O{}^X + H_{2(g)} \rightleftharpoons 2OH_O{}^{\bullet} + 2e' \\ &K_{H_2} = [OH_O{}^{\bullet}]^2 p_{H_2}^{-1} n^2 \end{aligned} \tag{4}$$

Protonic defects can also be introduced through interaction with water as shown in Eq. 5:

$$\begin{aligned} &V_O{}^{\bullet\bullet} + O_O{}^X + H_2O_{(g)} \rightleftharpoons 2OH_O{}^{\bullet} \\ &K_{H_2O} = [OH_O{}^{\bullet}]^2 p_{H_2O}^{-1} [V_O{}^{\bullet\bullet}]^{-1} \end{aligned} \tag{5}$$

Equation 5 can also easily be found by subtracting Eq. 2 and adding the gaseous equilibrium between water, hydrogen and oxygen in Eq. 6 from Eq. 4.

$$H_2O_{(g)} \rightleftharpoons 1/2O_{2(g)} + H_{2(g)} \tag{6}$$

The complete electroneutrality equation for the system is:

$$\left[Ca_{Sm}'\right] + n = 2\left[V_O^{\bullet\bullet}\right] + p + \left[OH_O^{\bullet}\right] \tag{7}$$

To aid the analysis of the conductivity data, simplified electroneutrality conditions can be formulated, where only the dominant species are taken into account. The concentration of other species can then be calculated if the equilibrium constants are known, but their dependency on oxygen and water vapour pressure can be found directly from the equations.

If the dopant level is significant, the concentration of oxygen vacancies will be dominated by the dopant level. In dry conditions, the concentration of oxygen vacancies is dominant and protonic defects negligible, and a simplified electroneutrality condition can be written:

$$\left[Ca_{Sm}'\right] = 2\left[V_O^{\bullet\bullet}\right] \tag{8}$$

The oxide ionic conductivity depends on the concentration of oxygen vacancies, and will therefore not vary with p_{O_2}, while the p_{O_2} dependency of the n- and p-type

electronic conductivity can be calculated from the oxygen vacancy creation reaction (Eq. 2):

$$\begin{array}{l} K_{\mathrm{O}} = p_{\mathrm{O_2}}^{1/2}[V_{\mathrm{O}}^{\bullet\bullet}]n^2 \\ \Updownarrow \\ n \propto p_{\mathrm{O_2}}^{-1/4} \\ \Updownarrow \\ p \propto p_{\mathrm{O_2}}^{1/4} \end{array} \tag{9}$$

At low $p_{\mathrm{O_2}}$ a situation may arise in which the material is sufficiently reduced that electrons take over as the species charge compensating the oxygen vacancies. The simplified charge neutrality condition then becomes:

$$n = 2\left[V_{\mathrm{O}}^{\bullet\bullet}\right] \tag{10}$$

The $p_{\mathrm{O_2}}$ dependence of electronic and oxide ionic conductivities can be expressed by Eq. 11:

$$\begin{array}{l} K_{\mathrm{O}} = p_{\mathrm{O_2}}^{1/2}[V_{\mathrm{O}}^{\bullet\bullet}]n^2 = \frac{1}{2}p_{\mathrm{O_2}}^{1/2}n^3 \\ \Updownarrow \\ n \propto p_{\mathrm{O_2}}^{-1/6} \\ \Updownarrow \\ p \propto p_{\mathrm{O_2}}^{1/6} \end{array} \tag{11}$$

Similarly, at high $p_{\mathrm{O_2}}$, the electron hole conductivity may rise up to a level where it becomes the charge compensator for the dopant, giving a simplified electroneutrality condition as stated by Eq. 12:

$$\left[\mathrm{Ca}_{\mathrm{Sm}}^{'}\right] = p \tag{12}$$

In this situation, the concentration of oxygen vacancies will decrease as $p_{\mathrm{O2}}{}^{-1/2}$.

When water vapour is introduced, protonic defects are created. Assuming the simplified electroneutrality condition in Eq. 8, the concentration of protonic defects relate to the partial pressure of water vapour as follows:

$$\begin{array}{l} K_{\mathrm{H_2O}} = [\mathrm{OH}_{\mathrm{O}}^{\bullet}]^2 p_{\mathrm{H_2O}}^{-1}[V_{\mathrm{O}}^{\bullet\bullet}]^{-1} \\ \Updownarrow \\ [\mathrm{OH}_{\mathrm{O}}^{\bullet}] \propto p_{\mathrm{H_2O}}^{1/2} \end{array} \tag{13}$$

As the concentration of protons increases, they can eventually overtake oxygen vacancies as the species charge compensating the dopant:

$$\left[\mathrm{Ca}_{\mathrm{Sm}}^{'}\right] = \left[\mathrm{OH}_{\mathrm{O}}^{\bullet}\right] \tag{14}$$

which leads to the following water vapour partial pressure dependencies for the other conducting species:

$$\begin{array}{l} [V_{\mathrm{O}}^{\bullet\bullet}] \propto p_{\mathrm{H_2O}}^{-1} \\ n \propto p_{\mathrm{H_2O}}^{1/2} \\ p \propto p_{\mathrm{H_2O}}^{-1/2} \end{array} \tag{15}$$

It should be noted that at the moderate temperatures and oxygen partial pressures employed in this work, the material is expected to remain in the extrinsic ionic conductive region.

The concentration cell EMF method

The EMF method is based on an open cell voltage measurement on a sample equipped with two reversible electrodes and subjected to a gradient in chemical potential. If small gradients are used, an average transport number can be assumed. The voltage measured over the sample will then be equal to:

$$E_{\mathrm{EMF}} = -\frac{RT}{nF}t_{\mathrm{i}}\ln\frac{p_2}{p_1} \tag{16}$$

where R, T, n and F are the universal gas constant, the temperature, the number of electrons transferred and Faraday's number, t_i is the average transport number and p_2 and p_1 are the partial pressures of the active species on either side of the sample. Comparing this to the theoretical voltage calculated using the Nernst Eq. 17:

$$E_{\mathrm{Nemst}} = -\frac{RT}{nF}\ln\frac{p_2}{p_1} \tag{17}$$

it is clear that the average transport number can be calculated by simply dividing the measured voltage with the calculated voltage (Eq. 18):

$$t_{\mathrm{i}} = \frac{E_{\mathrm{EMF}}}{E_{\mathrm{Nemst}}} \tag{18}$$

For systems where both oxide ion and proton conductivity are expected, the equilibrium between hydrogen, oxygen and water vapour must be taken into account. The total voltage developed over the sample can be calculated from partial pressures of gaseous species and transport numbers of oxide ions and protons (t_{O} and t_{p}) according to Eqs. 19 and 20:

$$E_{\mathrm{EMF}} = \frac{RT}{4F}(t_{\mathrm{O}} + t_{\mathrm{H}})\ln\frac{p_{\mathrm{O_2}}^2}{p_{\mathrm{O_2}}^1} - \frac{RT}{2F}(t_{\mathrm{H}})\ln\frac{p_{\mathrm{H_2O}}^2}{p_{\mathrm{H_2O}}^1} \tag{19}$$

or

$$E_{\mathrm{EMF}} = \frac{RT}{2F}(t_{\mathrm{O}})\ln\frac{p_{\mathrm{H_2O}}^2}{p_{\mathrm{H_2O}}^1} - \frac{RT}{2F}(t_{\mathrm{O}} + t_{\mathrm{H}})\ln\frac{p_{\mathrm{H_2}}^2}{p_{\mathrm{H_2}}^1} \tag{20}$$

Using these two equations as guidelines, it is possible to set up concentration cell measurements to determine the total ionic transport number, or the transport number of only oxide ions or protons. Keeping the gas phase equilibrium between oxygen, hydrogen and water vapour in mind, the experiment can be set up to create a gradient over the sample in only one species, as described elsewhere [15].

Correction methods

When using the EMF method, electrode polarisation resistance can possibly lead to underestimation of ionic

transport numbers. Two methods for correcting for high electrode polarisation resistance are reported in the literature; one based entirely on impedance measurements [16], and one based on impedance coupled with a variable load measurement [13]. The high polarisation resistances expected in this work would require time consuming impedance measurements down to very low frequencies, or alternatively extrapolations down to low frequency regions which would introduce a large uncertainty. Therefore, the second method, where only relatively high frequency impedance measurements are required, originally developed by Gorelov [13], was chosen.

The current driven by a Nernstian voltage E_{Nernst} in a sample with ionic, electronic and electrode polarisation resistances R_{i}, R_{e} and R_{η} and electrode over potential η can be described as Eq. 21:

$$I = \frac{(E_{\mathrm{Nernst}} - \eta)}{(R_{\mathrm{i}} + R_{\mathrm{e}})} = \frac{E_{\mathrm{meas}}}{R_{\mathrm{e}}} \tag{21}$$

The overpotential is assumed to be in the linear regime, which is a reasonable assumption at low voltage perturbations. Expressing the potential that would be measured between the electrodes in terms of R_{e}, R_{i} and t_{i} gives:

$$E_{\mathrm{meas}} = \frac{t_{\mathrm{i}} E_{\mathrm{Nernst}}}{1 + \frac{R_{\eta}}{R_{\mathrm{i}}+R_{\mathrm{e}}}} \tag{22}$$

For systems with a small electrode polarisation resistance, this will reduce to the original Wagner expression (Eq. 16). When R_{η} is significant, failing to take the electrode polarisation into account and correcting for it will give an underestimation of t_{i}. In practice, this is done by connecting a variable resistor (R_{b}) in parallel to the sample. This will increase the electronic conductivity of the entire system by an amount ($1/R_{\mathrm{b}}$). An equivalent circuit describing such a setup is shown in Fig. 1. The relation between theoretical and measured voltages for this system can be written as:

$$\frac{E_{\mathrm{Nernst}}}{E_{\mathrm{meas}}} - 1 = (R_{\mathrm{i}} + R_{\eta})\left(\frac{1}{R_{\mathrm{e}}} + \frac{1}{R_{\mathrm{b}}}\right) \tag{23}$$

Here, the left hand side of the expression is proportional to the sample's electronic conductivity ($1/R_{\mathrm{e}}$). If R_{b} is varied, E_{meas} will change and plotting $E_{\mathrm{Nernst}}/E_{\mathrm{meas}} - 1$ against $1/R_{\mathrm{b}}$ will yield a straight line with a slope of $(R_{\mathrm{i}}+R_{\eta})$.

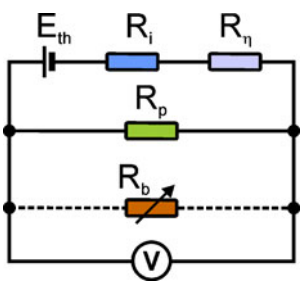

Fig. 1 Equivalent circuit of a concentration cell adapted from ref. [13]. See text for further details

Furthermore, the intercept at the y-axis give $(R_{\mathrm{i}}+R_{\eta})/R_{\mathrm{e}}$ and the extrapolated intersection at the x-axis give $-1/R_{\mathrm{e}}$. By performing an EIS measurement on the sample, the total bulk resistance, R_{T}, can be determined and the electronic transport number (t_{e}) can be expressed:

$$t_{\mathrm{e}} = \frac{R_{\mathrm{T}}}{R_{\mathrm{e}}} \tag{24}$$

Assuming only one ionic conduction path, the ionic transport number corrected for electrode polarisation resistance is:

$$t_{\mathrm{i}} = 1 - t_{\mathrm{e}} \tag{25}$$

As noted elsewhere [15], this correction method is not applicable if both protonic and oxide ionic conductivity is significant. Precise figures for transport numbers for both species are thus not always possible to obtain, but by using EIS and EMF data, a relatively good understanding of the material can be achieved.

Experimental

$Sm_{1.92}Ca_{0.08}Ti_2O_{7-\delta}$ was prepared via conventional solid state reactions of high purity reactants (Sm_2O_3 (99.9%), $CaCO_3$ (99.9%) and TiO_2 (99.9%)) as described in previous studies [16]. The powder was then ball-milled (150 rpm, 90 min) using zirconia balls after a fraction was taken aside to be used as sacrificial powder during sintering. The powders were mixed with a binder (polyvinyl alcohol 2% *w*/*w*) and pressed into pellets They were pressed uniaxially (73.5 MPa) and then as isostatically (325 MPa) in evacuated latex containers followed by sintering carried out in air (1650 °C, 100 h). The microstructure of the pellets was examined using a Zeiss SUPRA 35 scanning electron microscope (SEM).

The $Sm_{1.92}Ca_{0.08}Ti_2O_{7-\delta}$ pellet chosen for the EIS measurements was lightly polished, had a thickness of 2.08 mm and a relative density of 89%. The EIS was measured (4.5 MHz–1 Hz) with a Hioki 3532-50 LCR HiTESTER in a purpose built conductivity cell. The surface of the pellet was painted with Pt-paste (~0.55 cm^2) and the data were collected upon cooling (500–300 °C) in 50 °C interval steps (30–60 min equilibrium time) under a flow of gas (100–1% $O_2/O_2+H_2O/H_2+H_2O$ in N_2). The p_{O_2} was measured using a Nernst type cell built in house.

For the EMF setup, the $Sm_{1.92}Ca_{0.08}Ti_2O_{7-\delta}$ pellet (1.55 mm thick, density 86% of the theoretical value) was fitted with platinum electrodes and rigged inside an alumina tube (Fig. 2) in accordance with previous studies [15]. Gas to the inner and outer compartments was supplied through stainless steel tubes from a mixer setup. For wetting, the gas was bubbled through H_2O bottles in a fridge kept at

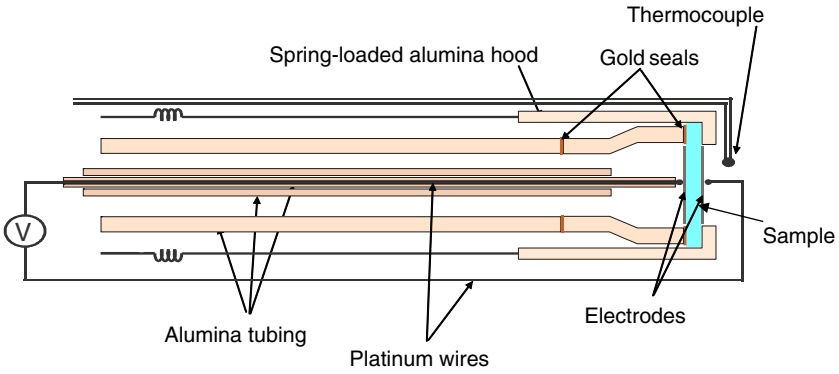

Fig. 2 Diagram of the measurement rig

12 °C, giving approximately 1% water vapour in the gas. Mixing the dry and wet gas enabled control of the water content of the gas. The water vapour concentration was measured using a Dewlux moisture meter from MCM Ltd, Wetherby UK, with analog output.

The experiments were carried out to find the transport numbers for oxide ions (t_O) and protons (t_H); the gas setup for the experiments is displayed in Table 1. The temperatures were decreased from 500 to 300 °C in steps of 100 °C with varying equilibration times (30 min – 2 h) depending on temperature and gas content. The Gorelov corrections for electrode irreversibility were performed at the maximum gas concentration gradient.

Results and discussion

The EIS data were fitted using ZSimpWin 3.21 from Echem Software. Voigt type equivalent circuits were used with a number of sub-circuits in series, each sub-circuit consisting of a resistor and a constant phase element in parallel. The inductance of the cell is known, and was corrected for, before fitting the data. Quasi equivalent capacitances were calculated for each individual RQ-couple. The highest frequency arc typically had a quasi equivalent capacitance in the order of 10^{-11} F cm^{-2}, while the next arc gave values around 10^{-9} F cm^{-2}. These values are typical for bulk and grain boundary conductivity respectively. A lower frequency arc is also observed. This arc, which is very dispersed in most of the measurements, represents the impedance related to various electrode processes. For some of the data, only the initial onset of the electrode arc was present in the data. In such cases, it was fitted with only a constant phase element without a resistor. The platinum electrodes did not cover the entire faces of the pellet, leading to fringing effects. Through final element modelling the error in conductivity was estimated to be approximately 12% and was corrected for.

In Fig. 3 the changes in conductivity with oxygen partial pressure are shown. In general only small changes are observed. Only at 500 °C is a clear increase of conductivity with increasing oxygen pressure observed at the high p_{O_2} end. The data obtained at 500 °C was fitted to Eq. 26:

$$\sigma_{tot} = \sigma_{ion} + \sigma_p^0 p_{O_2}^p + \sigma_n^0 p_{O_2}^{-n} \quad (26)$$

where the subscripts σ_{tot} is the total (measured) conductivity, σ_{ion} is the ionic conductivity, assumed independent of p_{O_2}, ${\sigma_p}^0$ and ${\sigma_n}^0$ are p- and n-type conductivity at $p_{O_2} = 1$, and p and n are positive fitted values to describe the p_{O_2} dependence of the two electronic conductivities. In the fit, both p and n come to a value of approximately 0.014, which is not consistent with any known defect chemical model. The small increase in conductivity that is observed at high and low p_{O_2} could merely be the onset of p- and n-type conductivity, and data from a wider range of oxygen

Table 1 Concentration cell setups

Experimental configuration	Gas in outer compartment (fixed)	Gas added in inner compartment	Transport number determined
A	100% O_2 (dry)	Dry N_2	t_O
B	O_2+H_2O (1%)	Dry O_2	t_H
C	6% H_2, 1% H_2O+N_2	Dry N_2	t_H
D	6% H_2, 1% H_2O+N_2	Dry 6% H_2 in N_2	t_O

The gas in the outer compartment was kept fixed while the gas in the inner compartment was varied to create a gradient by adding the gas noted in steps of 0%, 20%, 50%, 80% and 90%

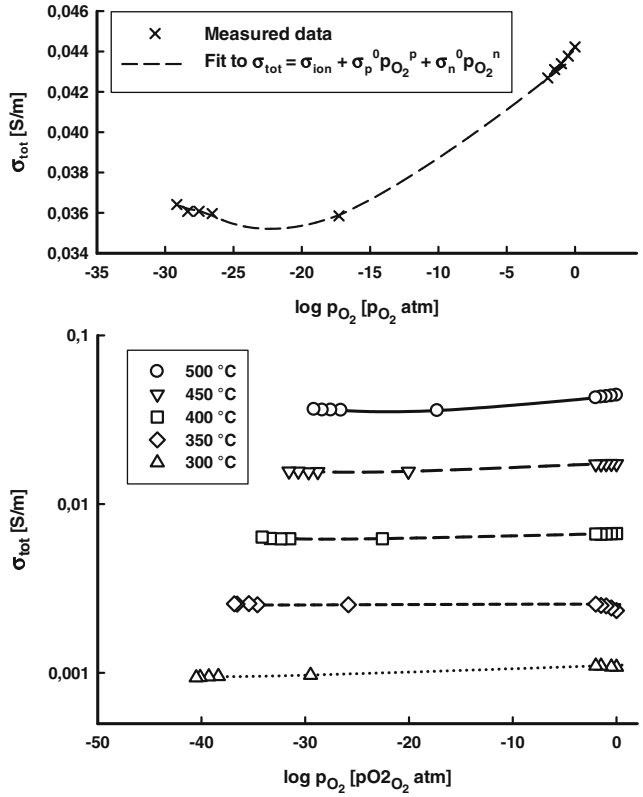

Fig. 3 Conductivity vs. log p_{O_2} at 500 °C (*top*) and conductivity at 500–300 °C vs. log p_{O_2} (*bottom*), all in 1% H_2O. The *lines joining the points in the bottom graph* are guides for the eye only

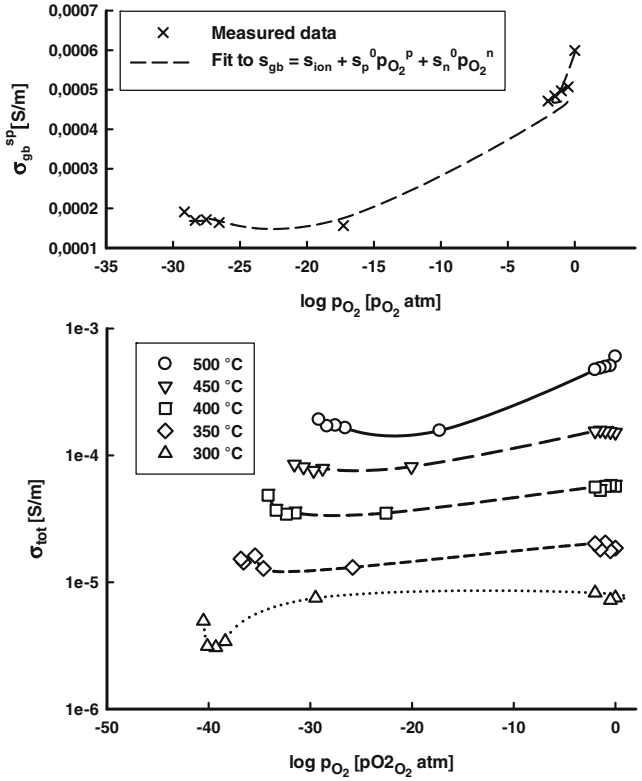

Fig. 4 Specific grain boundary conductivity vs. p_{O_2} at 500 °C (*top*) and specific grain boundary conductivity vs. log p_{O_2} at 300–500 °C (*bottom*), all in 1% H_2O. The *lines joining the points in the bottom graph* are guides for the eye only

partial pressures would be needed to extract their true p_{O_2} dependencies. At lower temperatures, the p_{O_2} dependency of the conductivity was even smaller, and no fitting was attempted.

A similar plot was constructed for the grain boundary conductivity of the material (Fig. 4), and it is immediately clear that a larger dependency on p_{O_2} is present both at high and low p_{O_2} over the entire temperature range. Again, a fit was made of the data from 500 °C, this time yielding *p*- and *n*-exponents of around 0.055. This is still far lower than predicted from the defect chemical model.

As expected the conductivity increases with temperatures and moisture content of the gas. When the temperature is increased, the difference in conductivity of wet and dry runs in oxygen becomes smaller, and at 500 °C they were close to identical. The same trend was observed in the previous measurements [12]. The data from 300 °C in this study gave similar values for the conductivity under dry conditions ($3.75\ 10^{-6}$ Scm^{-1}) as the previous study ($1.6{\cdot}10^{-6}$ Scm^{-1}) [12]. Under wet O_2 similar results are also obtained for the two studies ($1.2{\cdot}10^{-5}$ [12] vs. $1.75\ 10^{-5}$ S cm^{-1}). However, an increase in conductivity in dry argon compared with dry oxygen was reported, indicating n-type conductivity. A similar behaviour was not observed here, even when submitting the sample to atmospheres significantly more reducing than dry argon. The larger conductivity in dry Ar compared with dry O_2 found previously at low temperatures is most likely due to unintentional uptake of moisture during the measurements in Ar. The experimental setup was later modified to avoid this problem by introducing two silica drying tubes for the dry runs.

To examine whether some structural or compositional differences between the samples used in [12] and the samples used for the present work could account for the difference in conductivity vs. p_{O_2} behaviour between the two measurement series, both samples were investigated using scanning electron microscopy. Back scattered mode revealed a few, darker, grains dispersed in both samples. Energy dispersive X-ray spectroscopy indicated that these grains were very rich in calcium, while containing little titanium. Since this secondary phase is present in a too small amount to significantly influence the conductivity, and, furthermore, appeared to be present in roughly the same amount in both samples, it cannot explain the difference in conductivity vs. p_{O_2} behaviour between these measurements and those in [12]. It could, however, indicate that the calcium doping level is slightly above the actual solubility limit.

Dry measurements were not performed in hydrogen atmospheres to protect the sample from overly reducing conditions. The clear difference between wet and dry conductivity measurements can be seen in Fig. 5, which shows Arrhenius plots in wet O_2, dry O_2 and wet 6% H_2 in N_2. The two curves for wet gases are very similar, with the one obtained in oxygen being slightly higher at high temperatures, possibly due to the onset of *p*-type electronic conductivity. The marked difference between the dry and the wet runs, which increases with decreasing temperature, is ascribed to proton conductivity. This is in agreement with TGA data from a previous study on the material, which showed a mass loss beginning at around 375 °C and completing at around 500 °C [12].

As the present conductivity measurements were performed in the temperature range where the proton concentration changes, it was not possible to calculate a true activation energy for the proton conductivity. Measurements at a significantly higher water vapour partial pressure, so as to make sure that the material is saturated with protonic defects over a range of temperatures, would be required. The activation energy found for measurements performed in dry oxygen was 1.0 eV. This is comparable to the previously reported results of 0.93 eV in dry O_2 and 0.58 eV in H_2O and D_2O atmospheres [12].

Grain boundary conductivity has been shown for other systems to be limiting [17], but in this material they appear to only have a minor influence on the total conductivity. SEM analysis revealed a typical grain size of ~10 μm and using the brick layer model [18, 19] to illustrate the grain boundaries as described elsewhere [17], allowed a grain boundary thickness of approximately 5 nm to be estimated. In similar Sn-based pyrochlores [20] the calculated grain boundary thickness was almost ten times larger (~45 nm).

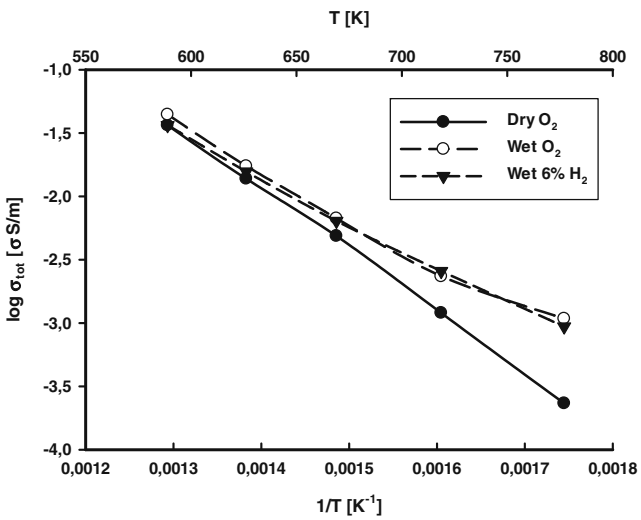

Fig. 5 Arrhenius plots of conductivity of $Sm_{1.92}Ca_{0.08}Ti_2O_{7-\delta}$ under dry and wet (1% H_2O) gas in 100% O_2 and 6% H_2 in N_2

From the grain size and grain boundary thickness the specific grain boundary conductivity can be calculated, and is shown to be about 100–400 times lower than the total conductivity. The p_{O_2} dependency of the grain boundary conductivity (Fig. 4) is stronger than that for bulk. The specific grain boundary conductivity decreases with decreasing oxygen partial pressure at constant temperature, while the bulk conductivity is overall constant. The fact that the p_{O_2} dependency of conductivity in the grain boundaries remains small, along with the fact that the it also increases when introducing water vapour in the atmosphere suggests that proton conduction also occurs in the grain boundaries but with a much lower conductivity than for the grain interior (bulk). For $Er_{1.96}Ca_{0.04}Ti_2O_{6.98}$ [11] proton conduction at the grain boundary was found to be significant but the bulk conductivity was dominated by oxide ion charge carriers. The reason for this differing behaviour may be linked to the subtleties of the synthesis routes. Fjeld et al. [11] report the presence of a Si impurity at the grain boundary originating possibly from the glass beaker used to prepare the initial solution of Er_2O_3 and $CaCO_3$.

The EMF measurements were carried out to find t_O and t_H. Investigations to determine the former were based on an oxygen concentration cell using dry oxygen and dry nitrogen/oxygen mixtures. t_H was evaluated at both high and low oxygen partial pressures. For a low p_{O_2} estimate of t_H, wet hydrogen diluted with nitrogen is used on one side of the sample, and the same gas mixed with dry inert gas (nitrogen) on the other side. In this manner, the hydrogen/water vapour ratio is kept constant and no unintentional oxygen partial pressure gradient is created. At high p_{O_2} a gradient in hydrogen partial pressure is created by using fixed levels of oxygen and water vapour on one side of the sample, while varying the oxygen/water vapour ratio, and thereby the hydrogen partial pressure, on the other side. Similarly, a gradient in oxygen can be made at low p_{O_2} by varying the water vapour partial pressure while maintaining a fixed hydrogen partial pressure on both sides. This measurement was also attempted, but only gave interpretable results at 500 °C. Given the results, it seems likely that this is due to the fact that proton conductivity is far higher than oxide ion conductivity, and even a slight unintended gradient in hydrogen partial pressure will obscure any EMF from the oxygen gradient.

The active load correction was carried out at the largest concentration gradient for each measurement series by adding a variable resistor to the circuit and recording the resulting change in EMF. Figure 6 shows the measured EMF data to determine t_H in oxidising conditions at 400 °C along with the data for the electrode polarisation resistance correction.

As expected, electrode polarisation resistance was significant in all measurements. In oxidising atmospheres,

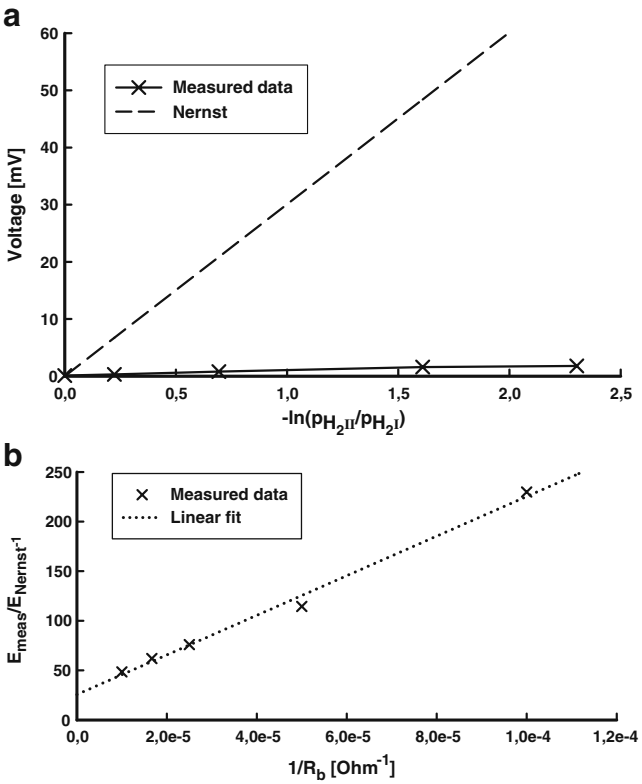

Fig. 6 Typical EMF measurement data from wet O_2 (t_H) 400 °C, configuration B in Table 1 (**a**), and active load measurement for electrode polarisation resistance correction of the same measurement (**b**)

impedance data showed it to be around a factor of 20 larger than the sample resistance at 500 °C and increasing with decreasing temperature. Electrode polarisation resistance was much lower in reducing atmospheres. At the lowest temperatures, this means that the entire electrode contribution to the impedance was not measured, but had to be extrapolated, since very low frequencies would have had to be employed to measure them. For the active load measurement, the resistor introduced in parallel needs to be of the same order of magnitude as the internal electronic resistance, i.e. the electronic resistance of the sample. Introducing a much smaller electronic resistance caused some drift in the EMF values. This explains for example the corrected proton transport number of 1.06 that was measured at high p_{O_2} at 300 °C. The uncorrected and corrected EMF data, along with the calculated transport numbers, are summarised in Table 2.

Despite the high electrode polarisation resistance, there is a clear trend in the data. At 300 and 400 °C in wet conditions the proton transport number is close to unity while the transport number for oxide ions is close to zero at these temperatures. At 500 °C the trend is reversed, with the oxide ionic transport number being close to unity and the protonic close to zero. This is in good agreement with previous results, where protons were shown to leave the compound as the temperature is increased towards 500 °C [12]. It is, however, not possible from these data to completely exclude the possibility that some protonic conductivity remains at 500 °C, or that some oxide ionic conductivity is still present at lower temperatures, since the necessary correction methods are not valid for systems with more than two conduction paths. It is also worth noting that the electrode polarisation resistance and the necessary correction for it is much greater in dry and oxidising conditions than in wet and reducing. This behaviour is in excellent agreement with the behaviour of platinum electrodes on ytterbium-doped strontium cerate [21].

Conclusions

The combined EIS and EMF measurements show that the conduction in $Sm_{1.92}Ca_{0.08}Ti_2O_{7-\delta}$ is mainly ionic. At 500 °C oxide ion transport dominates with a transport number, $t_O > 0.98$, while at 300 and 400 °C proton conduction takes over in wet conditions. Using the active load correction method, protons appear to be the majority charge carrier at both 300 and 400 °C, in both reducing and oxidising wet conditions. Using this correction method we were able to estimate reasonably reliable ionic transport numbers in the region where electrode polarisation resistance dominated. The partial pressure dependences suggested that electronic conduction probably plays

Table 2 Transport numbers for protons and oxide ions

		Configuration (see Table 1)		300 °C	400 °C	500 °C
t_O	High	A	Uncorrected	–	0	0.073
			Corrected	–	0	0.986
	Low	D	Uncorrected	–	–	0.75
			Corrected	–	–	0.991
t_H	High	B	Uncorrected	0.08	0.026	0
			Corrected	1.06	0.947	0
	Low	C	Uncorrected	0.42	0.34	0
			Corrected	0.876	0.924	0

a larger role in the grain boundaries than in the grain interior but the total conductivity is dominated by and practically equal to bulk conduction in this temperature interval.

Acknowledgements This work has been supported by the Swedish Research Council (Vetenskapsrådet) and by Risø-DTU as part of the project "Initiatives for Hydrogen Separation Membranes".

References

1. Iwahara H (1995) Solid State Ionics 77:289–298
2. Scherban T, Nowick AS (1989) Solid State Ionics 35:189–194
3. Bonanos N, Ellis B, Mahmood MN (1991) Solid State Ionics 44:305–311
4. Ahmed I, Eriksson SG, Ahlberg E, Knee CS, Berastegui P, Johansson LG, Rundlöf H, Karlsson M, Matic A, Börjesson L, Engberg D (2006) Solid State Ionics 177:1395–1403
5. Kreuer KD (2003) Annu Rev Mater Res 33:333–359
6. Yamamura H, Nishino H, Kakinuma K, Nomura K (2003) J Ceram Soc Jan 111:902–906
7. Kramer SA, Tuller HL (1995) Solid State Ionics 82:15–23
8. Omata T, Okuda K, Tsugimoto S, Otsuka-Yao-Matsuo S (1997) Solid State Ionics 104:249–258
9. Labrincha JA, Frade JR, Marques FMB (1997) Solid State Ionics 99:33–40
10. Omata T, Otsuka-Yao-Matsuo S (2001) J Electrochem Soc 148: E252–E261
11. Fjeld H, Haugsrud R, Gunnaes AE, Norby T (2008) Solid State Ionics 179:1849–1853
12. Eurenius KEJ, Ahlberg E, Ahmed I, Eriksson SG, Knee CS (2010) Solid State Ionics 181:148–153
13. Gorelov VP (1988) Elektrokhimiya 24:1380–1381
14. de Grotthuss CJT (1806) Ann Chim 58:54
15. Bentzer HK, Bonanos N, Phair JW (2010) Solid State Ionics 181:249–255
16. Liu M, Hu H (1996) J Electrochem Soc 143:L109–L112
17. Fleig J, Maier J (1998) J Electrochem Soc 145:2081–2089
18. van Dijk T, Burggraaf AJ (1981) Phys Status Solidi A 63:229–240
19. Verkerk MJ, Middelhuis BJ, Burggraaf AJ (1982) Solid State Ionics 6:159–170
20. Eurenius KEJ, Ahlberg E, Knee CS (2010) Solid State Ionics 181:1577–1585
21. Potter AR, Baker RT (2006) Solid State Ionics 177:1917–1924